PL-TR-96-2069

PATH CALIBRATION, SOURCE ESTIMATION AND REGIONAL DISCRIMINATION FOR THE MIDDLE EAST: APPLICATION TO THE HINDU-KUSH REGION

C.K. Saikia
B.B. Woods
L. Zhu
H.K. Thio
D.V. Helmberger

Woodward-Clyde Federal Services
566 El Dorado Street, Suite 100
Pasadena CA 91101-2560

31 January 1996

DTIC QUALITY INSPECTED 2

19960924 077

Scientific Report No. 1

PHILLIPS LABORATORY
Directorate of Geophysics
AIR FORCE MATERIEL COMMAND
HANSCOM AIR FORCE BASE MA 01731-3010

This technical report has been reviewed and is approved for publication.

DELAINE REITER
Contract Manager
Earth Sciences Division

JAMES F. LEWKOWICZ
Director
Earth Sciences Division

DISCLAIMER NOTICE

UNCLASSIFIED

Technical Report
distributed by

**DEFENSE
TECHNICAL
INFORMATION
CENTER**

DTIC Acquiring Information—
Imparting Knowledge

Cameron Station
Alexandria, Virginia 22304-6145

UNCLASSIFIED

THIS DOCUMENT IS BEST
QUALITY AVAILABLE. THE
COPY FURNISHED TO DTIC
CONTAINED A SIGNIFICANT
NUMBER OF PAGES WHICH DO
NOT REPRODUCE LEGIBLY.

REPORT DOCUMENTATION PAGE

1. AGENCY USE ONLY (Leave blank)	2. REPORT DATE	3. REPORT TYPE AND DATES COVERED
	31 January 96	Scientific Report #1

4. TITLE AND SUBTITLE
Path Calibration, Source Estimation and Regional Discrimination for the Middle East: Application to the Hindu-Kush Region

5. FUNDING NUMBERS
Contract No:
F19628-95-C-0093
PE 62301E

PR NM95 TA GM WU AC

6. AUTHOR(S)
C.K. Saikia, B.B. Woods, L. Zhu*,
H.K. Thio, and D.V. Helmberger*

7. PERFORMING ORGANIZATION NAME(S) AND ADDRESS(ES)
Woodward-Clyde Federal Services
566 El Dorado Street, Suite 100
Pasadena CA 91101-2560

8. PERFORMING ORGANIZATION REPORT NUMBER
WCFS-R-96-01

9. SPONSORING / MONITORING AGENCY NAME(S) AND ADDRESS(ES)
Phillips Laboratory
29 Randolph Road
Hanscom AFB MA 01731-3010

Contract Manager: Dr. Delaine Reiter/GPE

10. SPONSORING / MONITORING AGENCY REPORT NUMBER
PL-TR-96-2069

11. SUPPLEMENTARY NOTES
* California Institute of Technology
Seismological Laboratory 252-21
Pasadena CA 91125

12a. DISTRIBUTION / AVAILABILITY STATEMENT

Approved for public release; distribution unlimited.

12b. DISTRIBUTION CODE

13. ABSTRACT (Maximum 200 words)

We have analyzed observations of earthquakes occurring in the Hindu-Kush region to establish a basis for location and discrimination using the new broadband station NIL, a GSETT-3 β station, which is located near the site of the GSETT-3 α array PKAR in Pakistan. Preliminary analyses of the regional data at NIL in terms of energy ratios (the integrated energy in the short-period P_{nl} wavetrain, divided by the intermediate-period, three component, surface wave integrated energy) produces plots not unlike those produced by a similar analysis of TERRAscope data (for the southwestern U.S.). NTS explosions consistently plot higher than regional earthquakes in the latter population, Woods and Helmberger (1996). In the NIL earthquake population, there are observed events with high ratios which look like explosions but appear to be deep events where the surface waves have become weak relative to the body waves. The identical problem occurs for the m_b:M_s discriminants for events in this region. Thus, the ability to determine the source depth becomes crucial in this region as a complimentary method to infer the source type. To calibrate the regional paths we selected 5 crustal and 5 sub-crustal events ($5.5 < M_w < 4$) to study in detail both teleseismically and regionally. Most of these local events were recorded by

14. SUBJECT TERMS
Waveform Modeling   Master Events   1-D Crustal Structure
Seismic Monitoring   Relocation   Seismology
Hindu-Kush   Path Calibration   Discrimination

15. NUMBER OF PAGES
140

16. PRICE CODE

17. SECURITY CLASSIFICATION OF REPORT	18. SECURITY CLASSIFICATION OF THIS PAGE	19. SECURITY CLASSIFICATION OF ABSTRACT	20. LIMITATION OF ABSTRACT
Unclassified	Unclassified	Unclassified	SAR

SECURITY CLASSIFICATION OF THIS PAGE

CLASSIFIED BY:

DECLASSIFY ON:

13. Abstract (Continued)

the temporary local arrays in Pakistan (PAKN) and in Kyrgyzstan (KNET) and by the IDC network of far-regional teleseismic stations. Several 1-D models were developed to fit the local waveform data and a useful library of Green's functions generated for use in source inversions. We used a modification of the "cut-and-paste" method for obtaining estimates of moment, strike, dip, rake and depth by applying a direct grid search, after Zhu and Helmberger (1995). For shallow events, the depth constraint is provided by the ratio of Pnl to surface waves, whereas for deep events the time separation between sPmP and P becomes the best indicator of depth. Teleseismic and far-regional short-period waveform synthetics predicted by standard earth models and the local source inversion parameters compare quite well with events greater than Mw > 4.5, although the depth phases (pP, sP) are not always clear for shallow events. Smaller events become problematic to analyze at teleseismic distances even for stacked array data although upper-mantle triplication arrivals still provide reasonable estimates of location (50 km). A comprehensive review of these master event locations relative to those of the various monitoring agencies (such as ISC and AFTAC) reveals the importance of local data, especially for depth controls. Source parameters and locations obtained from two stations (SBRA, the nearest PAKN station to NIL, and AAK, an IRIS/IDA station situated in the KNET) prove quite compatible to the results from the 10 master event study using both arrays. Since the PKAR array (when operational) can help establish locations independent of AAK and the single broadband station NIL can provide depth constraints, we should be in a position to automate regional discrimination and location techniques for the Hindu-Kush area.

SECURITY CLASSIFICATION OF THIS PAGE

TABLE OF CONTENTS

Acknowledgements

Summary

We have analyzed observations of earthquakes occurring in the Hindu-Kush region to establish a basis for location and discrimination using the new broadband station NIL, a GSETT-3 β station, which is located near the site of the GSETT-3 α array PKAR in Pakistan. Preliminary analyses of the regional data at NIL in terms of energy ratios (the integrated energy in the short-period P_{nl} wavetrain, divided by the intermediate-period, three component, surface wave integrated energy) produces plots not unlike those produced by a similar analysis of TERRAscope data (for the southwestern U.S.). NTS explosions consistently plot higher than regional earthquakes in the latter population, Woods and Helmberger (1996). In the NIL earthquake population, there are observed events with high ratios which look like explosions but appear to be deep events where the surface waves have become weak relative to the body waves. The identical problem occurs for the m_b:M_s discriminants for events in this region. Thus, the ability to determine the source depth becomes crucial in this region as a complimentary method to infer the source type. To calibrate the regional paths we selected 5 crustal and 5 sub-crustal events ($5.5 < M_w < 4$) to study in detail both teleseismically and regionally. Most of these local events were recorded by the temporary local arrays in Pakistan (PAKN) and in Kyrgyzstan (KNET) and by the IDC network of far-regional teleseismic stations. Several 1-D models were developed to fit the local waveform data and a useful library of Green's functions generated for use in source inversions. We used a modification of the "cut-and-paste" method for obtaining estimates of moment, strike, dip, rake and depth by applying a direct grid search, after Zhu and Helmberger (1995). For shallow events, the depth constraint is provided by the ratio of P_{nl} to

surface waves, whereas for deep events the time separation between sP_mP and P becomes the best indicator of depth. Teleseismic and far-regional short-period waveform synthetics predicted by standard earth models and the local source inversion parameters compare quite well with events greater than $M_w > 4.5$, although the depth phases (pP, sP) are not always clear for shallow events. Smaller events become problematic to analyze at teleseismic distances even for stacked array data although upper-mantle triplication arrivals still provide reasonable estimates of location (50 km). A comprehensive review of these 10 master event locations relative to those of the various monitoring agencies (such as ISC and AFTAC) reveals the importance of local data, especially for depth controls. Source parameters and locations obtained from two stations (SBRA, the nearest PAKN station to NIL, and AAK, an IRIS/IDA station situated in the KNET) prove quite compatible to the results from the 10 master event study using both arrays. Since the PKAR array (when operational) can help establish locations independent of AAK and the single broadband station NIL can provide depth constraints, we should be in a position to automate regional discrimination and location techniques for the Hindu-Kush area.

1. Introduction

In this era of increased concern for the proliferation of nuclear weapons, the need for effective seismic discrimination techniques is perhaps more important than ever before. As more countries attain or near the technology threshold needed to develop nuclear weapons, more regions of the world need to be monitored for verification purposes. Consequently, a program is planned to install seismic arrays in Pakistan (PKAR), Turkmenistan (ABKO), Egypt (LXAR), and Russia (KIVO) to monitor this volatile region. These types of arrays have demonstrated the ability to detect small events at large distances and therefore are essential in low-yield monitoring. The main difficulty is in discrimination and the recognition of a "first blast", since these regions have many earthquakes, but virtually no large explosions. While small earthquakes ($M_w < 4$) can cause difficulties in discrimination, larger earthquakes ($M_w > 4.5$) can be used to calibrate paths and establish source estimation techniques useful for discrimination of all types and sizes of events. For example, events larger than about 5 generally can be observed teleseismically and their depth phases, pP and sP, identified. Standard processing can be applied to estimate source orientation and strength quite independently of regional data. Thus, the regional Green's functions and paths to the various arrays can be studied with a suite of known sources (master events).

To implement these ideas we have concentrated on the Hindu-Kush region; a region of complex geology and a region where the present $m_b:M_s$ technique has had difficulties identifying some events (Blandford, personal communication). These difficulties have been traced to deep crustal events and upper-mantle events which have correspondingly weaker M_s than shallow events, making them fall in the explosion population. Thus, these events appear interesting at all magnitudes. Figure 1 displays the target area for this study. It contains the two broadband arrays PAKN (in Pakistan) and KNET (in Kyrgyzstan). They are separated by about 900 km with numerous earthquakes occurring at various depths in between. The KNET station AAK, not presently a GSETT-3 station, and NIL (a GSETT-3 β station), just south of the PAKN, report regularly to the IDC and are becoming part of the monitoring system. The primary purpose of this report is to calibrate the region to improve the capability of those two stations, as well as the GSETT-3 α arrays to be co-deployed, in order to locate and identify events.

Ten events were chosen for detailed study, five crustal and five upper-mantle. Each event is identified by the notation XXX.HHMM where XXX is the Julian day and HHMM is the nearest origin time in hour (HH) and minute (MM). Their mechanisms, determined from modeling the regional seismograms, are shown in Figure 1. They range in size from $M_w = 4.0$ to 5.5. The larger events have CMT (Centroid Moment Tensor) solutions and are well-recorded by the global arrays, including some stations operated by AFTAC. We will discuss these data in detail as they pertain to location (latitude, longitude and depth), origin times and magnitudes. A small number of other events have been included on the map which are available from the temporary deployment of PAKN. All the above events were processed with respect to our favored energy discriminant.

One of the most promising universal discriminants, in our opinion, is the ratio of short-period (1 Hz) vertical component energy integrated over the extended P-wave window to that of the intermediate-period (0.05 to 0.16 Hz) three component integrated surface wave energy plotted versus distance. Explosions tend to have higher ratios than earthquakes for a given magnitude in the same fashion as the $m_b:M_s$ discriminant. Thus, this measure can be viewed as an extension of the well-known teleseismic $m_b:M_s$ method to regional distances. Documentation of the method is given in Woods and Helmberger (1996) who analyzed 32 NTS underground explosions and 131 earthquakes occurring in the southwestern U.S. The results are shown in Figure 2 (a).

Results of this discriminant for Hindu-Kush earthquakes located in Figure 1, as well as other events examined in Section 4, are given in Figure 2 (b). Unlike the case for the TERRAscope data set, the Pakistan data set includes no explosions, so that all inferences regarding this discriminant must be based on the behavior of earthquakes. Further, unlike the case of the southwestern U.S., where the seismicity is confined to the upper crust (d $\leq$ 30 km), seismicity in this region is spread throughout the crust and into the mantle down to a depth of at least 230 km. In general, the shallow and intermediate depth earthquakes have energy ratios similar to, although slightly higher than, those recorded by TERRAscope. This can be seen by overlaying Figures 2 (a) and (b), which have the same axes. Even disregarding the deeper Pakistani events, the upper-bound energy ratio cut-off is slightly higher for the Pakistan earthquake data than its TERRAscope counterpart. This difference can be explained by regional propagation

2
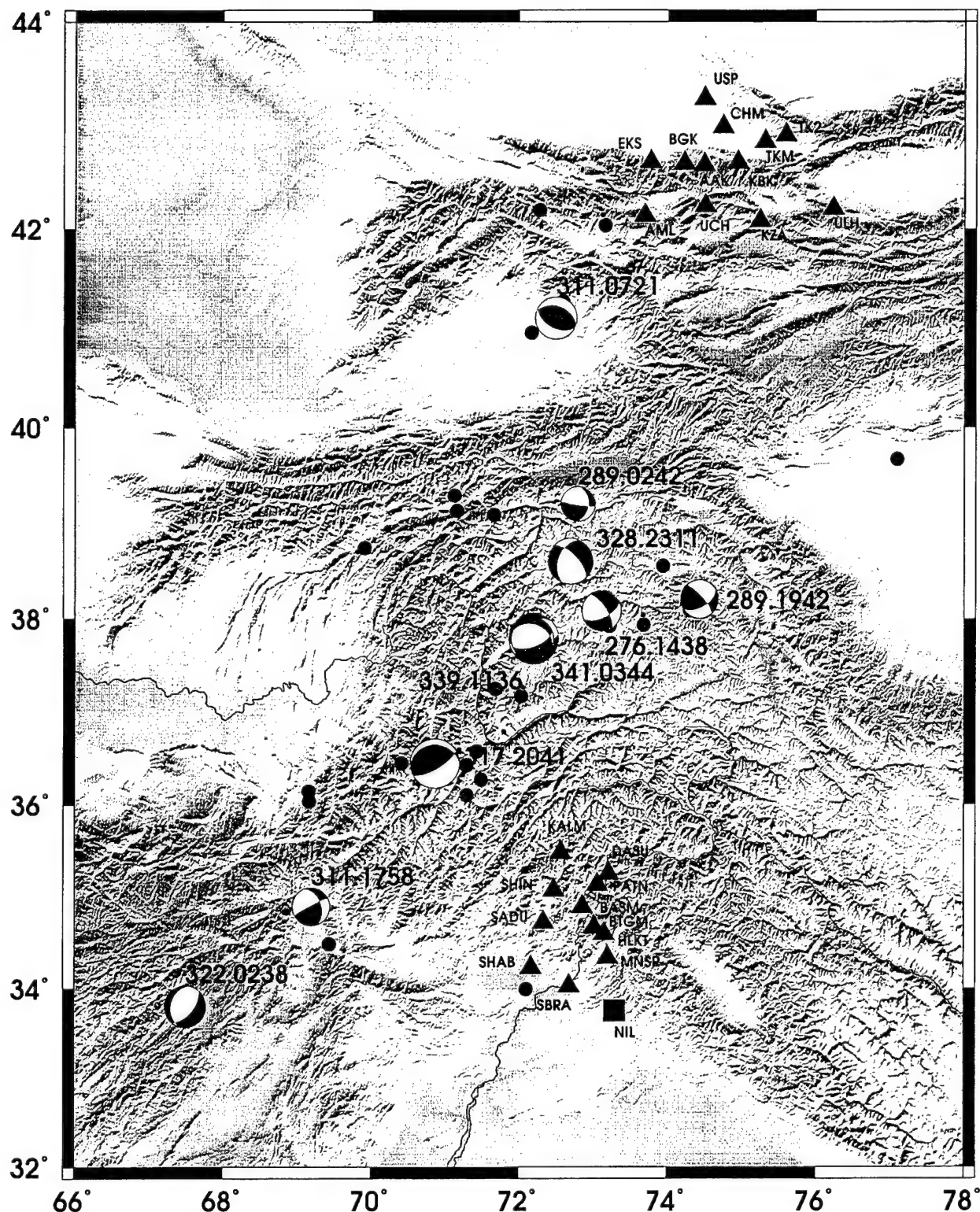
Figure 1 Map of the Hindu-Kush region showing the locations and mechanisms of
the events sudied in this paper. The focal mechanisms are derived using the inversion of
regional broadband data, the red dots are events used in the short-period:long-period energy
discrimination study. The triangles represent the stations of the KNET and PAKN arrays,
the square is the location of the broadband station NIL. Blue focal mechanisms denote deep
events, red mechanisms are crustal events.
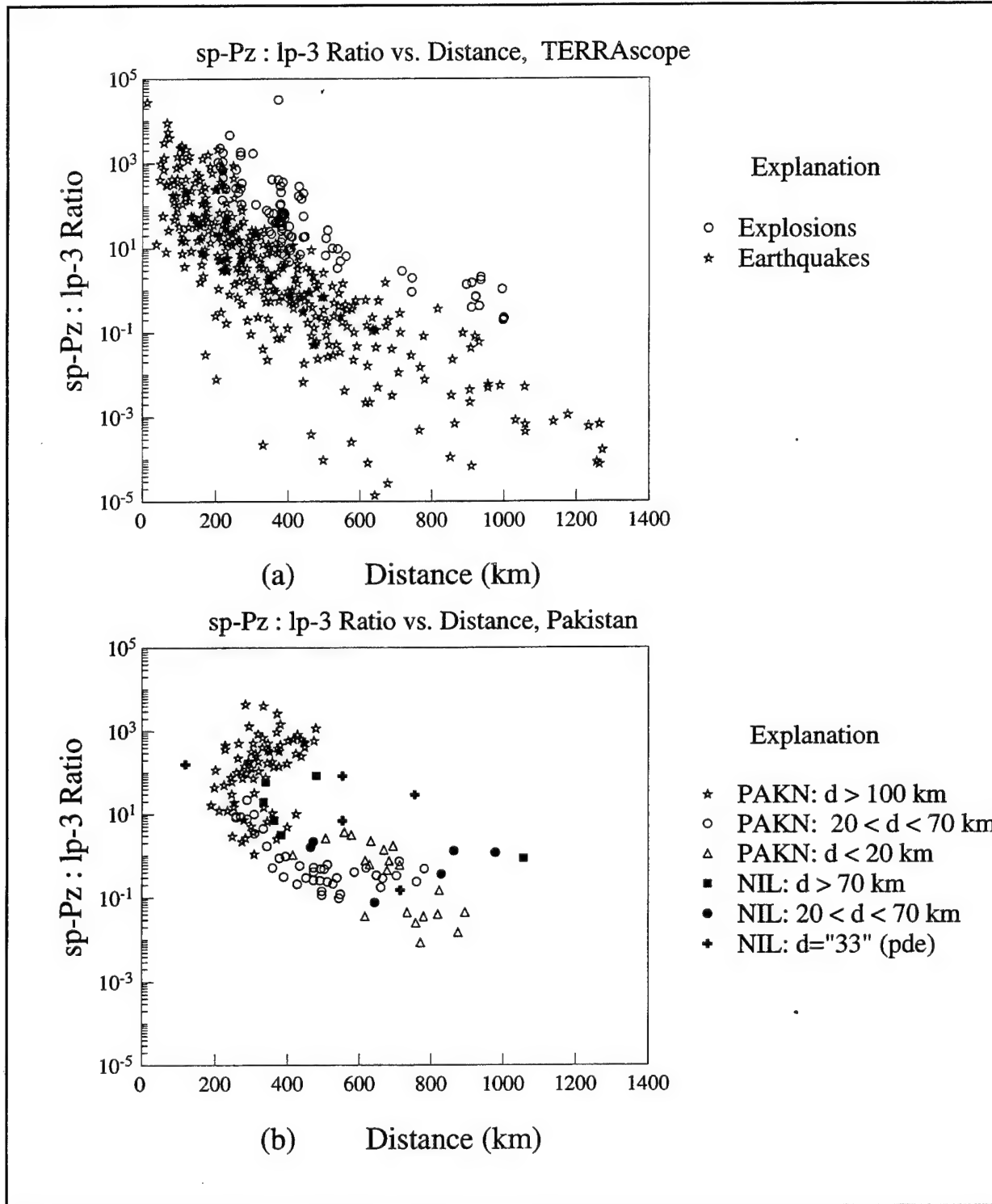
Figure 2 (a)   Short-period:long-period energy ratio vs. distance for TERRAscope data; stars represent earthquakes and circles represent explosions. (b) The energy ratio discriminant for data recorded by stations in Pakistan. Events are sorted by depth as well as the station (NIL) or array (PAKN) by which they were recorded.

characteristics and can be accounted for by calibrating the energy ratio discriminant from region to region. In the course of this project, we have made refinements to Figure 2 (b) using magnitude corrections that improve the performance of the energy discriminant (Section 4.3; Figure 36).

The deeper (mantle) events however have relatively higher energy ratios, which is explained by the lack of long-period fundamental-mode surface wave energy from deep events. Such deep earthquakes are problematic for this discriminant, just as they are for the teleseismic m_b:M_s discriminant, unless their depths can be accurately estimated (Marshall and Basham, 1972). Further, the earthquakes which have reported depths of 33 km do not lie within one population group or another, suggesting that the ones with higher energy ratios are in fact significantly deeper than 33 km. In this way, this measurement can be used as a fast depth estimator or depth discriminant to identify deep mantle events from crustal events, although other high energy ratio source outlier events, i.e. explosions would fall into this deep event category.

We conclude that the deep events look explosion-like. Methods of establishing that they are deep thus becomes a key point of the overall discrimination process, i.e. an event that plots with the deep events but cannot be proven to be deep could be an explosion. In addition, the depths for events occurring in the Middle East and North Africa have both deep and shallow depths as is seen in Figure 3. This figure includes only those events for which the CMT solutions are available. The deep events are marked in blue color (depth $\geq$ 75 km) and the shallow events are marked in red. Figure 4 shows the significant variation in depth between the CMT and ISC estimates. Resolving the depth ambiguity for some selected events is also crucial because in a new geographic region to be calibrated, ground truth information for the master events is very useful for deciphering the waveguide characteristics contained in the data. Although our objective is to calibrate and study path effects throughout this entire region, we will concentrate in this report on the Hindu-Kush events.

To address these various issues we have broken the study into four sections. Section 2 deals with source estimation from regional seismograms, relatively long-period array data, and using imperfect Green's functions. With the sources reasonably well established we can examine the

5
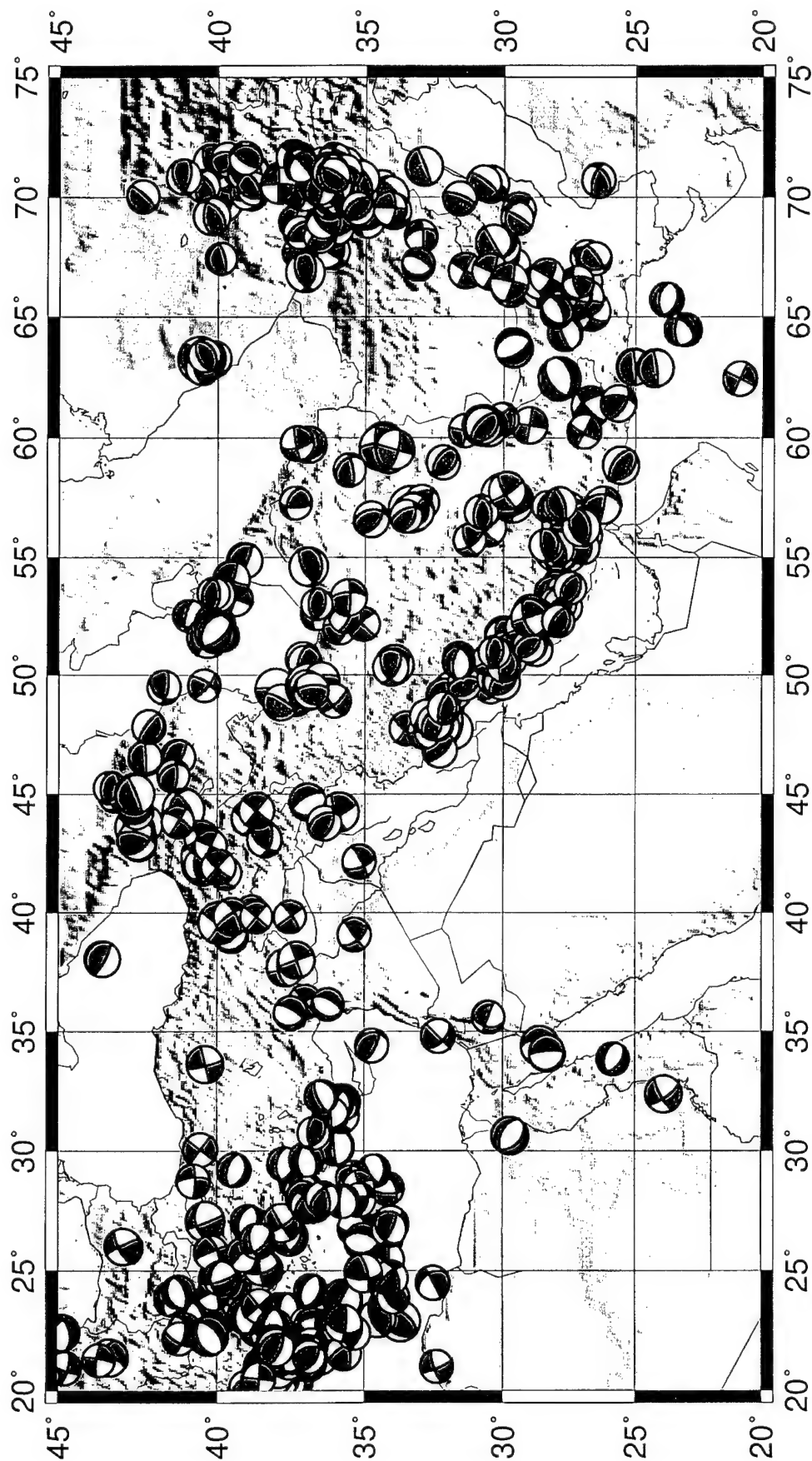
Figure 3   Map of the Middle-East showing the Harvard CMT solutions, divided in crustal events (red) and deep events (blue).
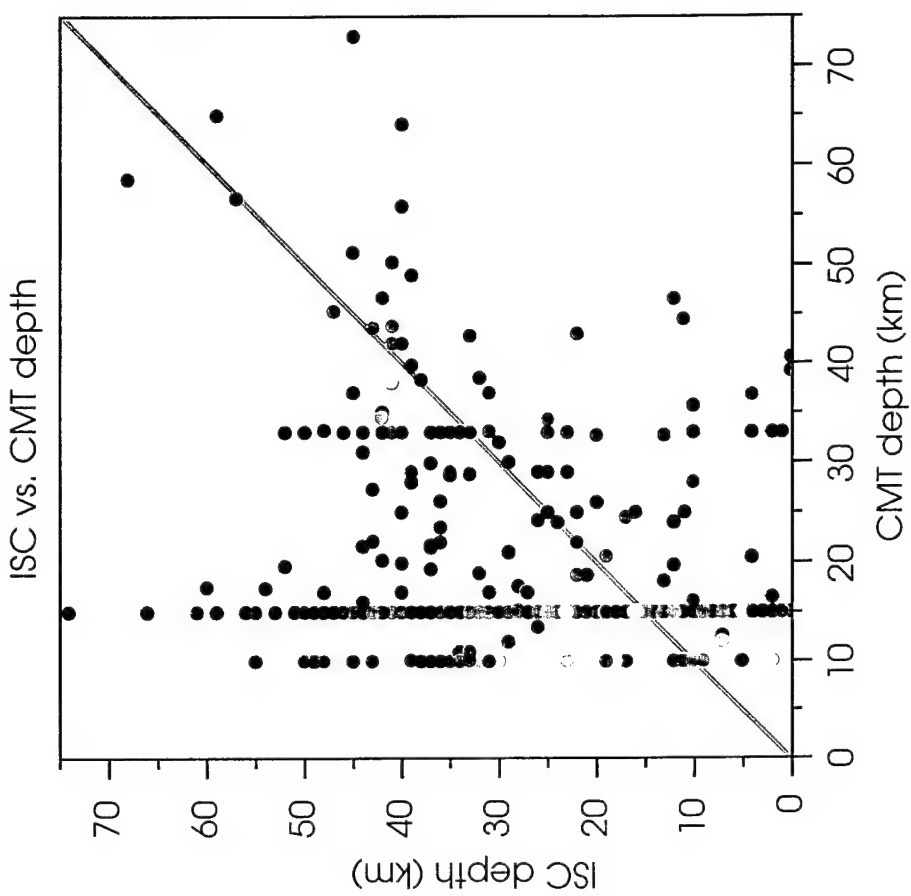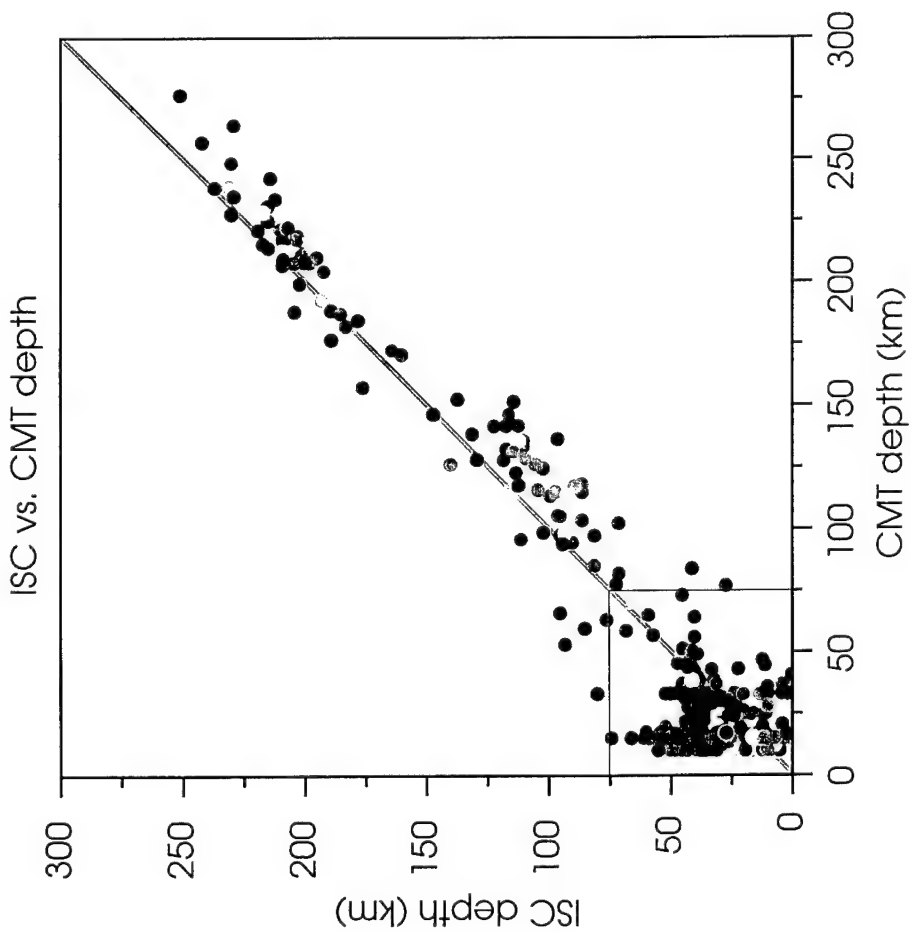
Figure 4 Comparison of depths between the ISC and the Harvard CMT catalogs. The colours correspond to the size of the events, ranging from red for large events (Mw=7) via green and blue to purple for small events (Mw=5). The box in the left panel is shown enlarged in the right panel. The grey line corresponds to the ISC and Harvard depths being equal.

7

broadband properties of the various phases essential in recognizing source depth. This is discussed in the third section on waveform modeling and the development of a good average regional model. Section 4 deals with the issue of source discrimination and Section 5 with the compatibility of regional and teleseismic data in terms of locating events and calibrating paths. We conclude with a general discussion and a brief plan of future work on using the AAK and/or NIL broadband data to locate and discriminate events as a stand-alone system.

2. Source Parameters from Regional Seismograms

Significant progress has been made in retrieving source mechanisms from regional broadband seismograms. A consequence is that the magnitude threshold can be lowered to moderate-to-small sized events ($M_w = 3.5$, Zhu and Helmberger, 1996). Because of the frequent occurrence and relatively simple source functions of earthquakes in this magnitude range, their waveforms are ideal for calibrating path effects and investigating regional structures.

Two kinds of regional waveform data are used for source estimation; surface waves (Patton, 1980; Thio and Kanamori, 1995) and body waves (Wallace and Helmberger, 1982; Fan and Wallace, 1991; Fan *et al.*, 1994; Dreger and Helmberger, 1993). Generally, body waves are less affected by shallow heterogeneities and are more stable compared to surface waves. However, they also tend to have lower signal-to-noise ratio than surface waves due to their smaller energy. There are also several recently proposed inversion methods that use the entire waveform (Walter, 1993; Ritsema and Lay 1993; Zhao and Helmberger, 1994). However, these inversions are mainly controlled by surface waves because most of them only invert the long period waveforms. An exception is the method by Zhao and Helmberger (1994) which breaks the broadband waveform into *Pnl* and surface wave segments and inverts them independently. One of the advantages of this method is that it takes into account the imperfect 1-D regional velocity model and the lateral structural variation by allowing time shifts between portions of recorded and synthetic seismograms. The solution is obtained by applying a direct grid search through the source parameter space to find the global minimum of misfit between the observed and synthetic seismograms.

Thus, source estimation from regional records can be very accurate with only a few stations if the Green's functions are well enough known (Dreger and Helmberger, 1993). Unfortunately, the more detailed the Green's functions, the more restricted its application. This proves especially true for shallow events where 3-D geology becomes important. Thus, working with very simple Green's functions allows a much broader application if the essential physical phenomenon of P_{nl} waves and surface waves is still included. For periods less than 50 secs and ranges less than 10°, we find that a single surface layer is enough to explain the fundamental Rayleigh wave and surface coupled PL waves, (Helmberger and Song, 1995). The crustal wave guide plays a more important role for the body waves as well as the Love wave. If we are interested in relatively larger ranges, beyond 300 km, the detail of Moho sharpness becomes less important for modeling shallow events. Crustal gradients do affect the time separation between P_{nl} waves (the extended P wavetrain) and the surface waves, but this effect can be handled by the so-called "cut-and-paste" method as discussed above. This approach is followed here by using the model determined by Zhu and Helmberger (1995) for the Tibetan Plateau. The model has two layers over a half space as given in Table 1. The P-SV system of synthetics at a range of 400 km is displayed in Figure 5 for crustal events and in Figure 6 for the deeper events. We want to model any observed seismogram, $u_i(t)$, by fitting it with $s_i(t)$;

$$s_i(t) = M_o \sum A_{ij} (\phi - \ominus, \delta, \lambda) \; G_{ij} \; (z). \tag{1}$$

where the G_{ij}'s are taken from a Green's function library, as in Figures 5 and 6. Here $i = 1,2,3$ corresponds to the vertical, radial, and tangential components of motion and the j's correspond to the three fundamental faults; strike-slip, dip-slip, and 45° dip-slip. The A's contain the relative weighting of these three functions and are determined by applying a direct grid search, where the misfit error

$$e \equiv \left(\frac{r}{r_o} \right)^p \; \| \; u \bullet s \; \| \tag{2}$$

is minimized. We find that assuming the usual geometrical spreading of $p = 1$ for the body wave (P_{nl}) and $p = 0.5$ for the surface waves does a good job in equalizing the seismograms at different ranges. In this way the more distant observations are weighted similarly to the closer observations. This norm is very tolerant of errors in the Green's functions in that even if the

Table 1: 1-D velocity model of the Tibetan

layer	Th (km)	$V_p(km/s)$	$V_s(km/s)$
1	4	4	2
2	60	6	3
3	--	8	4

Table 2: Locations of the events from the ISC catalog

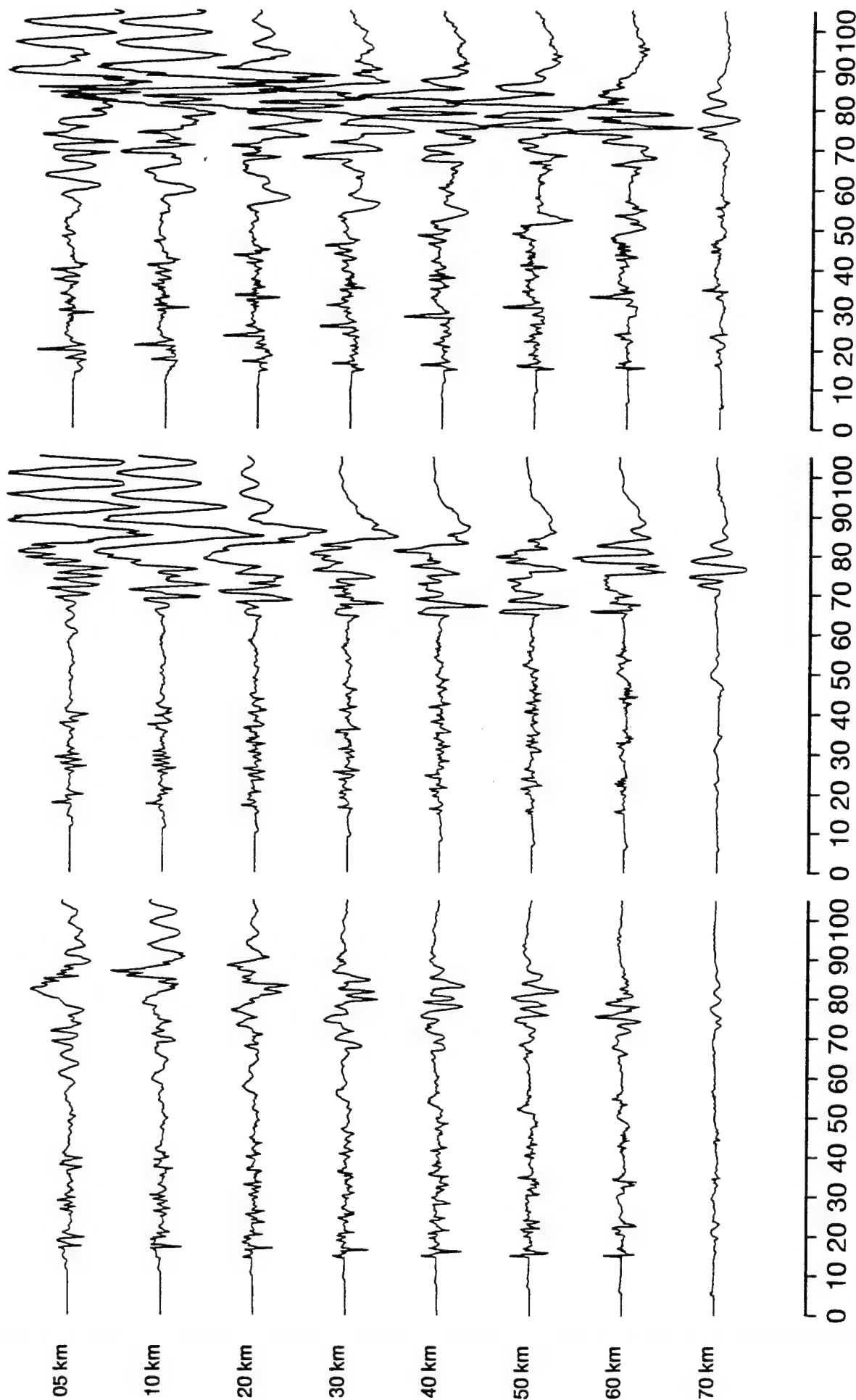| Event	Date	Origin Time h:m:s	Lat.°N	Long.°E	Depth (km)	m_b
276	10/2/1992	14:38:46.4	38	73	139	5
289	10/15/1992	02:42:06.7	39	72	16	5
289	10/15/1992	19:42:13.8	38	74	157	4
311	11/6/1992	07:21:56.0	41	72	21	5
311	11/6/1992	17:58:39.0	34	69	25	5
317	11/12/1992	20:41:05.2	36	70	204	6
322	11/17/1992	02:38:50.7	33	67	35	5
328	11/23/1992	23:11:06.9	38	72	43	6
339	12/4/1992	11:36:35.5	37	72	114	6
341	12/6/1992	03:44:29.3	37	72	122	6

Figure 5   Display of strike-slip (SS), dip-slip (DS) and 45° dip-slip (45° DS) vertical component synthetics at a distance of 400 km, where the depth varies from 5 to 70 km. The model is given in Table 1.
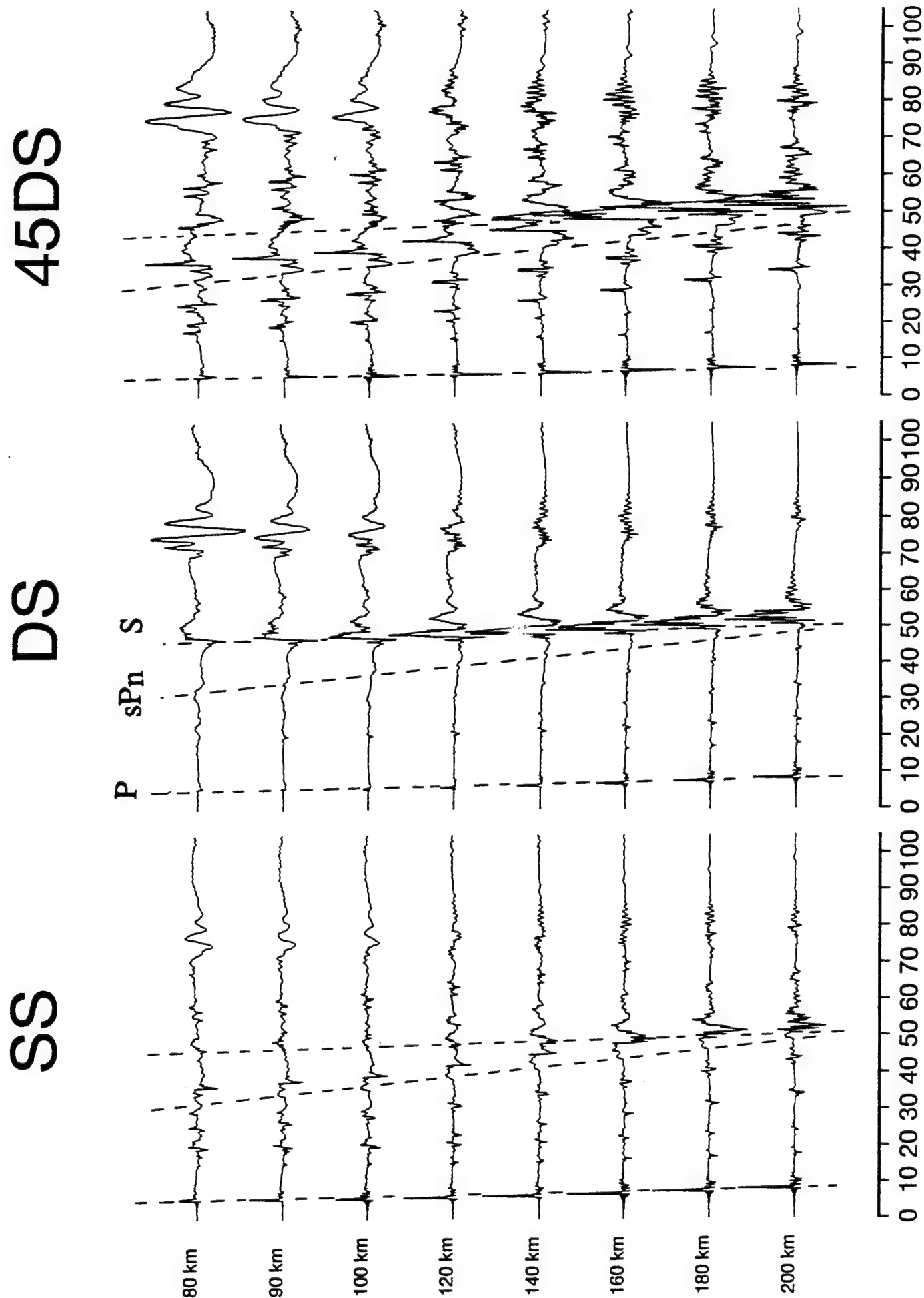
11

Figure 6   Continuation of Figure 5 to a depth of 200 km.

12

waveforms do not fit well, the amplitude information is still adequate for estimating a source orientation.

Since we model the seismograms in true amplitude, we have preserved this feature in the figures. Thus, the surface waves are very large for shallow events except for the strike-slip case which look similar to explosion Green's functions (Saikia *et al.*, 1992, and Zhao and Helmberger, 1995). The Green's functions at a depth of 70 km are just below the crust and lack the high-frequency signals trapped by the wave guide. The P-waves in this case have a long-period contribution which appears step-like and is caused by head-wave energy (Zhu and Helmberger, 1995). As the depth increases, the synthetics become increasingly simple, essentially reducing to just a P-wave and SV-wave, as shown in Figure 6. However, there is still important information about polarity and relative strengths of the phases. At shallower depths the phases pP_n and pP_mP develop and add useful waveform discriminating information. These features are absent in the dip-slip case since there is an SV-node at a 45° take-off angle.

Synthetics for the corresponding tangential field are quite simple and have been presented in Zhu and Helmberger (1995) for this particular model in connection with modeling some deep events beneath Tibet that are not included in this study.

We applied this source estimation code to the 10 events given in Table 2. The data set comes from two broadband arrays: the KNET array (see Pavlis and Mahdi, 1995) and the Pakistan Himalayas array PAKN (see Sandvol *et al.*, 1994). All the velocity records from these two arrays were integrated into displacement and band-passed filtered between 5 to 100 secs before attempting the source inversion. The locations and mechanisms of these events are displayed in Figure 7 along with the CMT solutions that are available. The two types of solutions are in good agreement with respect to mechanism and seismic moment.

2.1 Crustal Events

For convenience, we have divided the source solutions into two groups: shallow and deep events. Figure 8 presents the crustal source estimates for the two arrays, separately and together. These results display the best fitting mechanisms as a function of depth with the size of the beach

13
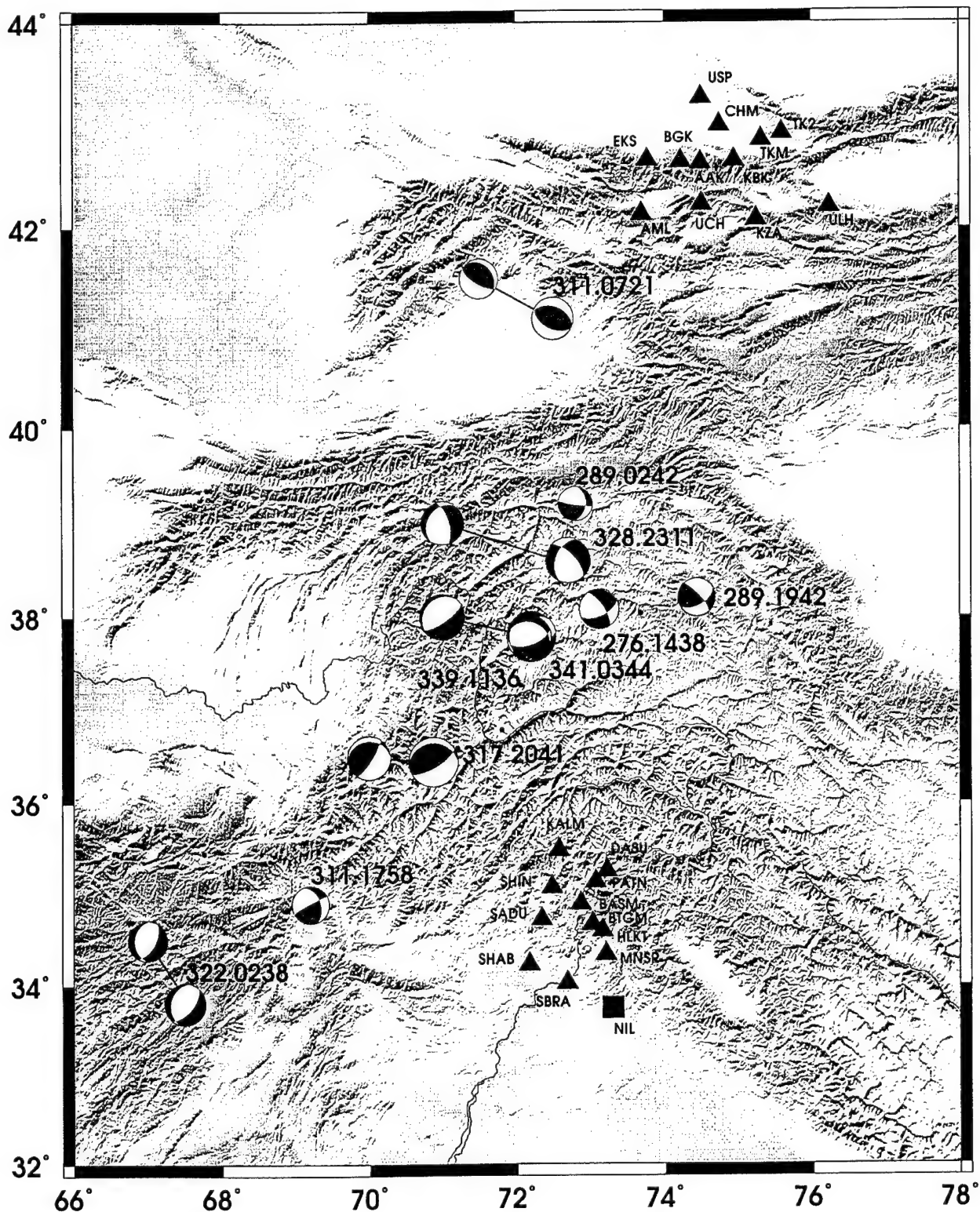
Figure 7   Locations of events (focal spheres) and broadband stations of KNET and PAKN (triangles). The CMT (Harvard) solutions for several large events are displayed to the left of our corresponding solution
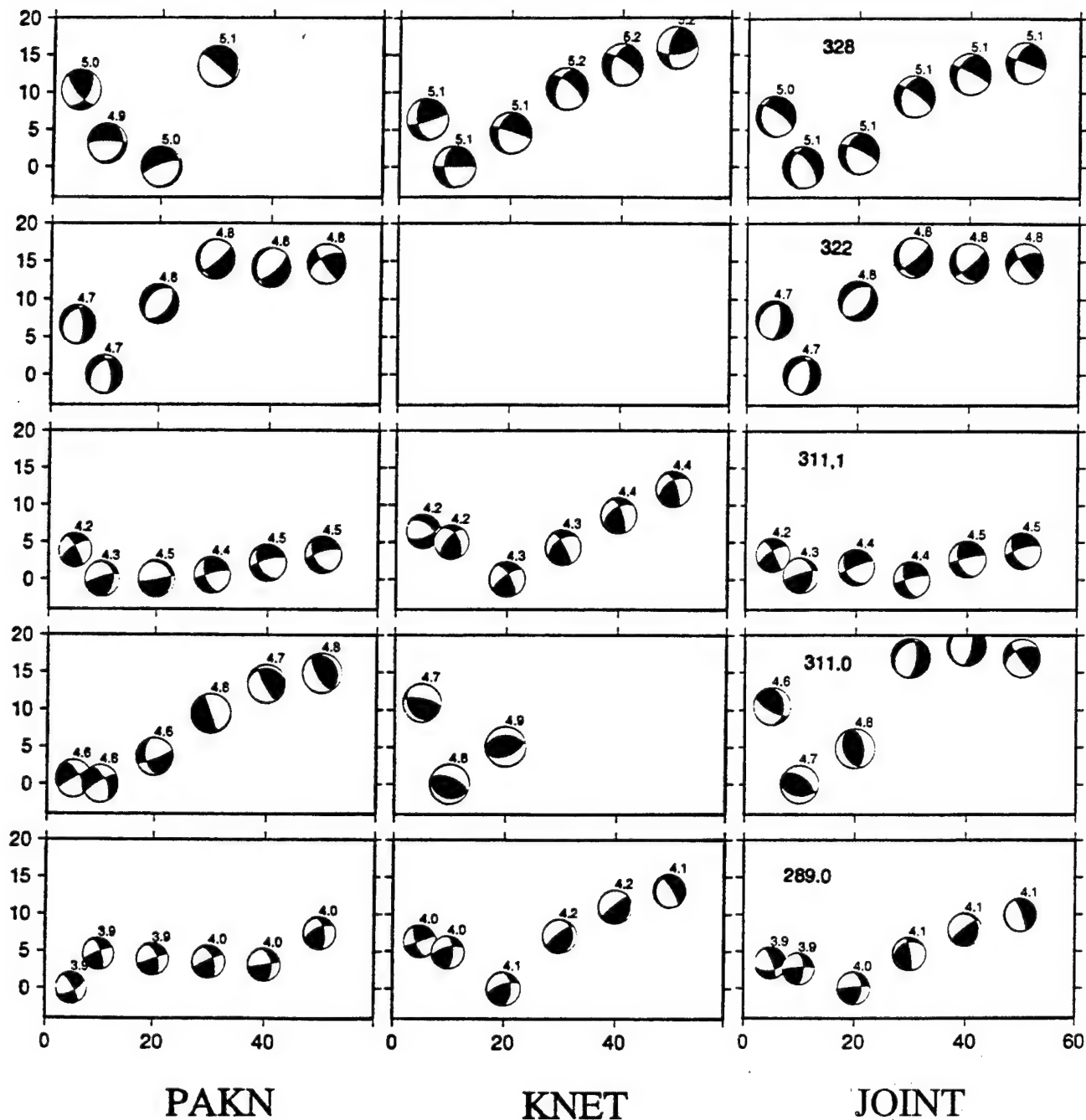
Figure 8   Display of misfit errors for the five shallow events as a function of depth. Solutions using the separate arrays are given on the left with the joint solution on the right.

ball indicating the relative moment. The source mechanisms are very stable over large depth ranges. For most shallow events (Figures 9 through 13), the waveform misfit errors have well defined minima. The only exception is event 311.1758 which is relatively small (M_b = 4.5) and only recorded by PAKN.

One of the best recorded shallow events is the magnitude 5.1 earthquake 328.2311 which occurred at about an equal distance between the two arrays. Figure 9 displays the observations and the synthetic fits for the best source depth estimate of 10 km. The surface waves (Love vs Rayleigh) are about equal size indicating a mixed mechanism and the overall fit is excellent as indicated by the low misfit error. The relative strengths of the two types of surface waves plays a key role in fixing the depth. Event 322.0238, shown in Figure 10, is also well modeled except the synthetic P_n does not have the strength of the observations. A positive upper-mantle gradient is needed to correct this. The neighboring event 311.1758 is displayed in Figure 11. These ranges are not very far past critical angle and are less effected by the mantle gradient. Note that all the P_{nl}'s have been fit separately as discussed above. We have omitted the actual time shifts to keep the figures simple. However, for these two events, (Figures 10 and 11), the model appears to be too slow. Thus, we had to shift the complete synthetics forward by 4 secs along with individual station shifts. For the P_{nl} fit at SHAB (event 311.1758) the synthetic is late by 5.8 secs whereas at DASU only a 4.4 sec shift was required. The corresponding Love wave shifts are 7.8 and 4.8. Much of this behavior is caused by 3-D geology, but at this stage these shifts will be viewed as baseline time corrections, since we do not necessarily know the location or origin time. Note that trade-offs between depth and origin time are quite serious for this region, (Zhao and Helmberger, 1991). They find that throughout the Tibetan Plateau crustal events systematically are located too deep by about 15 km and occur about 4 sec earlier than reported in PDE.

Many of the crustal events in this region are too small to be recorded well teleseismically and do not have CMT solutions. However, three of the events studied here have Harvard solutions with results included in Table 3 and mechanisms displayed in Figure 7. The mechanisms are quite good but the depths disagree as in the earlier study of events beneath Tibet.

Event 328.2311 model t92_10 strike 190 dip 40 rake -50 moment 5.1 error 2.63e-02 shift0 -999
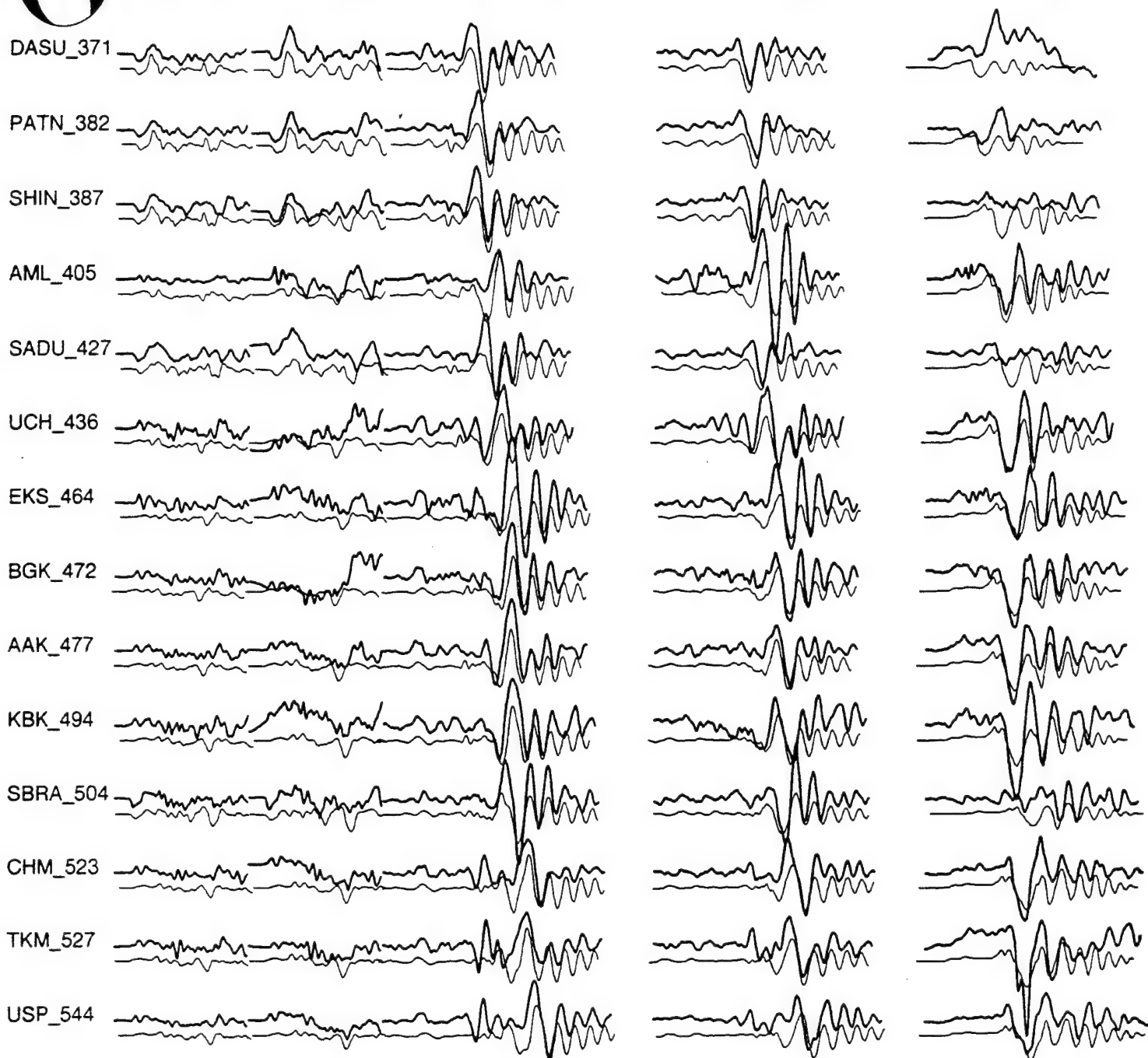
Figure 9   Comparison of the best fitting synthetics vs. observations for the 328.2311 event with parameters given at the top of the figure; model t 92 refers to the model used (Table 1), the next number states the best depth estimate followed by the strike, dip and rake angles, the moment magnitude M_w and the misfit error. Note that the vertical and radial P_{nl} have been separated from the surface waves and plotted on the left. The amplitudes are scaled to the largest amplitude in the top set of traces with both synthetics and observations multiplied by the assumed spreading corrections; r for P_{nl} and square-root-of r for surface waves.

Event 322.0238 model t92_10 strike 220 dip 40 rake -60 moment 4.7 error 5.61e-03 shift0 -999
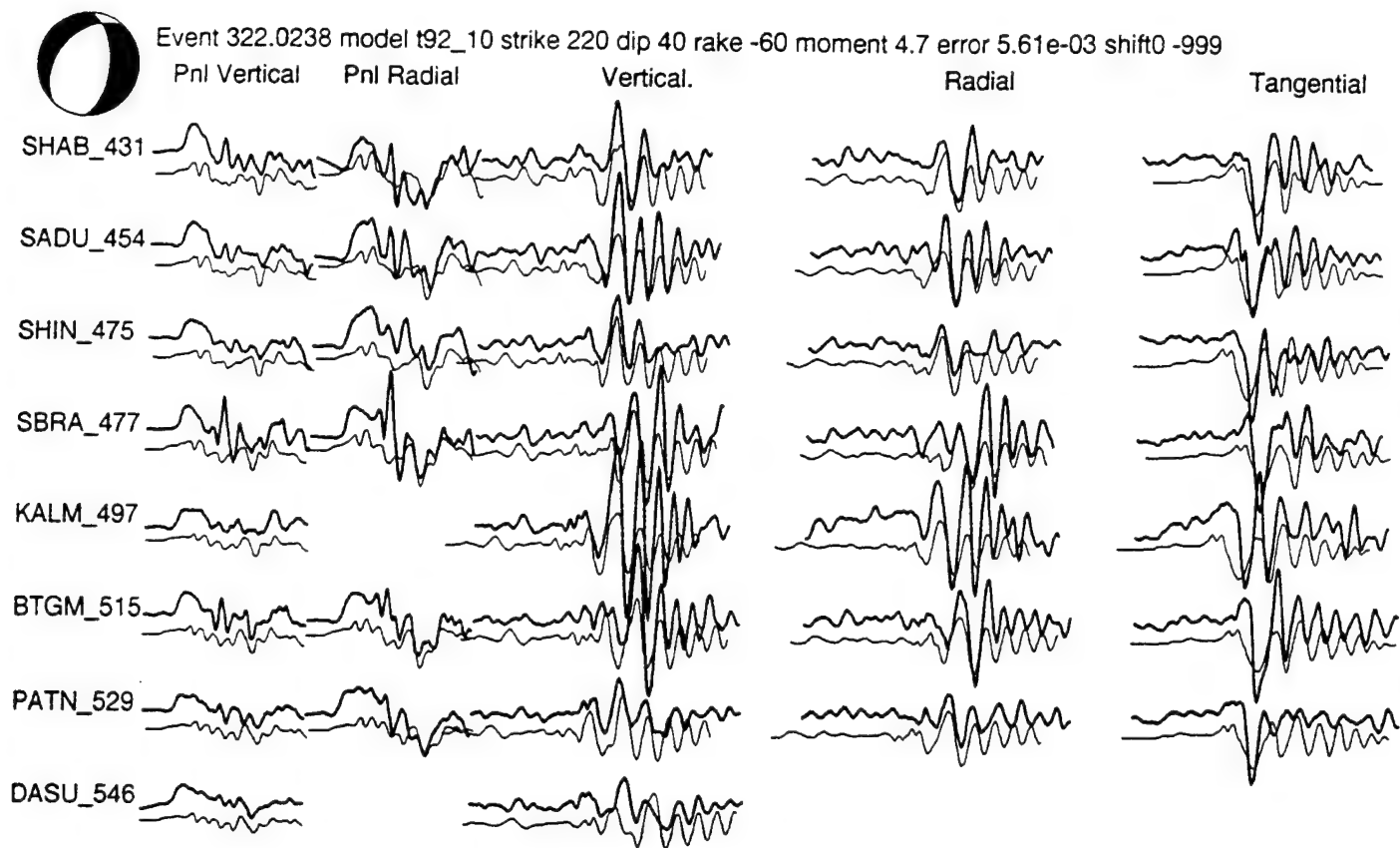
Figure 10   Source inversion results for event 322.0238.

Event 311.1758 model t92_30 strike 160 dip 60 rake -10 moment 4.4 error 1.83e-03 shift0 -999
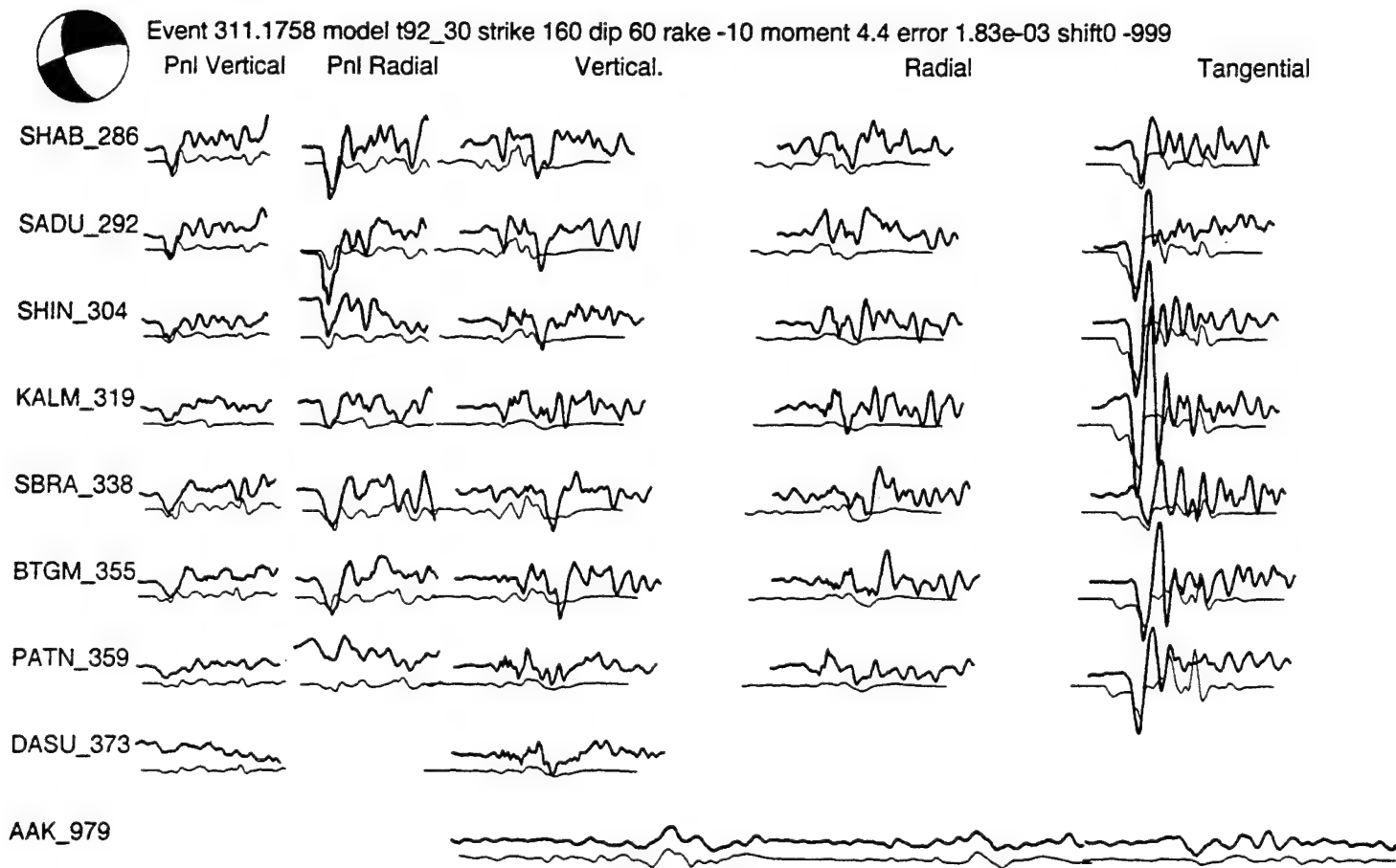
Figure 11   Source inversion results for event 311.1758 with only AAK available from the KNET.

18

Event 311.0721 model t92_10 strike 100 dip 40 rake 70 moment 4.7 error 1.25e-02 shift0 -999
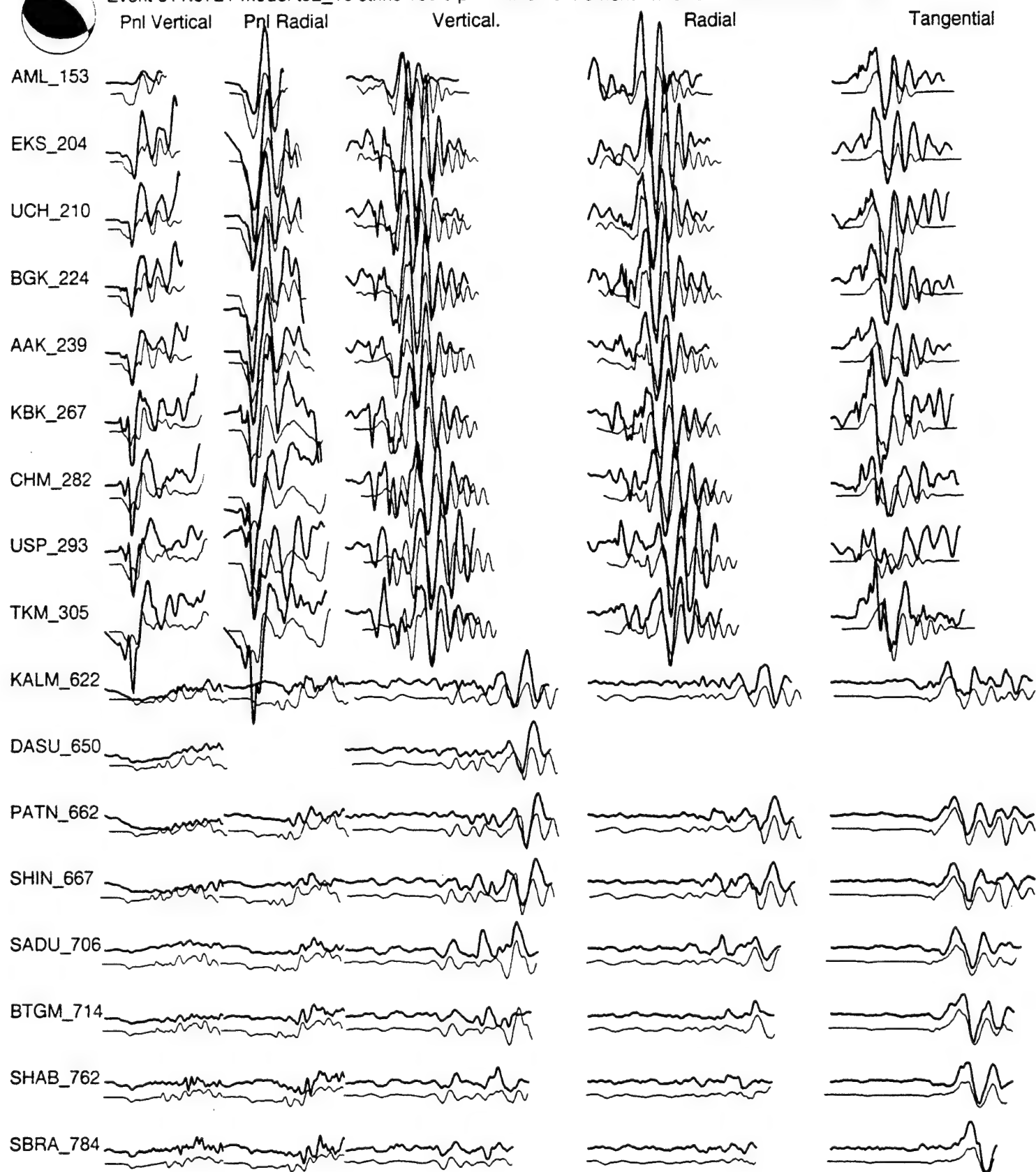
Figure 12   Source inversion results for event 311.0721.

19

Event 289.0242 model t92_20 strike 0 dip 50 rake 10 moment 4.0 error 6.44e-04 shift0 -999
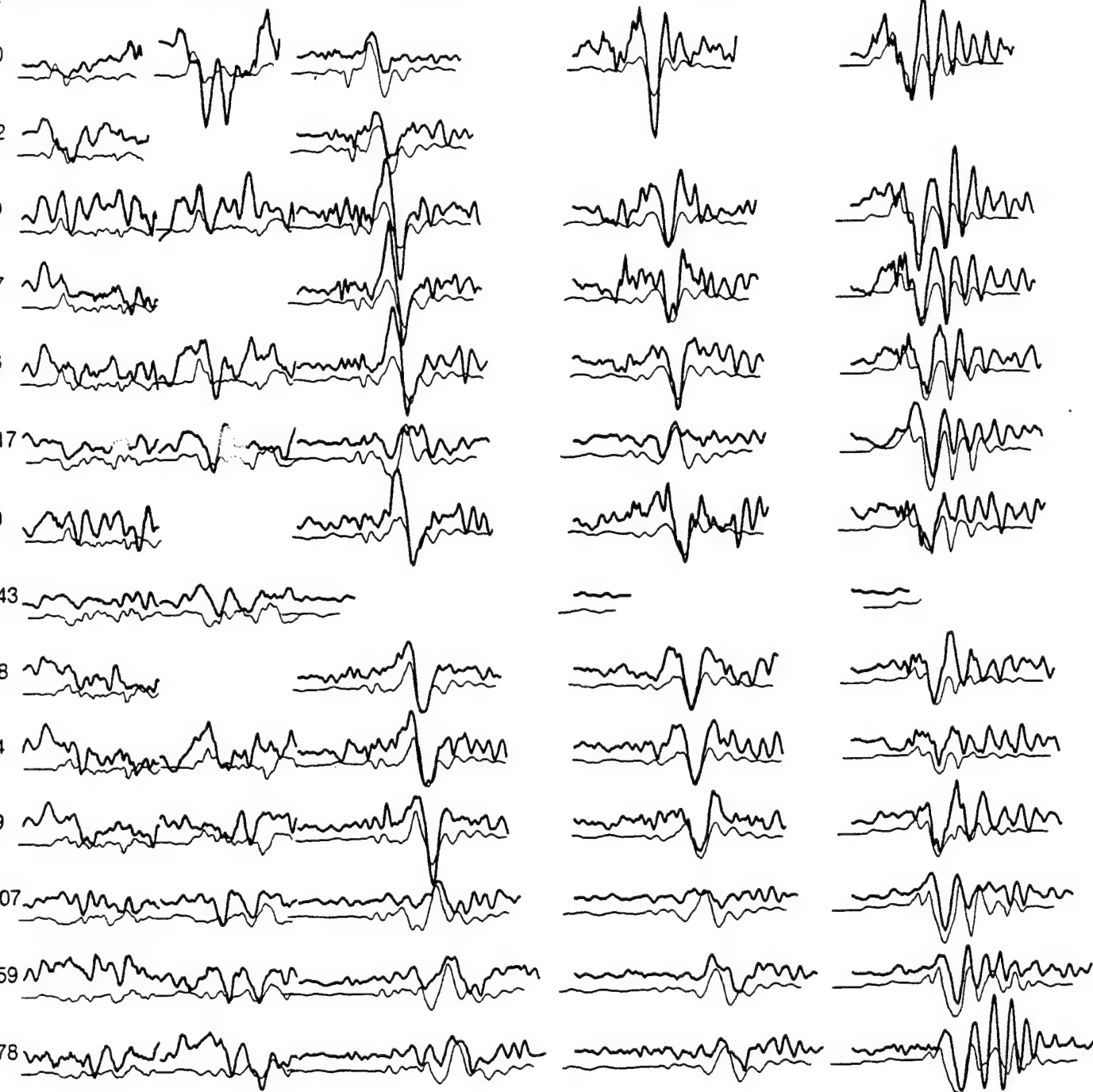
Figure 13 Source inversion results for event 289.0242.

Table 3: Focal depths and fault plane solutions from waveform modeling

Event	strike	dip	rake	h (km)	M_w	HCMT	H(km)
276.1438	330	80	-20	160	4.4		
289.0242	0	50	10	20	4.0		
289.1942	60	60	20	180	4.2		
311.0721	100	40	70	10	4.7	4.3	(19)
311.1758	160	60	-10	30	4.4		
317.2041	70	70	80	180	5.5	4.9	(188)
322.0238	220	40	-60	10	4.7	4.4	(33)
328.2311	190	40	-50	10	5.1	4.9	(44)
339.1136	70	60	-80	120	5.5	5.1	(131)
341.0344	290	40	-50	120	4.8		

M_w = Moment Magnitude
HCMT = Magnitude from Harvard Centroid Moment Tensor
H = Harvard Depth
h = Depth from Regional Waveform Modeling (This Study)

2.2 Mantle Events

The source parameter estimates for the deep events are given in Figure 14 following the same format used earlier for shallow events. The depth resolution for deep events is generally better in comparison to crustal events. This will be examined in more detail in Section 3. Part of the reason is that they do not generate surface waves which help to constrain the focal depths. Another reason is that the inversion uses the P and SV waves separately, so the S-P times are not employed to constrain focal depths. However, as we will discuss in more detail later, we have observed several distinguishing depth phases that can be used to determine the focal depth. The waveform comparisons are given in Figures 15 through 19.

3. Regional Modeling

The geological structure between the two arrays is probably amongst the most complex on the earth. It contains very young high mountains, the western Himalayan Syntax, major boundary faults, sutures, and two subduction zones. Mapping out the true 3-D structure, while highly interesting, is quite impossible given the current data coverage and resources. Thus, we will attempt to idealize the structure in a manner that allows the best use of the two permanent broadband stations NIL and AAK in future efforts of source location and identification. Since the KNET data has been studied by numerous investigators, Pavlis and Mahdi (1995), and others, we will concentrate mostly on the PAKN array data which has not been studied except for some analyses of anisotropy by Sandvol et al. (1994). Reconnaissance work by Barazangi et al. (1995) indicates that the crust is roughly uniform beneath the higher Himalayas and Karakorum Mountains to the north (Figure 20a) with some detail to the east and to the west. The northern most KNET stations seem to be significantly off the Plateau, and the structure can be 3-D like which may potentially complicate wave propagation characteristics. In this study we use equivalent 1-D model to explain the stable features in the waveforms. A high resolution map of the PAKN stations (Figure 20b) indicates a similar problem but the observations from the southern most stations SHAB and SBRA appear quite compatible with the other stations and have been included. Note that the station SBRA is quite close to NIL, a GSETT-3 β station essential to future studies.

22
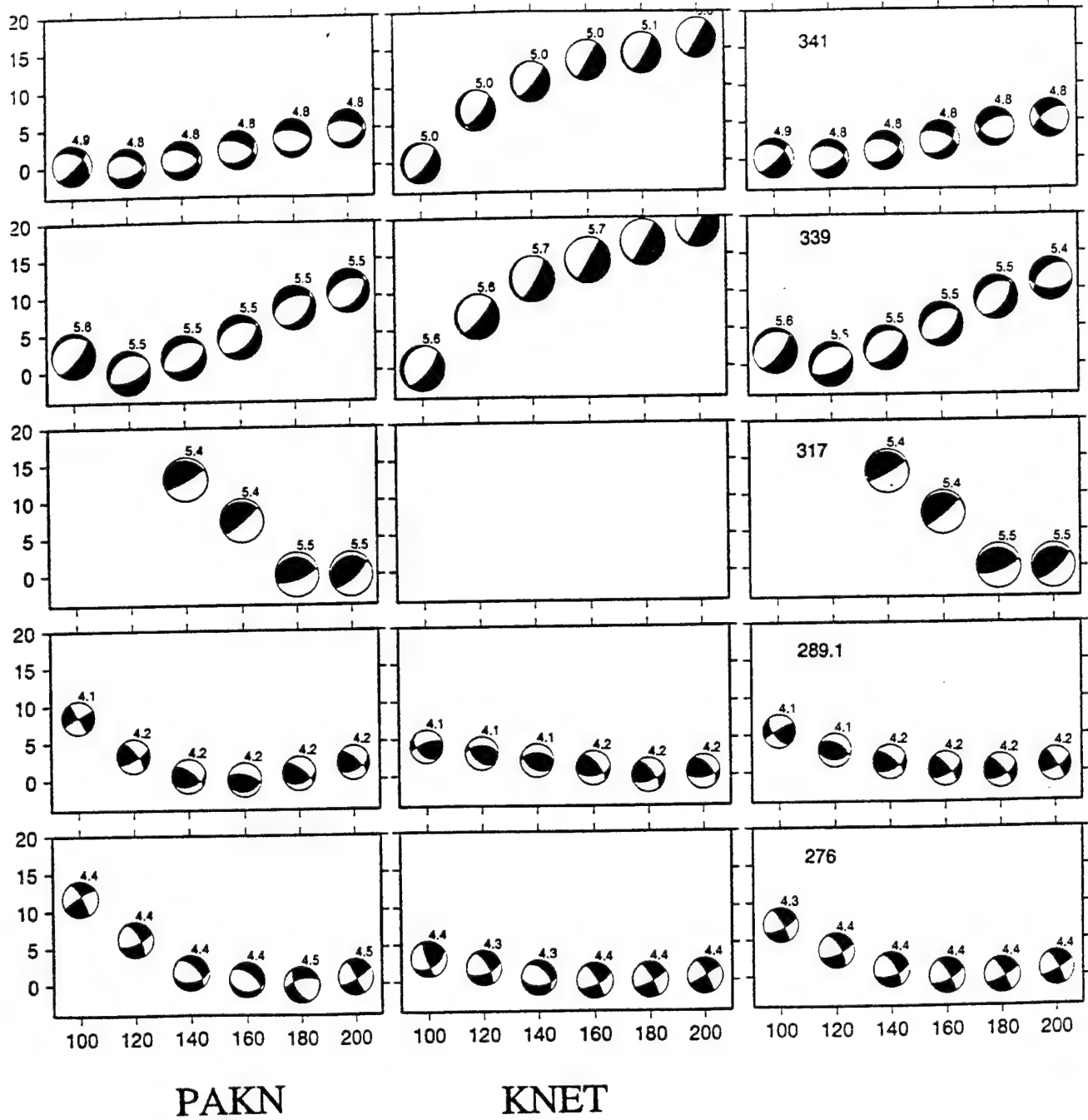
Figure 14 Comparison of misfit errors as a function of depth for the deep events. These solutions do not show strong minima because the strongest constraint, namely $(sP_n - P)$ is not used in the source parameter inversion.

Event 317.2041 model t92_180 strike 70 dip 70 rake 80 moment 5.5 error 1.76e-02 shift0 -999
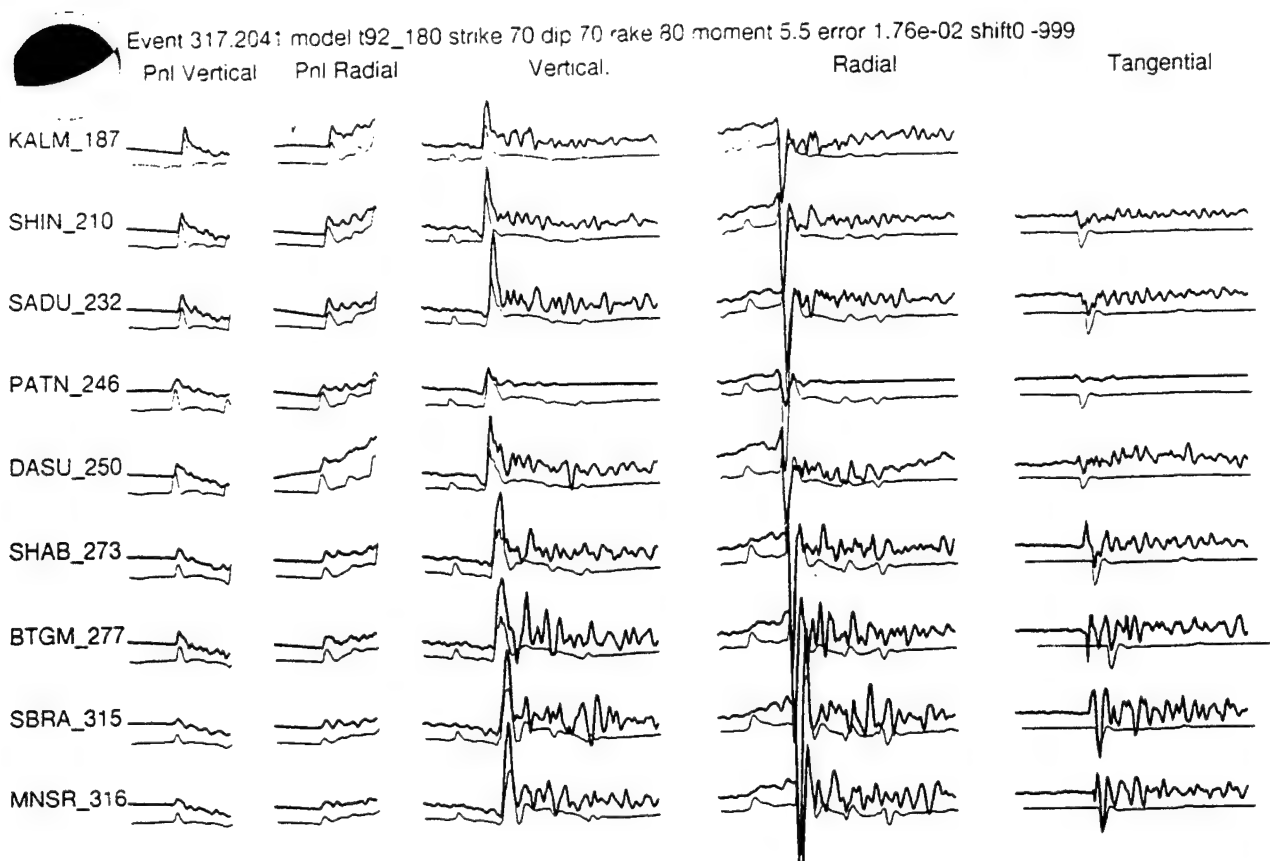
Figure 15 Source inversion results for event 317.2041 where only the PAKN data were available.

Event 339.1136 model t92_120 strike 70 dip 60 rake -80 moment 5.5 error 4.19e-02 shift0 -999
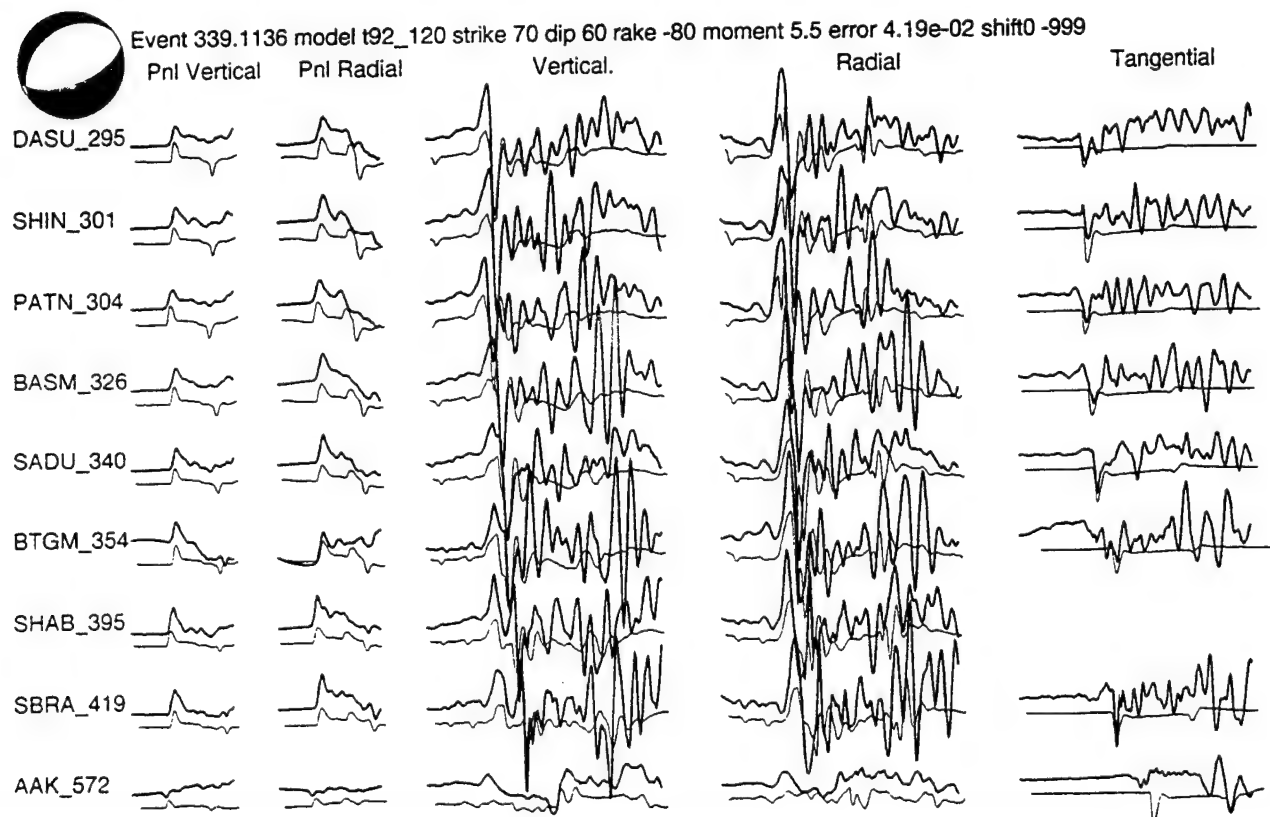
Figure 16 Source inversion results for event 339.1136 with only AAK available from the KNET.

24

Event 276.1438 model t92_160 strike 330 dip 80 rake -20 moment 4.4 error 1.13e-03 shift0 -999
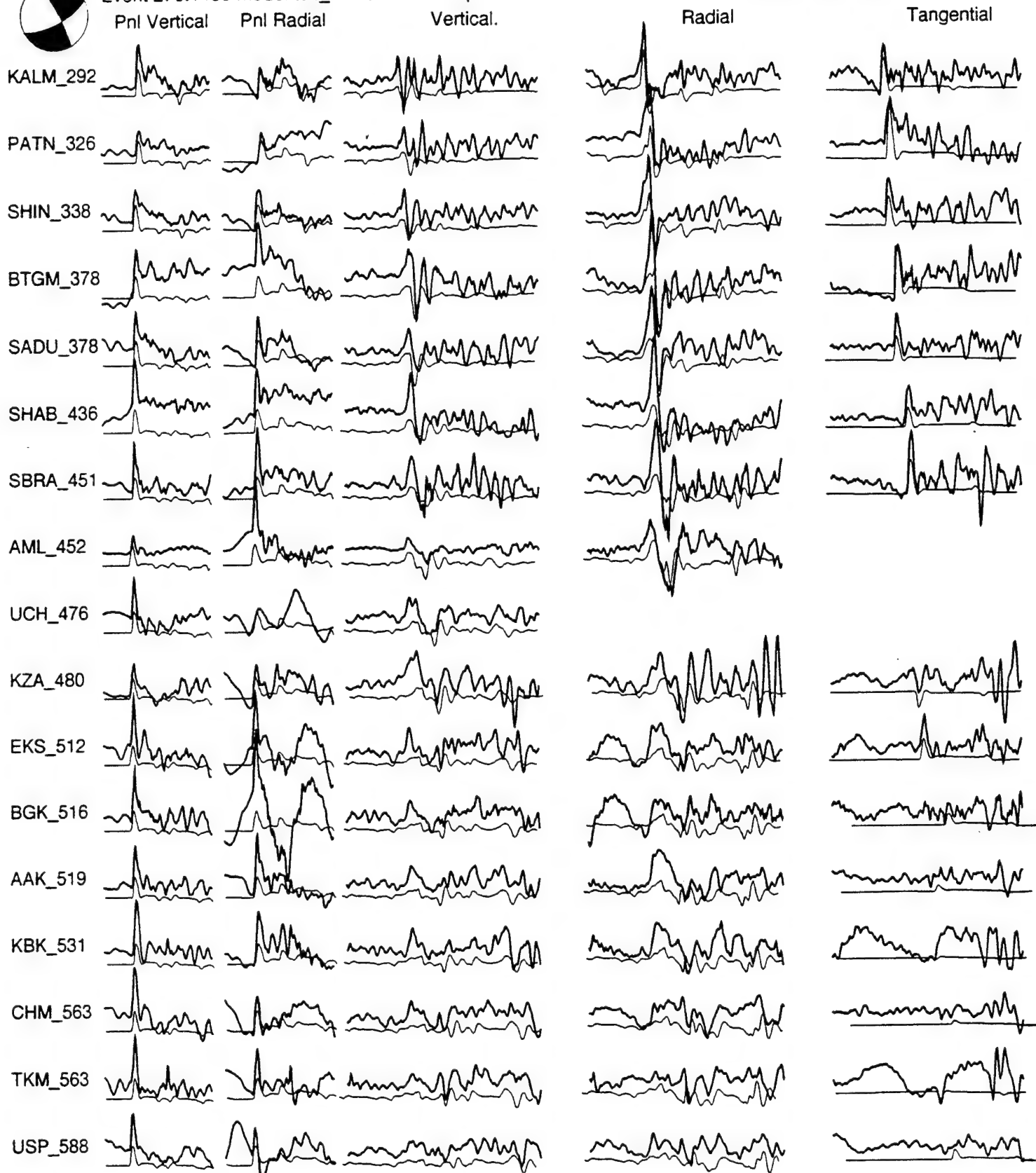
Figure 17   Source inversion results for event 276.1438. Note the long-period noise on the KNET horizontal components.

Event 289.1942 model t92_180 strike 60 dip 60 rake 20 moment 4.2 error 6.18e-04 shift0 -999
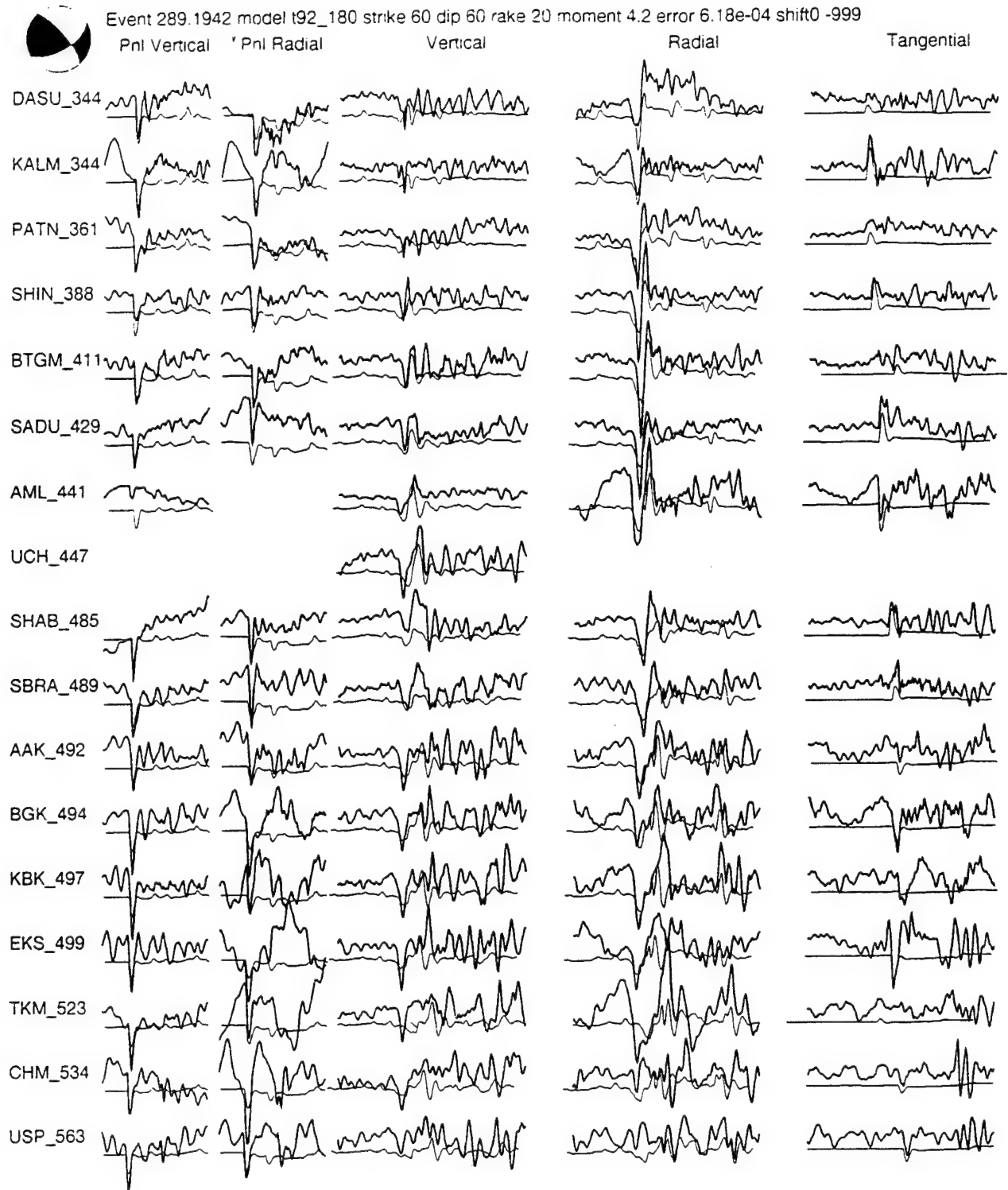
Figure 18 Source inversion results for event 289.1942, with strong noise on the radial and tangential components.

26

Event 341.0344 model t92_120 strike 290 dip 40 rake -50 moment 4.8 error 4.63e-03 shift0 -999
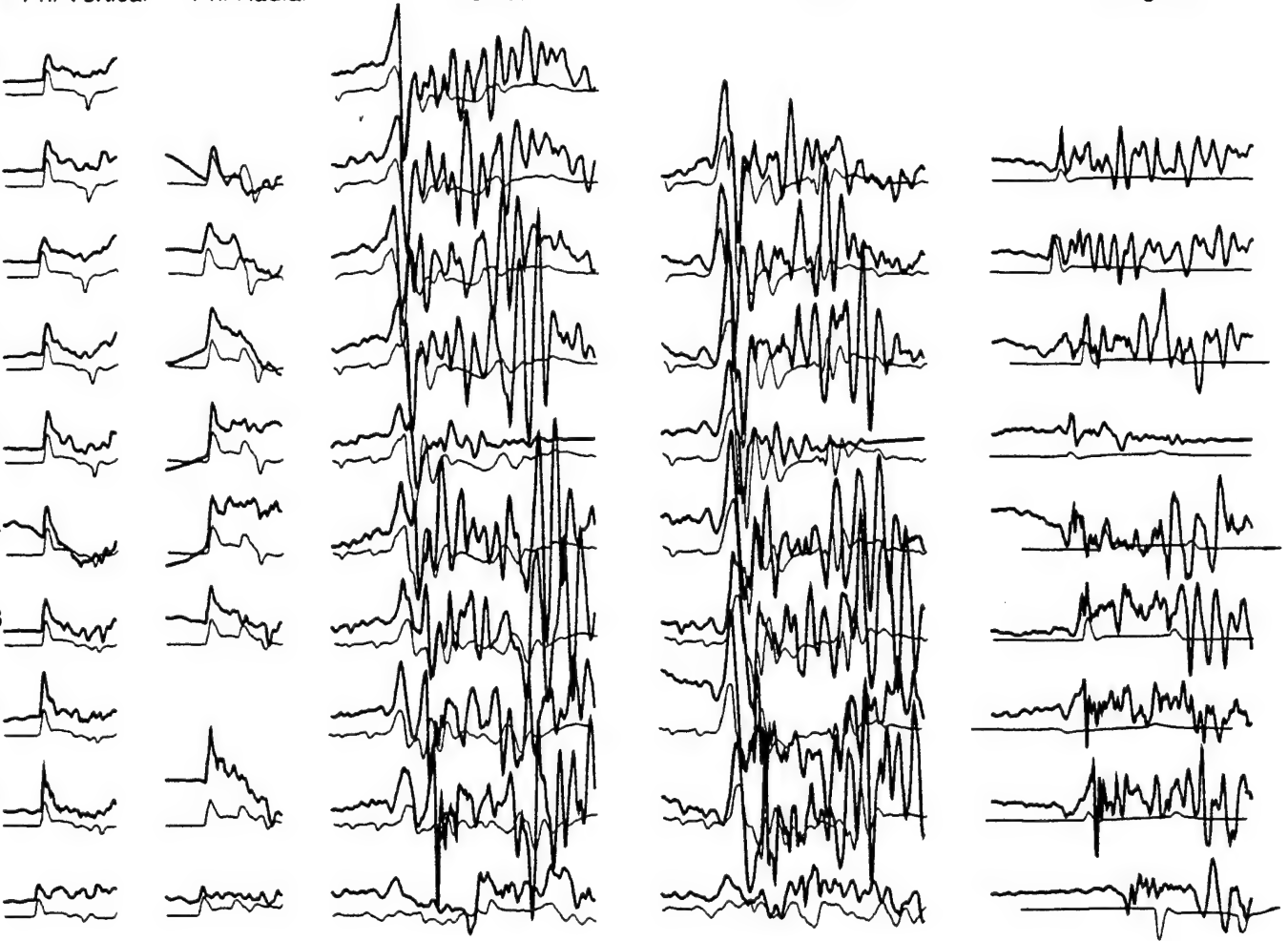
Figure 19 Source inversion results for event 341.0344.

27
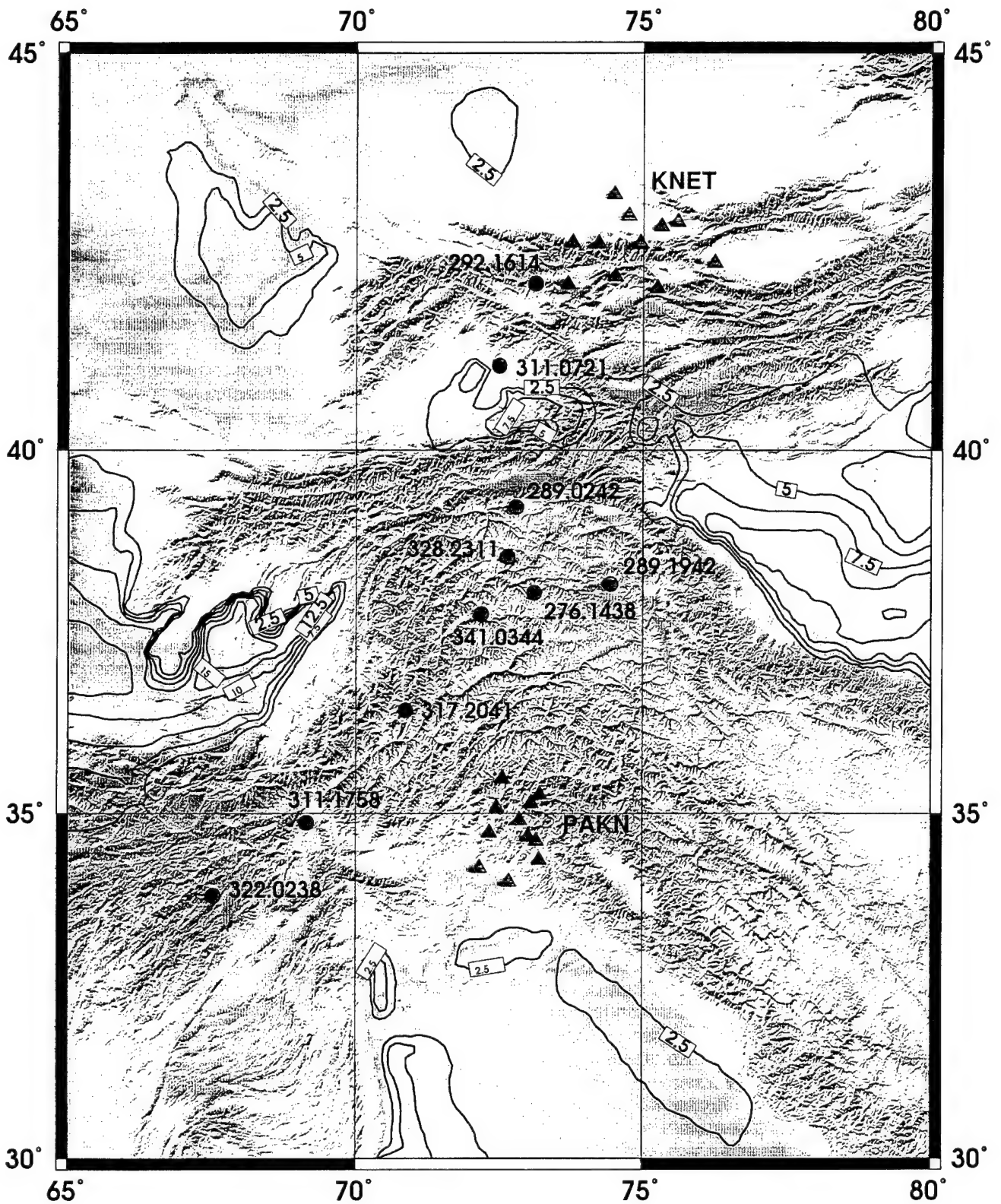
Figure 20a   High resolution topographic map of the study region superimposed on the depth-to-basement contours after Fielding et al. (1992).
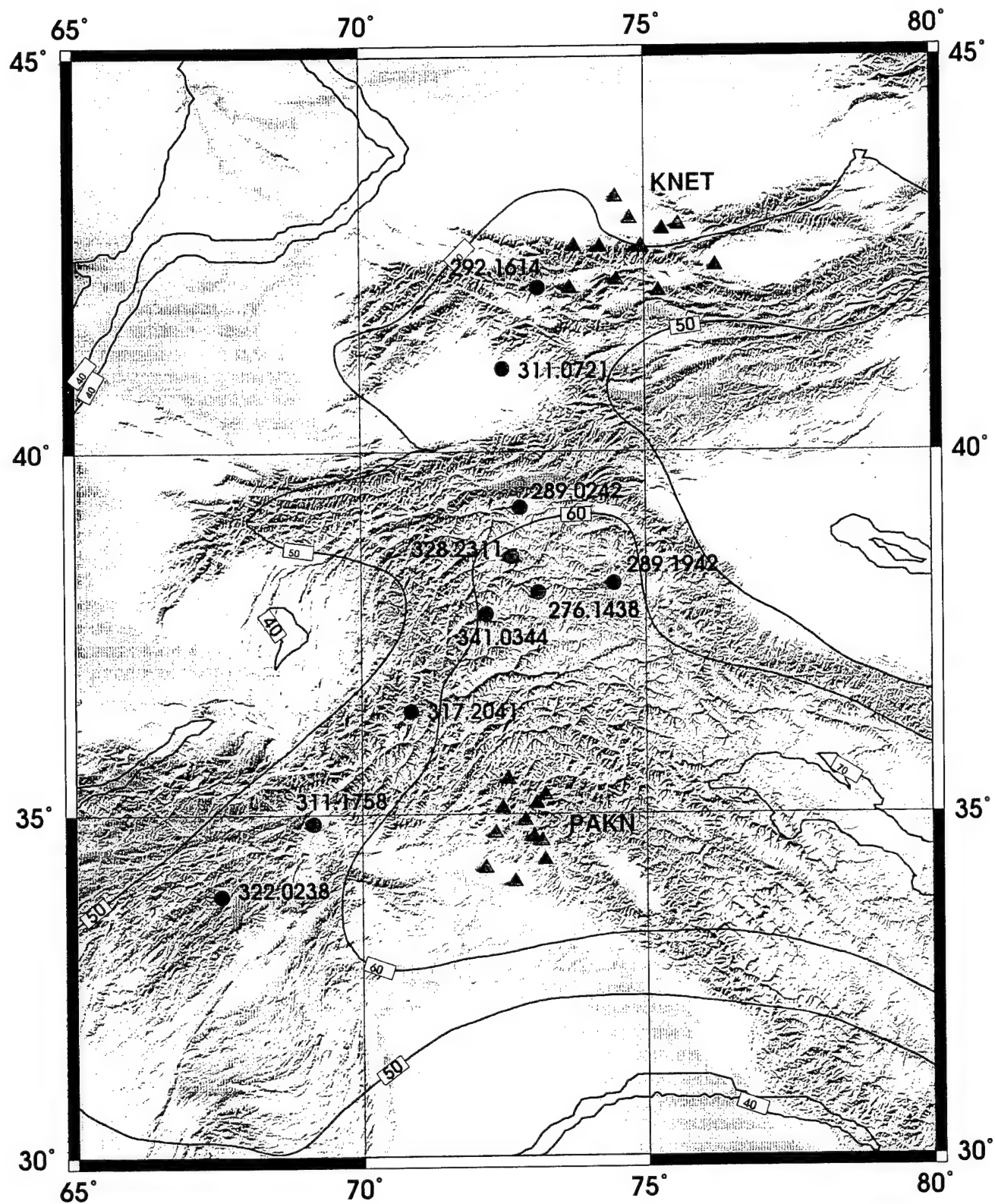
Figure 20b   High resolution topographic map superimposed on the Moho depth estimates, after Fielding et al. (1992).

29

3.1 Broadband Modeling of Depth Phases

The models developed in this section were derived following the direct waveform modeling method. This procedure is essentially a trial-and-error approach where one tries many possible models in an attempt to explain those features of the observations deemed most stable and useful in recognizing depth and source properties. The characteristics of these stable distinct phases can provide important clues towards the identification of seismic sources. We relied on two basic methods of generating synthetics: the reflectivity method which yields complete wavefield synthetics, and generalized ray theory (GRT) which provides quick estimates of timing and detailed waveform information for particular ray paths. The two methods used in conjunction prove highly complementary. An example of models developed in this fashion is discussed in Zhao and Helmberger (1993) in their study of Hindu-Kush events recorded at Garm. A particularly interesting phase noted in their study is the phase sP_mP which follows an S-wave path to the surface and which can become critical and develop a head wave sP_n because of the change to P. This phenomenon is well-recorded in both broadband data sets. Profiles of two deep events with different mechanisms are presented in Figures 21 and 22 displaying the prominence of this phase (indicated by dotted lines) on the long-period motions. Figure 23 presents the observations across the KNET from the latter event. While there appears to be more scatter occurring in the short-period wave propagation across the KNET, the sP_n phase is quite clear.

Since the separation between direct P and sP_n is quite diagnostic in depth estimation, we conducted a series of numerical experiments to develop a better appreciation of this phase and its relationship with direct SV. Figure 24 displays some of these results assuming the source parameters for the 276.1438 deep event (Figure 17). Column (a) contains the motions produced by the phases arriving at the surface layer leaving the source as SV. Those phases converted to P when crossing the moho arrive earlier and do not contribute in this window. The first arrival of these locally generated S to P converted PL waves is a P-headwave, P_n, travelling along the bottom of the surface layer. Many multiples of the P-SV system contribute but the P-waves dominate. The largest short-period phase is the direct S-wave, S_d. Only the first five bounces in this layer are included in this calculation so that the wavetrain following the S_d is incomplete but should be accurate up to S_d. Column (b) contains the results of (a) plus the ray path contributions from paths converting from S to P at the free-surface, sP_mP. Actually, this phase
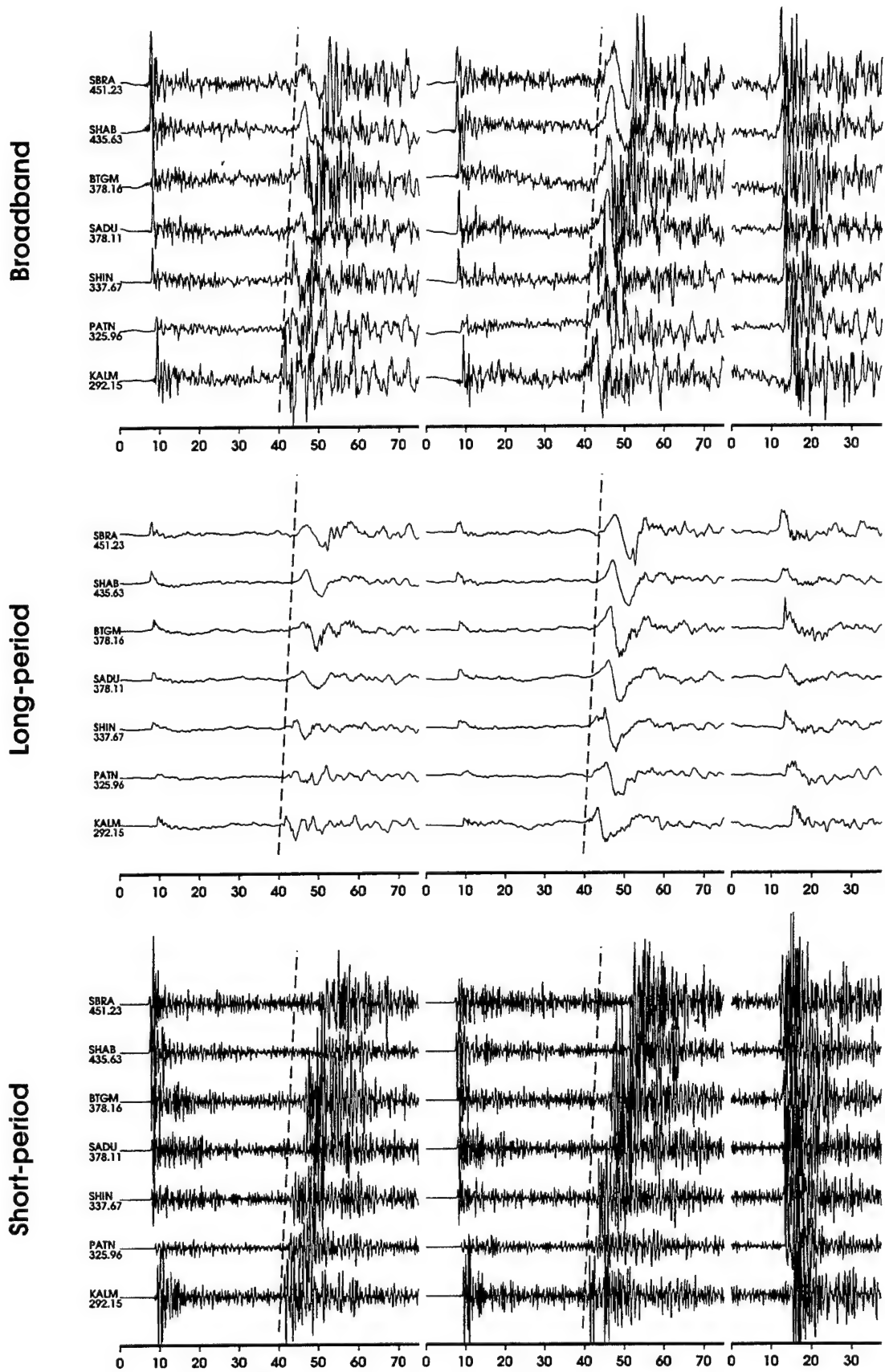
Figure 21   Presentation of PAKN observations for event 276.1438. Upper panel
displays the data broadband, middle panel after convolving with a lon-period instrument
(WWSSN) and the bottom panel assuming a short-period (WWSSN). Reference lines
have been added indicating the discordant behaiour between the short-period and long-
period response.

31
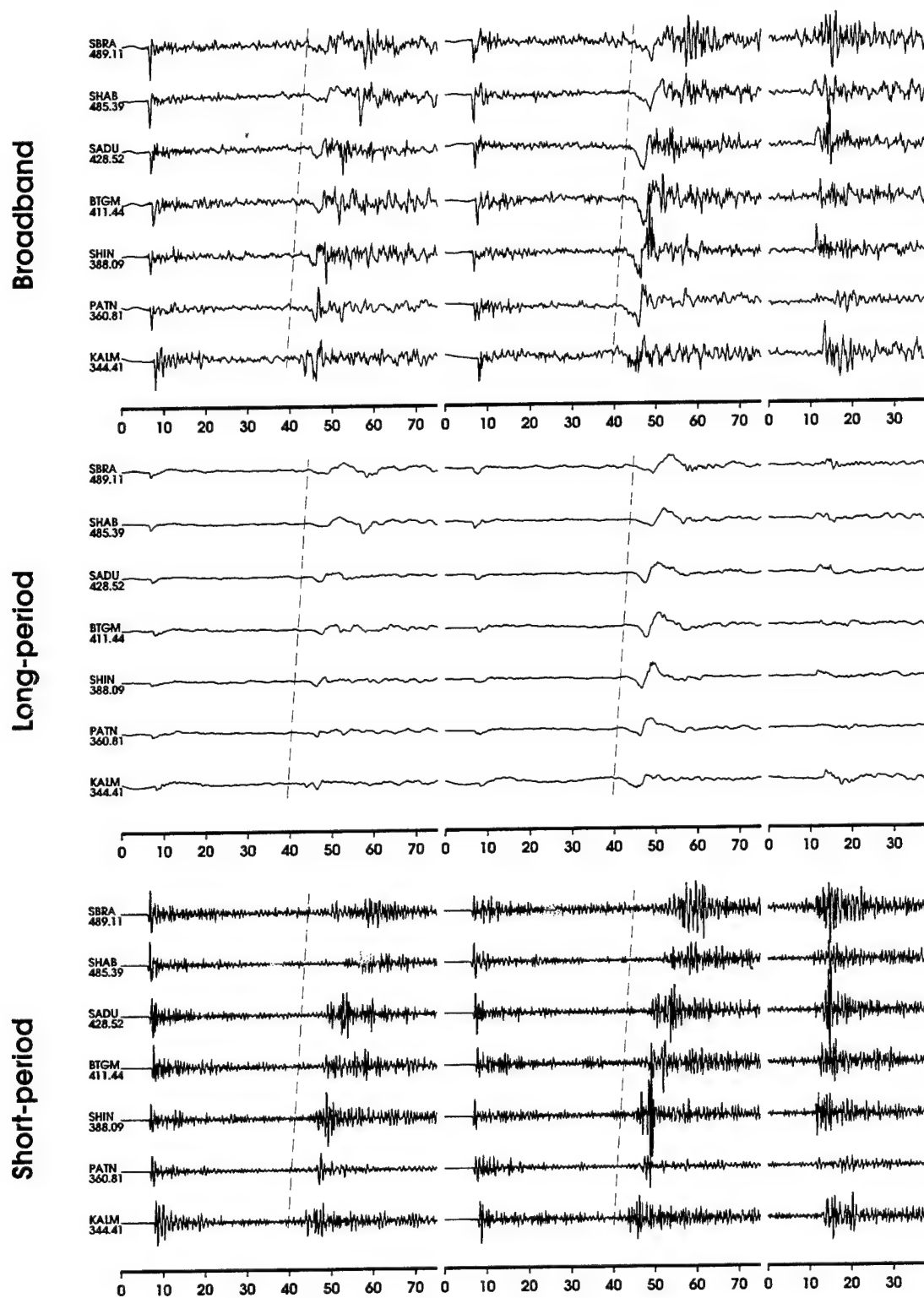
Figure 22 Presentation of PAKN observations for event 289.11942
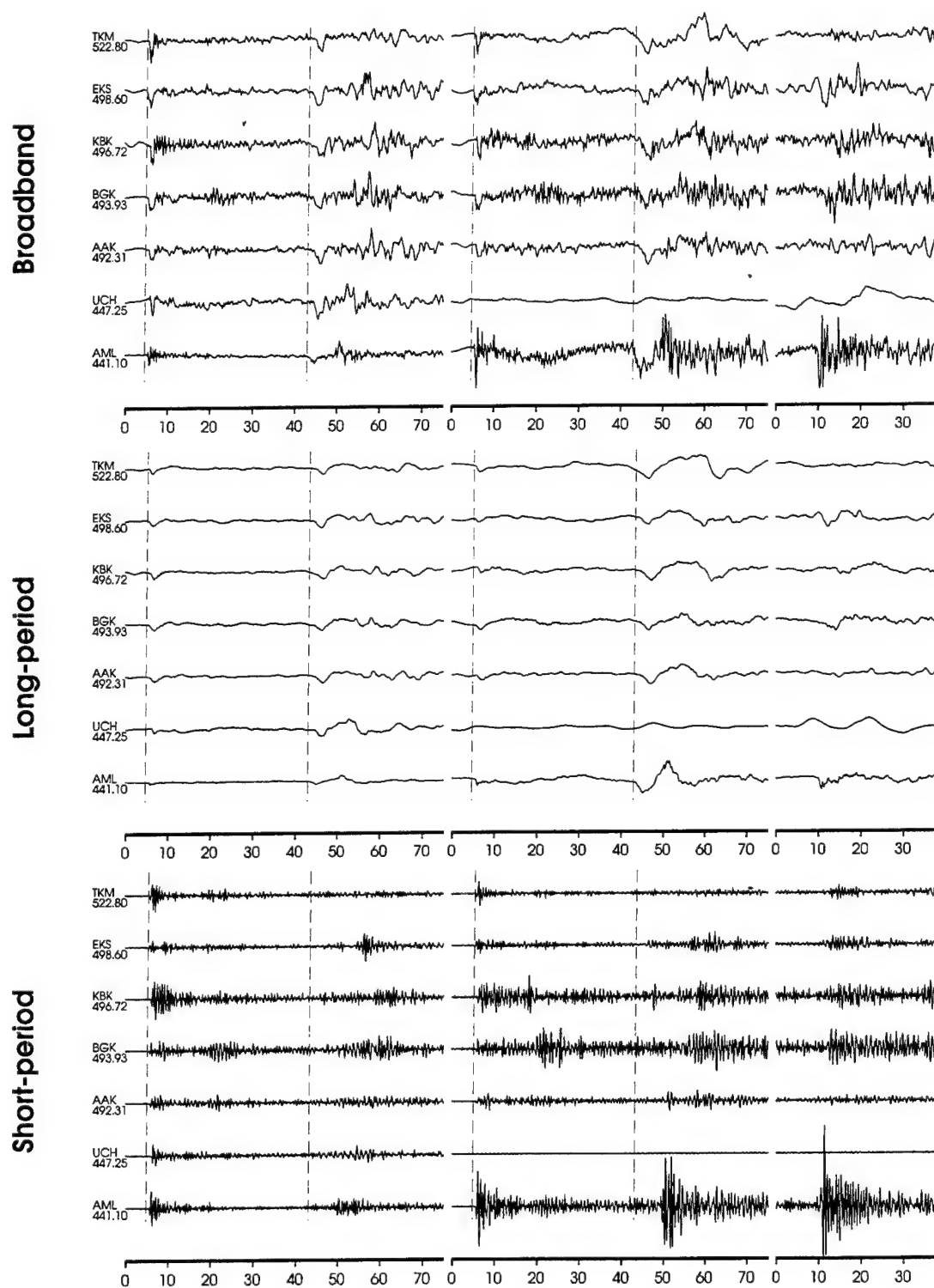
Figure 23 Presentation of KNET observations for event 289.1942.
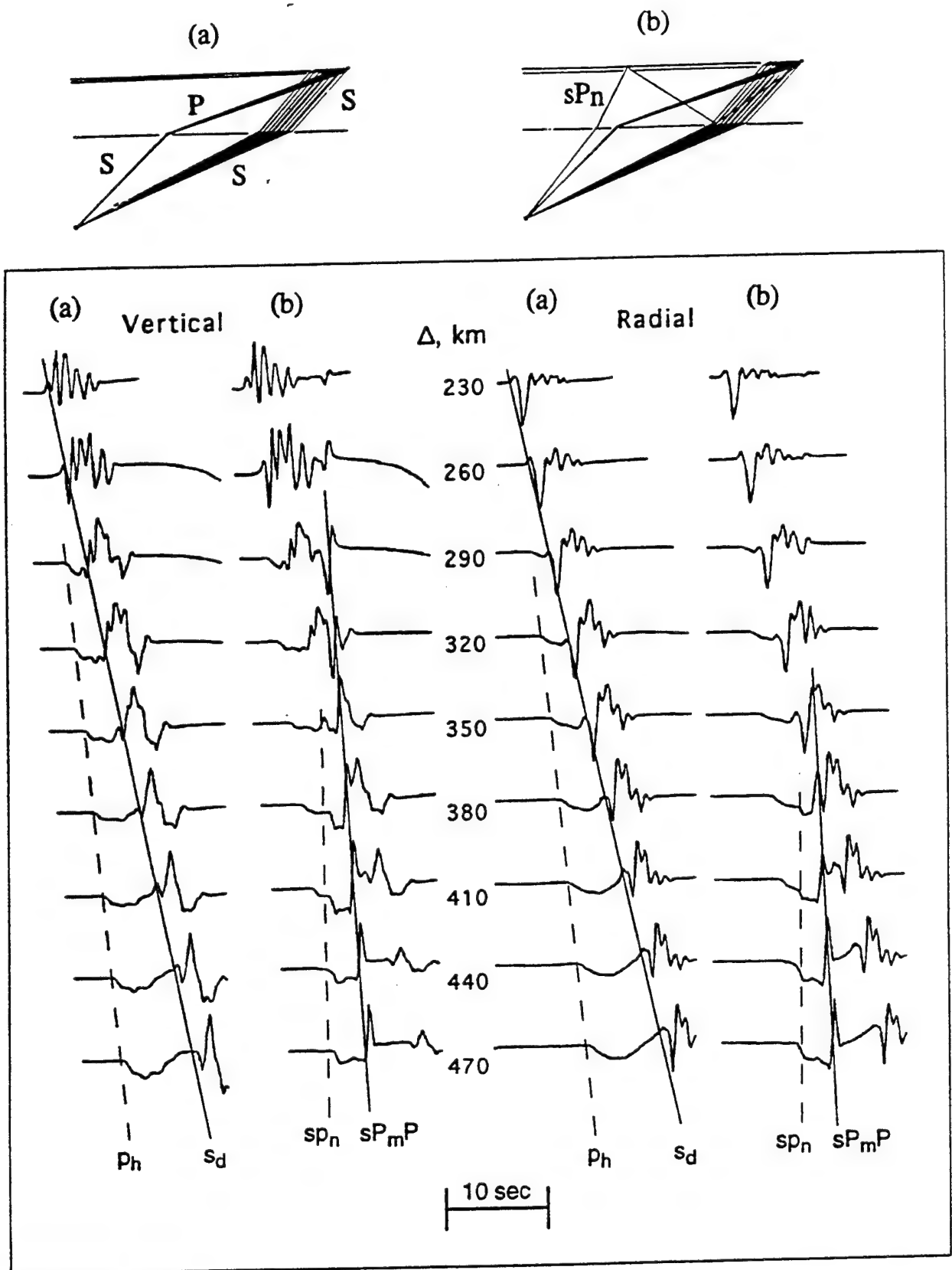
Figure 24 GRT synthetics constructed from two ray sets (a) and (b) as displayed in the top panel. The first column of each set contains only the P_{nl} contributions from the top-layer with P_h indicating the P-wave head wave along the bottom surface layer. The second column contains both sets of rays sampling the surface P_{nl} and the sP_mP rays. The sP_mP ray reaches critical angle near (300 km) with sP_n and sP_mP easily recognized at larger ranges. The Tibet model (Table 1) was assumed in this numerical experiment.

34

has both a headwave contribution, sP_n and a moho reflection contribution, sP_mP, as labelled in Figure 24. The headwave becomes visible at about 350 km and dominates the long-period motions beyond about 400 km. The reflected phase sP_mP from the bottom of the surface layer is very small in this case and has been neglected. Internal reflections at the surface SV to P mode-change-point become important when the layer becomes weak ($\beta < 2$ km/sec) and will be discussed later. The two lines P_n (local PL) and sP_n form the envelope expected for any crustal P-wave generated from S-to-P conversion at the surface. Most recordings at the Pakistan array appear to be dominated by the moho arrivals and any particular profile can be modeled quite well by adjusting the surface layer. Figure 25 displays the broadband reflectivity synthetics and observations (276.1438 event) for the Tibet model. The fit is not very good at broadband periods but proves satisfactory at long periods. Figure 26 displays the results for a similar model but with a faster surface layer, see Table 4. The faster surface layer spreads out the local PL waves and allows the moho headwave to become more visible near cross-over (~360 km). It also tends to reduce the strength of direct S_d on the radial component because of the increased angle of emergence. Note the difference in direct SV at the furthest station, SBRA, for the two contrasting models. The moho response consisting of P_n and sP_mP also is changed by the addition of the crust-mantle transition zone. The moho converted phases prove to be the most influenced by adding the transition as is evident in the two sets of synthetics. Note that the S to P converted phase which is quite evident at the start of the synthetics for the Tibet model, Figure 25, are nearly eliminated in Figure 26.

At long periods the Tibet model produced quite good fits to this particular profile, see Figure 17. Thus, adjustments of the type displayed in Table 4 are not going to change our source estimates but refining the model to study smaller events and associated shorter periods will be strongly affected. This remains a serious problem. Part of the problem can be addressed with respect to the receiver. Certainly, the variability in long-period to short-period signals from station to station displayed in Figures 21 through 23 suggests strong differences at each station and that these local site effects probably leave their own imprint upon the waveforms.

Correcting and dealing with short-period array data has been very well developed and will not be discussed here except for some broadband receiver function analyses. After examining

35
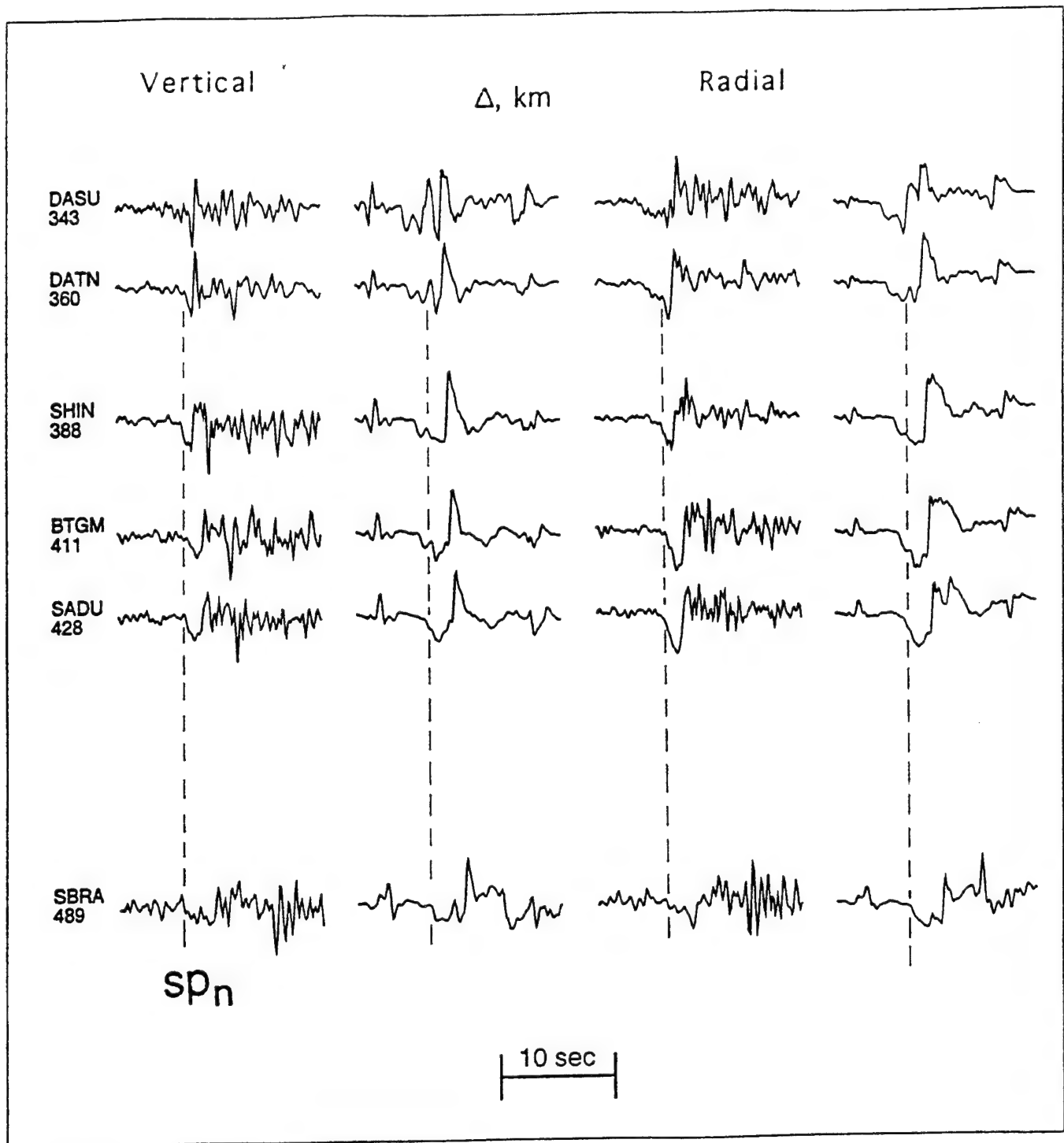
Figure 25 Comparison of broadband synthetics (reflectivity) from the Tibetan model vs. the 289.1942 observations. The vertical components are shown in the first two columns (data are plotted in the first column and synthetics are plotted in the second column). The radial components are similarly plotted in the third and fourth columns respectively. The dotted line is for the sP_n phase which leaves the source as a S and propagates as a P head wave along the bottom of the surface layer.

36
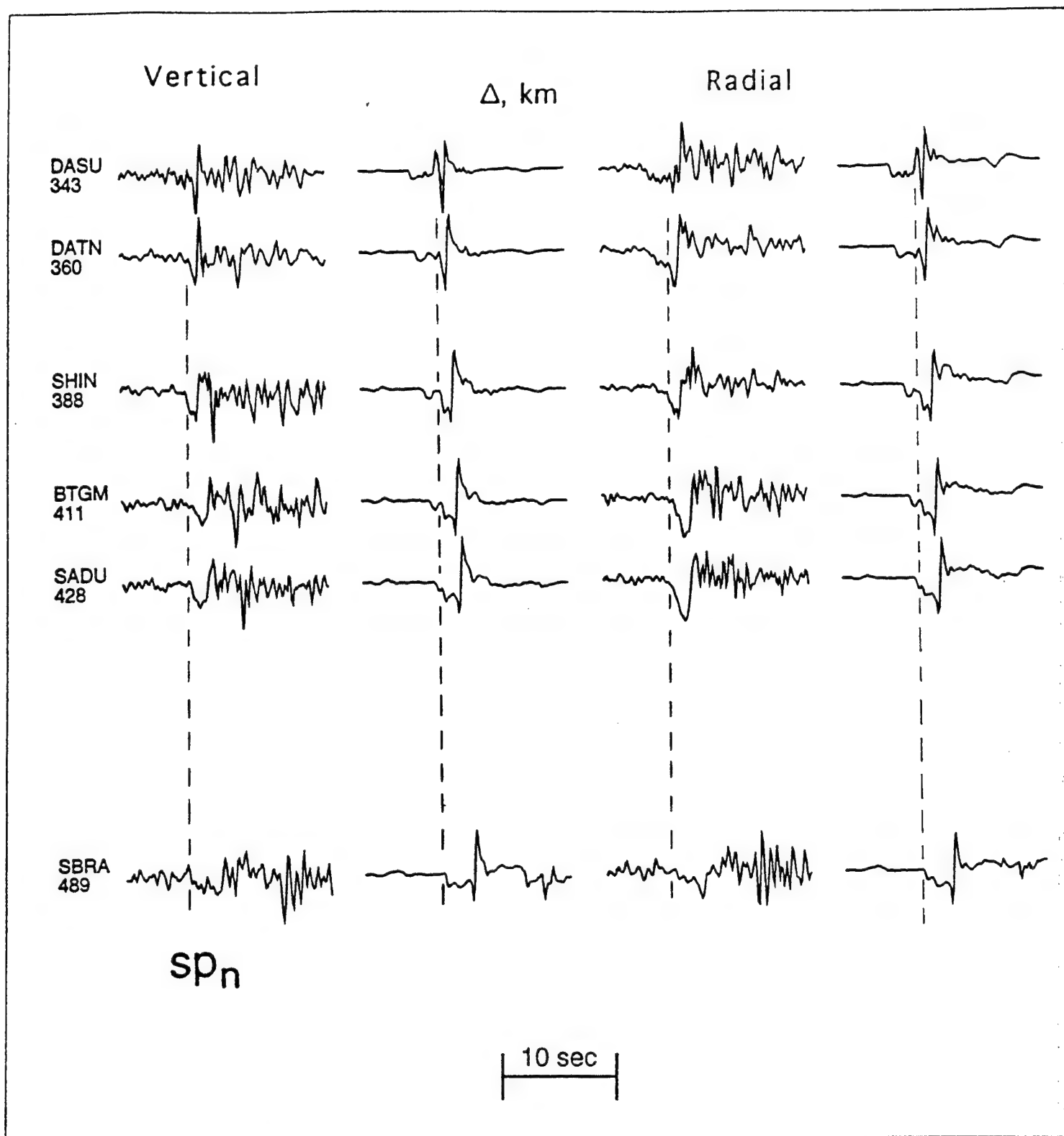
Figure 26 Comparison of broadband synthetics (reflectivity) with a similar model (see Table 4) where the top surface layer becomes faster and thicker. The vertical components are shown in the first two columns (data are plotted in the first column and synthetics are plotted in the second column). The radial components are similarly plotted in the third and fourth columns respectively. The dotted line is for the sP_n phase which leaves the source as a S and propagates as a P head wave along the bottom of the surface layer.

37

Table 4: Modified Tibetan Model

layer	Th (km)	$V_p(km/s)$	$V_s(km/s)$
1	7	5.5	3.0
2	60	6.2	3.5
3	2	6.6	3.7
4	2	7.0	4.0
5	2	7.4	4.2
6	2	7.9	4.5
7	200	8.27	4.7

Table 5: Receiver Models

	V_{S1}	V_{S2}	V_{S3}	V_{S4} (km/sec)
BTGM	3	3	3	3
DATN	2	2	2	3
KALM	2.6	3	3	3
SADU	2.1	2.3	2.3	2.3
SBRA	2	2.3	2.5	3.0
SHAB	2.2	2.3	2.3	2.3
SHIN	2.8	3.0	3.0	3.0

Table 6: Relocation Results Using PAKN and KNET

Event	Δt_0	Lat.	Long.	Δx	Az.	h	ISC h	h (km)
276	0	38	73	2	0	150	139	160
289	1	39	72	32	25	20	16	20
289	-0	38	74	5	321	160	157	180
311	-1	41	72	9	225	15	21	10
311	-2	34	69	23	161	20	25	30
317	-0	36	70	11	350	190	204	180
322	-4	33	67	8	320	10	35	10
328	-3	38	72	6	345	15	43	10
339	0	37	72	6	0	110	114	120
341	-0	37	72	4	0	110	122	120

38

the vertical and radial P-wave components of deep events such as those displayed in the above figures, we performed a standard deconvolution and modeling study of the first 10 secs of these records after stacking over the' events (Zhu *et al.*, 1995). Detailed velocity estimates of the top four kilometers with one km thicknesses were obtained as expressed in Table 5.

A comparison of synthetics and observations for the 276.1438 event is displayed in Figure 27 assuming the SBRA 'surface structure and the standard Tibet model for the deeper crust structure. Note that the hardest sites are in the mountains while the softest sites are situated along the river, see Figure 20. The start of the P-wavetrain on the two components is good for SBRA but this structure does not seem to help explain the direct SV phase. Moreover, the hardest site according to Table 5 is BTGM which is not in agreement with the SV-signals. The stations with the smallest ratio of short-period to long-period amplitude are station SADU and DATN which again are not supported by the results from Table 5. This lack of agreement between P and S waves is probably caused by the extreme sensitivity of the SV-wave to lateral variation since the locally generated P-waves are at or near critical angle. It is probably not practical to determine such detail for all the individual stations discussed above especially for those sites no longer occupied. However, the broadband PAKR station and the AAK site will be investigated in more detail as data become available.

The broadband nature of sP_n and sP_mP is probably more important than the direct S-wave for source estimation since it seemingly is more long period and stable. But, it too suffers from the S-to-P interaction at the bounce point. This feature is explored in Figure 28 where we have simulated the response of sP_n for various surface conditions and added it to S-PL structure of a different model essentially using two different models for the ray-sets discussed earlier in Figure 24. The S-PL structures, a set of rays, are those discussed earlier in Figures 25 and 26. The three columns of synthetics on each side of the data contain these PL-waves plus a hard interaction (assuming the same properties as the lower crust, $\alpha = 6.2$, $\beta = 3.5$), and a soft layer interaction ($\alpha = 3.5$ km/sec, $\beta = 2$, h = 2 km). A hard bounce-point produces the strongest conversion as well as keeping the response broadband. It is difficult to argue for such an idealized situation. A soft-point bounce is probably more realistic based on assumed geology and yields a more complex signal caused by the internal multiples produced from the layer

39
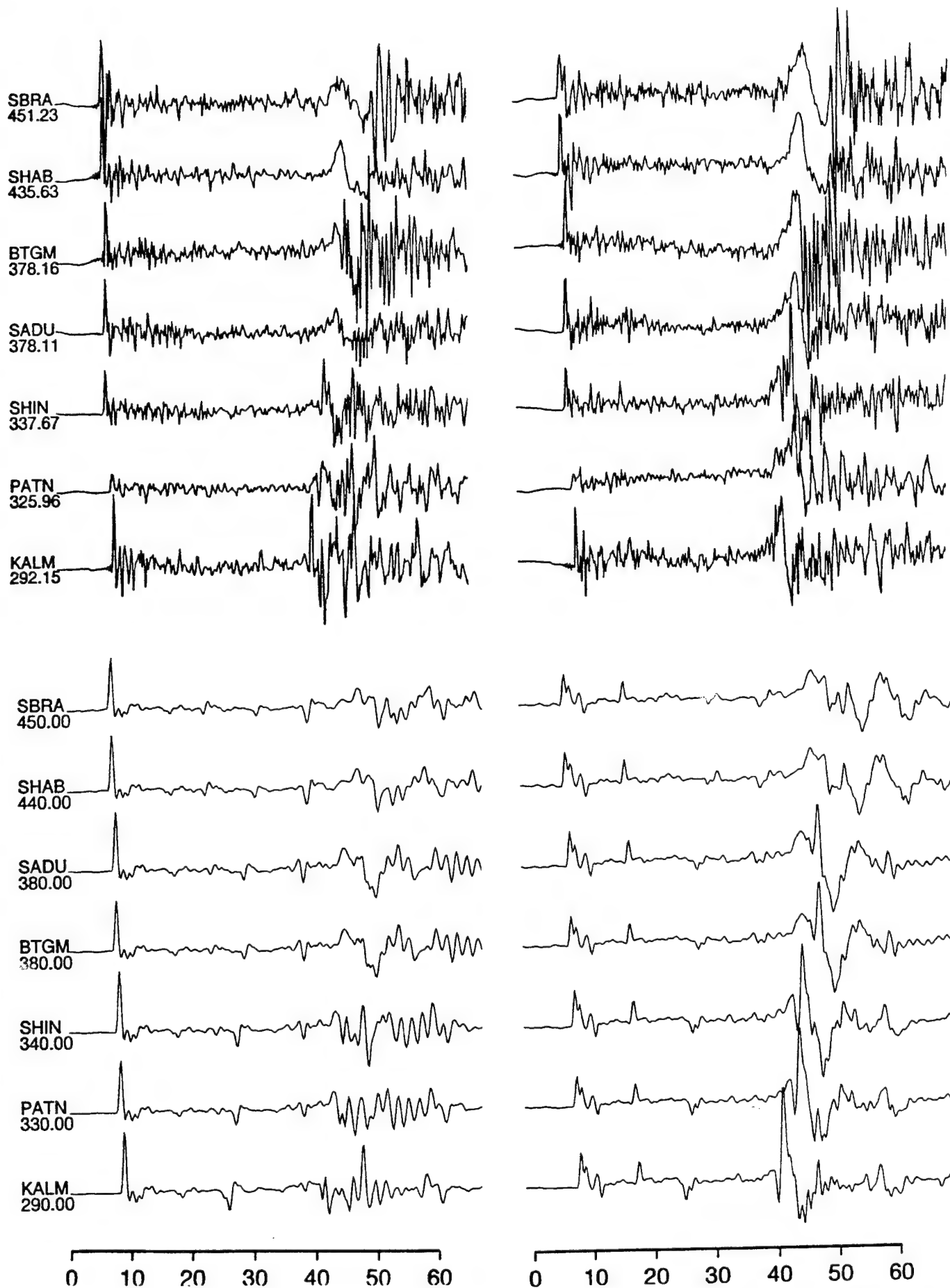
Figure 27 Comparison of broadband observations with a synthetic record section generated from a model derived by inverting the P-wave forms for SBRA.

40
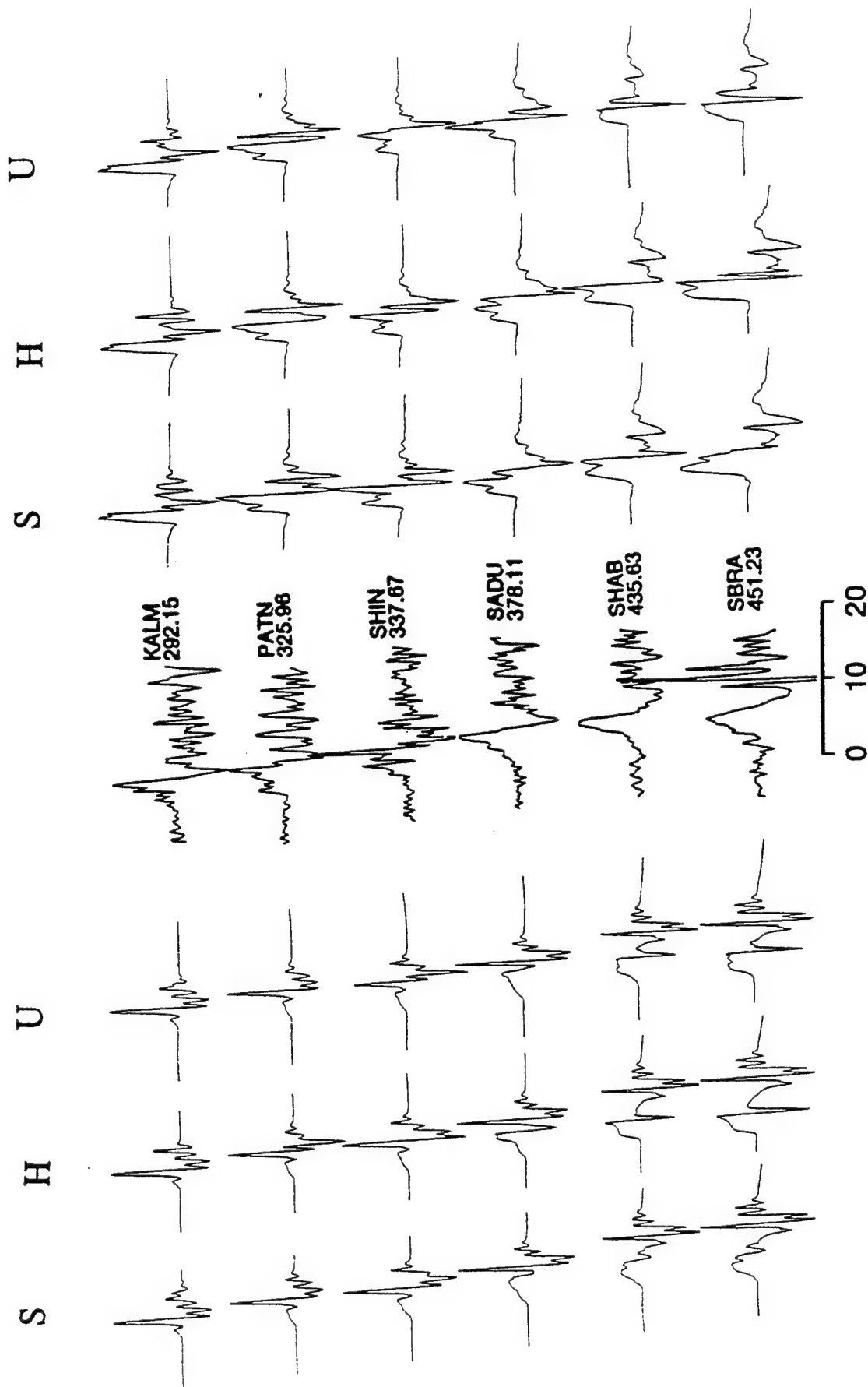
Figure 28 Comparison of hybrid GRT synthetics assuming the P_{nl}'s for the surface layer given in the Tibet model (on the left) and the faster model, Table 4, (on the right). Columns marked (U) also contain the sP_mP appropriate to that model. Columns marked H (hard bounce) do not have a soft layer at the surface and those marked S (soft bounce) assume a top layer with $\alpha = 3.5$, $\beta = 2$, $h = 2$ km. The middle row is for data.

interaction. The relative strengths of sP to direct SV varies with range caused by the above interference. Note that the nearest stations, KALM, PATN, SHIN and SADU favor the models on the right while the two stations at the edges of the basin SHAB and SBRA favor the softer surface conditions on the left. Synthetics generated in this fashion for other deep events produced similar results. Adding the flexibility of a separate structure for the bounce-point obviously makes modeling of these records much easier and provides one explanation for why the broadband characteristics of the individual records in Figures 21 - 23 are so different.

The KNET data for deep events are similar to that observed at PAKN except for sP_n, see Figure 23. While sP_n begins slowly at the largest ranges, see SBRA and SHAB in Figures 21 and 22, they tend to be much more impulsive at similar distances in Figure 23. Sharp crust-to-mantle transitions with uniform mantle velocities produce the shapes matching the PAKN observations as discussed above. To match the KNET data requires a more gradual crust-mantle transition zone along with a mantle gradient. A model that appears quite good is given in Figure 29 and was found by extensive forward modeling attempts. Synthetics for this model are compared with both sets of array data in Figure 30 for the 289.1942 event. Results for the 276.1438 event are about the same. While the shortest periods do not fit well from record to record, the overall fits are quite good with respect to KNET (upper panel). The fits to the nearest distance recordings in PAKN (lower panel) are not so good. For example, the synthetics display two strong peaks at DASU, KALM, and PATN with only the KALM data indicating such features. The first peak is an sP phase from a layer as displayed in Figure 29. Its absence in most PAKN records suggest this boundary is not there. Thus, this model is a compromise fitting many features from the two networks but fitting neither particularly well. Nevertheless, it is quite useful to have a 1-D model for locating as discussed later and for investigating shorter period motions when the PKAR short period array becomes operational.

3.2 Event Depth Estimation

Although we have discussed in detail why the phases sP_n, sP_mP, direct SV, and associated PL waves show considerable scatter, we do not mean to suggest that this combined wavetrain is not useful. In particular, at long periods the phase sP_n is quite detectable and its phase velocity is nearly the same as direct P, see Figure 23.
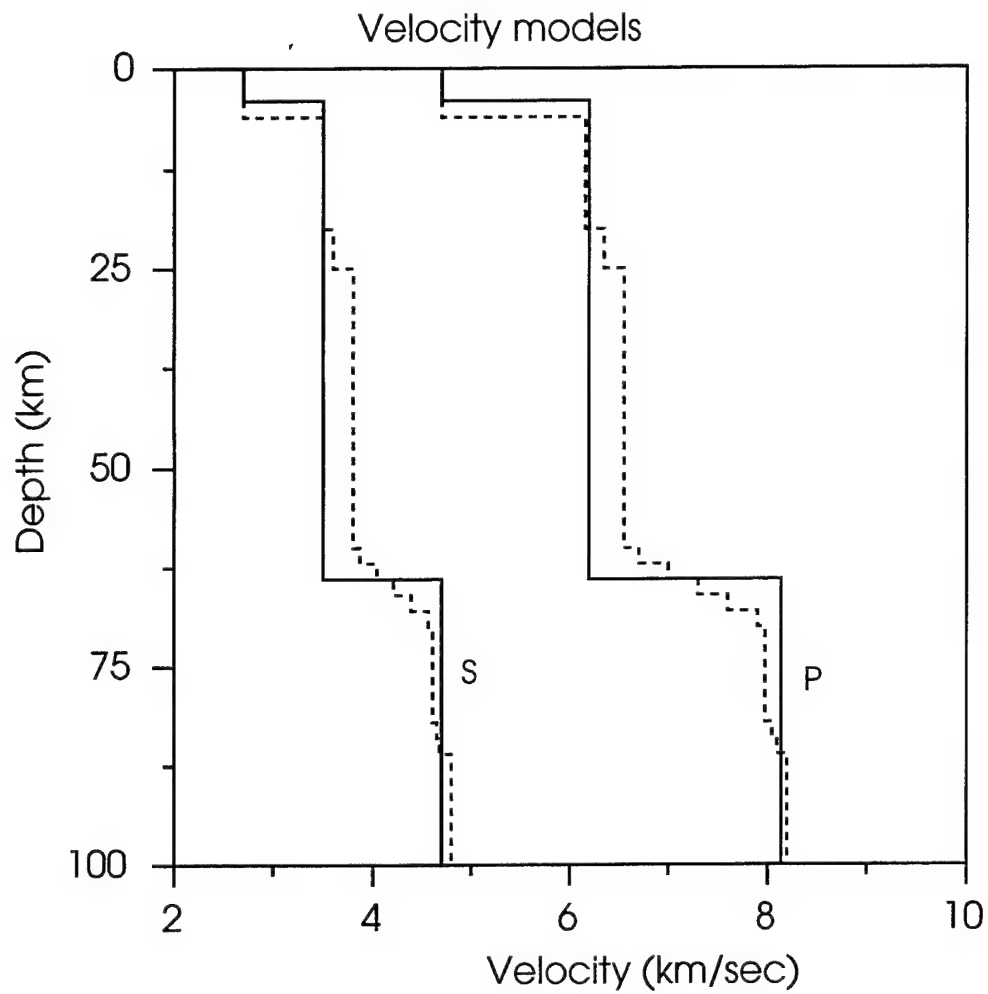
Figure 29 Comparison of the two-layered Tibetan model (solid line) with a 12 layered model (dashed line) that fits the KNET data better.
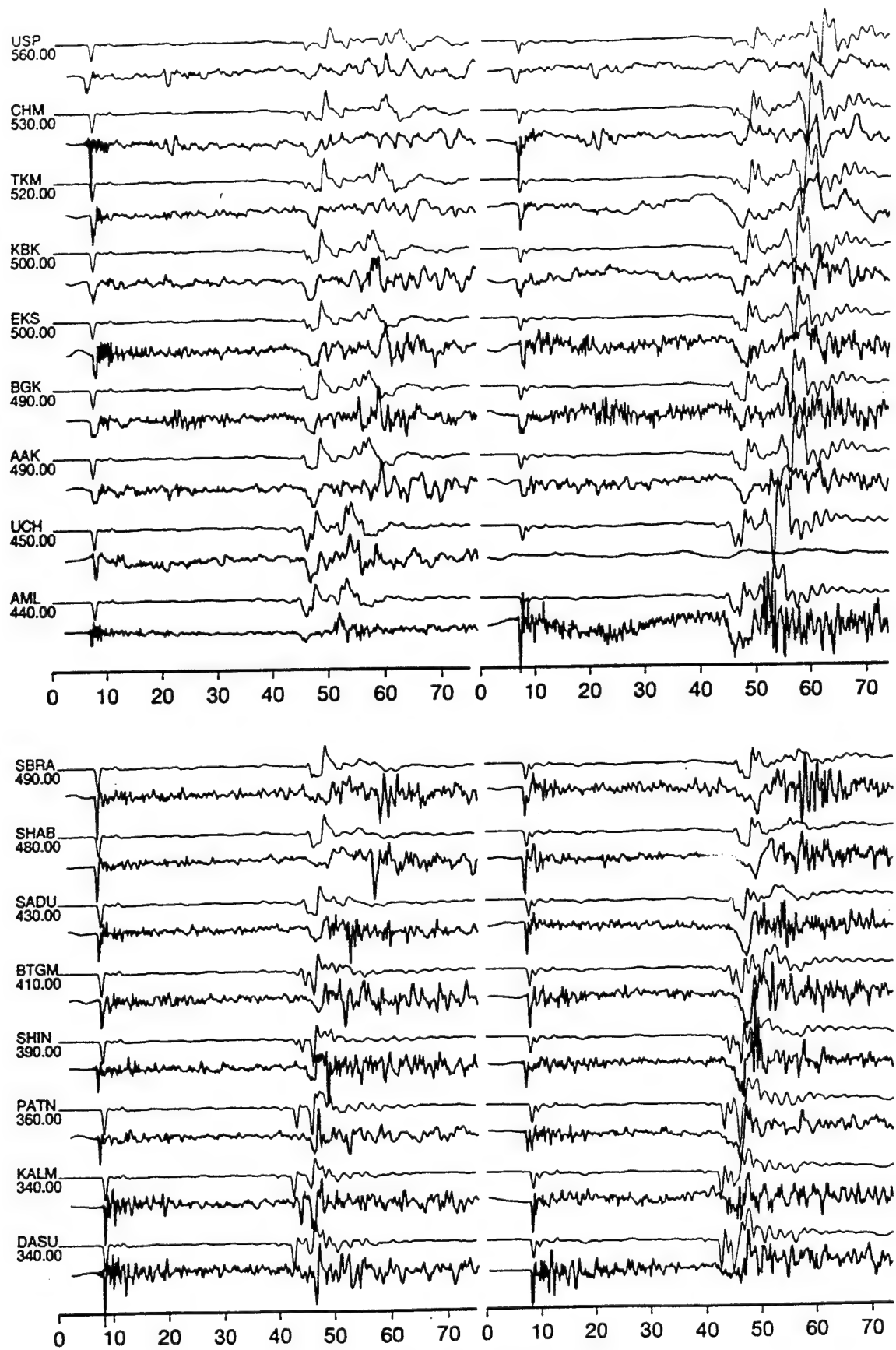
43

Figure 30 Comparison of broadband synthetics with observations (289.1942) for the arrays assuming the 12 layered model. For each station, the upper seismograms are the synthetic seismograms.

44

The offset, δt, between these arrivals is a direct measure of source depth. Estimates of δt for the Tibetan model can be obtained directly from the Green's function discussed earlier in Figure 6. A source depth of 80 km predicts a δt of about 25 secs while a 200 km depth yields about 40 secs. These estimates are model dependent as discussed above but appear quite useful in establishing stable depth estimates. One could simply measure the δt directly from the data, as in Figure 23, and use a look-up table generated from synthetics. Another method more amenable to automation is to obtain this measure by matching synthetics directly against the observations. However, as discussed earlier we have separated the P-wavetrain from the extended SV-wavetrain following our source estimation procedure. This desensitizes the direct depth estimate in an attempt to maximize the influence of the source mechanism. However, with the source fixed we can re-run the correlations of synthetics with observations as a function of depth but allowing only whole record shifts. The results are given in Table 6. The shallow events are not influenced much by this condition since the misfit error is controlled by the amplitude of the surface waves. The best comparison is in the time domain as displayed in Figure 31 where the separation between P and the converted S to P and SV in the synthetics compares well with the data, especially in the PAKN observations.

Included in Table 6 are some location estimates based on P-wave picks obtained from the two arrays. With the depth fixed, we form a square grid around the ISC location and compute travel times residuals until the best location is obtained. The distance, Δx, is expressed in km at the appropriate azimuth. A correction in origin time is expressed as Δt_O. Events tend to move northward but agree with the ISC locations quite well except for the two small, shallow events, 289.0242 and 311.1758. A possible explanation is discussed later in Section 5 where we address a much larger data set.

4. E_{sp-Pz}:E_{lp-3} Discriminant

In conjunction with calibrating propagation paths in this region, we are assisting in the integration and testing of the short-period:long-period energy (E_{sp-Pz}/E_{lp-3}) regional seismic discriminant into the IDC (International Data Center) monitoring system software. This work has involved several tasks including putting the discriminant algorithm into a form suitable for the DFX system and helping the IDC staff to implement it into their operational test-bed system.

Event 276.1438 model t92_150 strike 325 dip 70 rake -30 moment 4.4 error 7.09e-04 shift0 -999

Figure 31 Comparison of broadband synthetics with observations for the 276.1438 event assuming the Tibetan model where no shifts were allowed between the P and the S-wave. For each station, the bottom seismograms are the synthetic seismograms.

46

Another task has been to test and refine the $E_{sp-Pz}:E_{lp-3}$ discriminant on data throughout the current study area, in particular broadband records from stations near or at sites of current and future GSETT-3 stations and arrays in the Hindu-Kush region. Data examined so far is for regions covered by the KNET and PAKN arrays. Figure 32 is a map of this region with plots of the stations and events used.

The $E_{sp-Pz}:E_{lp-3}$ discriminant, which is the ratio of integrated energy between the short-period vertical component P-wave (E_{sp-Pz}) and the sum of the three long-period surface wave trains (E_{lp-3}), is calculated using the formulae:

$$E_{sp-Pz} = \int_{t_1}^{t_2} v_{sp-z}^2(t)dt \quad and \quad E_{lp-3} = \sum_{i=1}^{3} \int_{t_3}^{t_4} v_{lp}^2(t)dt, \tag{3}$$

where v is the ground velocity, and t_1 and t_2 are the window times of the P-wave train and are typically set slightly higher than the P_n and S_n velocities, respectively, and t_3 and t_4 are the window times for the surface wave trains and are set by the fastest and slowest surface wave group velocities of interest, respectively. The time windows are determined from velocity or slowness curves determined for a particular region. This discriminant was developed from observations of TERRAscope data for NTS explosions and earthquakes throughout the region and is a regional analog to the $m_b:M_s$ discriminant, see Woods and Helmberger (1996).

4.1 Software Development and Discriminant Operational Capability and Refinement

The $E_{sp-Pz}:E_{lp-3}$ algorithm was put into a subroutine form compatible with the DFX system. In conducting this task we have interacted with David Jepsen at the Center for Monitoring research (CMR), who is implementing the algorithm into the IDC automated (intelligent) monitoring system. This collaboration also involved evaluating the practical limits of the discriminant.

For an operational monitoring environment, it is necessary to delineate what data can be analyzed/processed using this discriminant. As this algorithm requires both short-period and long-period data, a broadband station is necessary. One of the strengths of this discriminant is
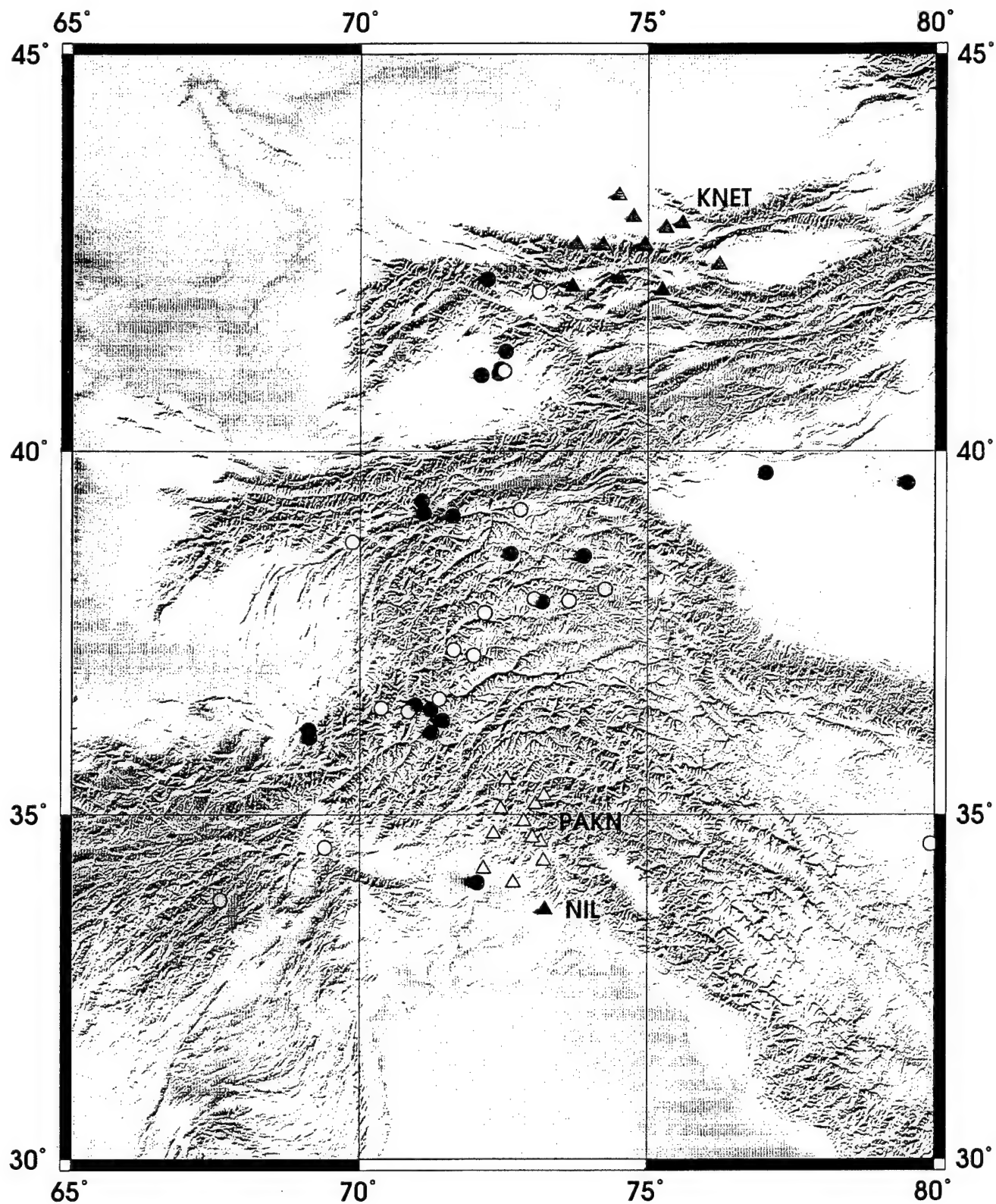
Figure 32 Map of the Hindu-Kush region with the stations (triangles) and events (circles) used in the short-period:long-period energy discriminant calibration/performance study. Events recorded by a particular array or station are color-coded with the corresponding station symbols. Earthquakes in pink were recorded by both the KNET and PAKN arrays.

48

that it relies on both Rayleigh and Love wave energy levels, however this does require a three component station to retrieve the energy of the entire wave field. Thus, should the vertical component be missing, the remaining time series cannot be used. Should one of the horizontal components be missing it may still be possible to obtain information concerning the event. For an earthquake generating large surface waves the observed energy ratio utilizing only two long-period records may still constrain the event to be an earthquake. However, on average the energy ratio will be 1.5 times larger than for a three-component measurement, as the long-period energy sum, the denominator in the ratio, will only be about two-thirds of its three-component sum.

Another operational problem is data outages, for which it is necessary to estimate the percent of the specified time windows required to have some confidence of the measurement. The answer to this question depends in large part on the stringency of the time windows used. Figure 33 is a typical regional (R=864 km) vertical component broadband velocity record for a crustal earthquake, along with short-period and long-period play-outs of the record and their associated long-period and short-period energy curves. Note in the energy curves the ramp-like (at short-period) and step-like (long-period) increases at the arrival of the main energy phase.

In the case of the P-wave this energy is either the P_n or P_g phase early in the P_{nl} wavetrain. Assuming that the time window is defined by the arrival times corresponding to the P_n (t_1) and S_n (t_2) arrivals, we suggest that at least the first 50% of the initial Pnl time window is necessary for the short-period energy integration. For the long-period energy, the most important part of the record is centered about the Airy phase, so this portion of the record is crucial for accurate long-period energy measurements. Hence, assuming a narrow time window between the fastest and slowest group velocity arrivals of interest, we estimate that 70% of the time window, centered about the Airy phase arrival, is necessary for accurate long-period energy measurements.

Related to the question of what portion of the time window is necessary for accurate integrated energy measurements is the development of a weighting scheme for the data by tapering the signal within the time windows. In particular, one would want something akin to a negative slope ramp function on the P-wave window, with the initial portion of the record
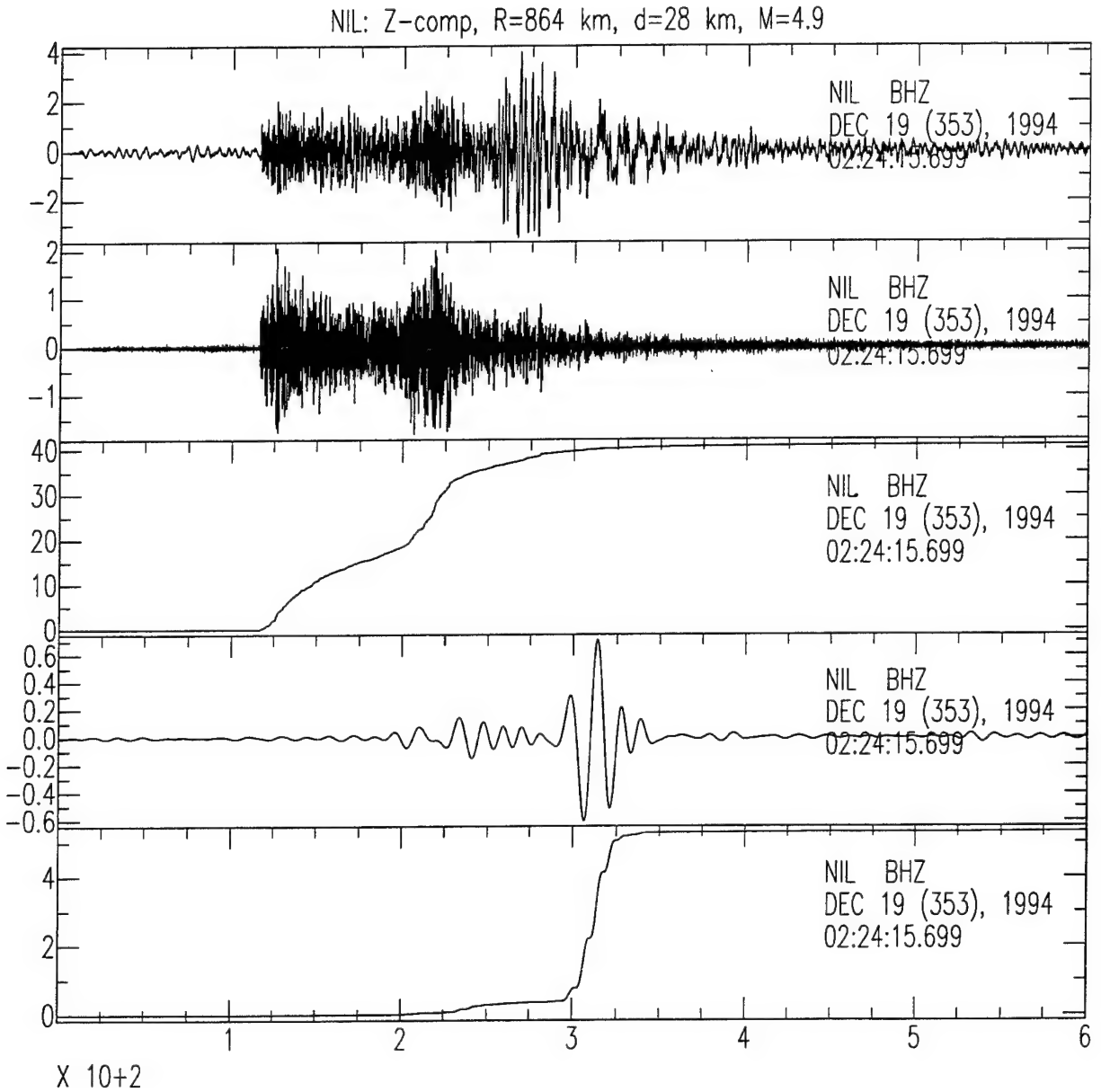
49

Figure 33   Example of a vertical component velocity record from NIL used in the short-period:long-period energy discriminant. The top trace is the broadband record. The second trace is the high-pass (f ≥ 1 Hz) play-out with its attendant energy curve under it. The fourth and fifth traces are the long-period (0.033 ≤ f ≤ 0.125Hz) playout and energy curve respectively.

50

weighted most heavily, and for the surface wave a trapezoidal or triangular weighting scheme centered about the Airy phase. For the P-wave such a weighting scheme would make the initial prominent arrivals the largest factor in the integrated energy term and mitigate the effects of later scattered and diffracted arrivals.

Such a weighting/windowing scheme would require a very accurate arrival time of the P-wave, otherwise the most strongly weighted portion of the time window could be before the primary arrival. One could also not begin tapering the data until later into the record, thus making it more effective at emphasizing the primary arrivals. The surface wave weighting scheme on the other hand is more forgiving assuming a fairly good estimate of the Airy phase arrival and can be used particularly effectively with large latitude (wide) time windows. From broadband waveform modeling, it has been found that the surface wave arrivals move around with respect to the more stable body wave phase arrivals (Helmberger and Song, 1995), contributing to the effectiveness of waveform source inversions using one of the "cut and paste" methods (Zhao and Helmberger, 1994; and Zhu and Helmberger, 1995). Thus, fairly general calibrated regional Greens functions or travel time curves can be used for determining the energy integration time windows.

Another problem is what to do with transient signals which are at or near the noise level in one pertinent frequency band or the other. Related to this issue is the effect of the length of the time window. For good signal to noise ratio (SNR) events in a particular bandwidth, the length of the time window is unimportant because the primary rise of the energy curve is the ramp or step function of the arrival of interest, see Figure 33, whereas for a poor SNR time series the entire energy curve may be a near constant slope ramp which may or may not have a slight step or temporarily steeper slope at the arrival of the phase or wavetrain of interest. Using as narrow a time window as possible to minimize such effects for the smaller (M > 4) events is important for obtaining accurate energy ratio estimates.

Another way to mitigate such low SNR effects is to remove the effects of ambient noise by taking a portion of the energy outside the arrival window of the transient signal, E_s, normalizing

this sum to the length of the time window of interest (E_N) and obtaining a modified integrated energy for the signal, E'_S; based on the apparent energy measurement, E_M:

$$E_S' \cong E_M \times \frac{E_M}{(E_M + E_N)}, \tag{4}$$

where $E_M = E_S + E_N$. This can be rearranged to yield:

$$\cong E_S + \frac{E_N^2}{E_S + 2E_N} . \tag{5}$$

For the case $E_S \gg E_N$, $E_S' \cong E_S$. For the case $E_S = E_N$,

$$E_S' = \frac{4}{3} E_S . \tag{6}$$

In the next section, which compares the performance of the discriminant on data from the study region with that in other tectonic provinces of the world, other refinements or ideas for improvement which came about through the processing and analysis of this data will be discussed. Such features and modifications have not yet been incorporated into the "alpha-version" of the subroutine delivered to IDC, but can easily be implemented, if desired.

4.2 Performance and Calibration of the Discriminant

The data sets compiled for the path calibrations of the Hindu-Kush region (the KNET and PAKN arrays and NIL) were also used to test the performance of the $E_{sp-Pz}:E_{lp-3}$ discriminant. These events and stations are shown in Figure 32. Table 7 lists the stations and their coordinates and Table 8 is an event catalog listing for this study. The fact that no explosion data are available for these regions makes it that much more important to compare the available results for earthquakes with combined population data sets for other regions. As was shown in Figure 2b, the behavior of the crustal earthquakes is similar to that of TERRAscope data, whereas the deeper, mantle events generally have higher integrated energy ratios that place them in the

52

Table 7: Stations used in the Energy Discriminant Study

Station	Lat.	Long.
NIL	33.650	73.251
MNSR	34.34	73.21
KALM	35.49	72.57
PATN	35.14	73.07
DASU	35.26	73.22
SADU	34.73	72.34
BTGM	34.67	73.02
SBRA	34.03	72.68
SHAB	34.23	72.17
SHIN	35.08	72.47
AAK	42.633	74.944
UCH	42.227	74.513
USP	43.267	74.500
ULHL	42.40	76.24
EKS2	42.662	73.777
AML	42.131	73.694
KZA	42.079	75.25
TKM	42.86	75.318
TKM2	42.92	75.60
KBK	42.656	74.947
BGK2	42.645	74.227
CHM	42.998	74.751

Table 8: Events used in the Energy Discriminant Study

Jul. date	h:m:s:	Mag.	Latitude	Longitude	ISC Depth	Recorded by
92136	8:8:2.9	6.2	41.019	72.429	50.0	KNET
92276	14:38:44.3	4.9	38.006	73.044	118.0	PAKN,KNET
92289	2:42:6.3	4.6	39.212	72.798	16.0	PAKN,KNET
92289	19:42:11.8	4.6	38.134	74.265	135.0	PAKN,KNET
92292	16:14:45.5	5.1	42.066	73.116	19.0	PAKN
92301	2:54:35.0	4.5	37.977	73.643	167.0	PAKN
92307	4:52:52.9	4.8	37.228	71.990	128.0	PAKN
92310	9:21:56.5	4.4	36.494	70.374	200.0	PAKN
92311	7:21:57.8	5.1	41.051	72.518	40.0	PAKN,KNET
92311	11:47:42.9	4.6	34.584	79.921	12.0	PAKN
92311	17:58:38.0	4.5	34.532	69.394	33.0	PAKN
92313	20:50:3.0	5.3	38.778	69.864	64.0	PAKN
92317	20:41:4.6	5.7	36.446	70.852	198.0	PAKN
92322	2:38:50.1	5.3	33.782	67.574	36.0	PAKN,KNET
92328	23:11:6.7	5.6	38.620	72.635	41.0	PAKN,KNET
92330	4:46:8.1	4.5	37.303	71.641	196.0	PAKN
92331	22:57:13.5	4.1	36.620	71.388	189.0	PAKN
92339	11:36:36.2	5.9	37.814	72.194	120.0	PAKN
92341	3:44:29.9	5.5	37.810	72.186	128.0	PAKN
92359	5:9:47.4	5.2	42.221	72.225	38.0	KNET
93364	14:24:4.5	5.7	44.735	78.793	15.0	KNET
94012	10:22:51.3	5.3	39.247	75.493	28.0	KNET
94121	21:17:20.7	5.2	39.126	71.621	33.0	KNET
94353	2:24:15.7	4.9	39.574	79.516	28.0	NIL
94353	3:22:17.8	4.1	34.032	72.060	33.0	NIL
94358	23:51:47.9	5.3	38.588	73.897	33.0	NIL
94360	14:48:1.4	5.3	36.469	71.244	226.0	NIL
94360	20:34:25.6	4.5	36.535	70.969	195.0	NIL
94363	16:1:18.2	5.5	35.655	80.663	33.0	NIL
95026	7:0:45.0	5.2	36.147	71.255	106.0	NIL
95026	11:36:51.8	4.2	39.711	77.051	33.0	NIL
95030	3:6:56.7	4.1	29.286	82.217	52.0	NIL
95030	22:36:31.5	4.9	36.315	71.446	77.0	NIL
95030	13:56:46.9	4.0	28.349	82.457	81.0	NIL
95041	7:49:19.4	4.6	36.186	69.111	44.0	NIL
95041	8:17:48.5	4.6	36.082	69.122	33.0	NIL
95051	4:12:23.2	5.4	39.167	71.118	26.0	NIL,KNET
95051	8:7:34.2	5.0	41.073	72.451	39.0	NIL,KNET
95059	10:24:13.9	4.9	37.962	73.180	141.0	NIL
95281	8:55:49.9	5.9	40.989	72.118	48.0	KNET

explosion population region, the exception being records recorded at apparent P-wave nodes. This behavior is also borne out in the KNET data in Figure 34a. Woods and Saikia (1995) also found the discriminant to be effective at separating crustal earthquakes from explosions (from the Kazakh and Lop Nor test sites) in Central Asia in Figure 34b. Note that the Ural event, believed to be a mine collapse (Walter, personal communication), plots within the earthquake population.

Similar results were also found in this study for historical data for U.S. PNE's and nearby earthquakes. A notable exception to this is for events recorded by the Tibetan PASCAL array experiment (Owens, Randall, Wu and Zeng, 1993) for which the travel paths traverse a region of known high shear-wave attenuation or S-wave blockage (McNamara, Owens and Walter, 1995; and Zhu and Helmberger, 1995) particularly at short-periods. Here, the short-period:long-period ratios are significantly reduced for earthquakes and the one available explosion. We speculate that P-wave propagation effects are similar to those of the S-waves, so the short-period P-wave amplitudes are diminished, too, with respect to the surface waves, thus lowering the $E_{sp\text{-}Pz}$:$E_{lp\text{-}3}$ ratio. Thus, when incorporating this discriminant into new monitoring regions it is important to determine regions of regional phase blockage.

Part of improving the performance of the discriminant involves arriving at optimal bandwidths for measuring the short-period and long-period energy levels. Woods and Saikia (1995) found that the short-period measurement is best made for velocity records high-pass filtered at 1 Hz, and the optimal long-period bandwidth is between 0.033 Hz and 0.125 Hz. Results in this study use these bandwidths.

Another refinement that came about through the analysis of the data and comparisons to other data sets was that the best separation of events is obtained if the energy ratio (E_R) is normalized by the magnitude of the event, i.e.:

$$E_R' = E_R \times 10^{(M-M_0)},$$

(7)

where M is the magnitude (m_b or M_L), and M_0 is a standard magnitude which we chose to be M = 5, so that the normalized ratio scale will be compatible with that of the raw ratio. Such a
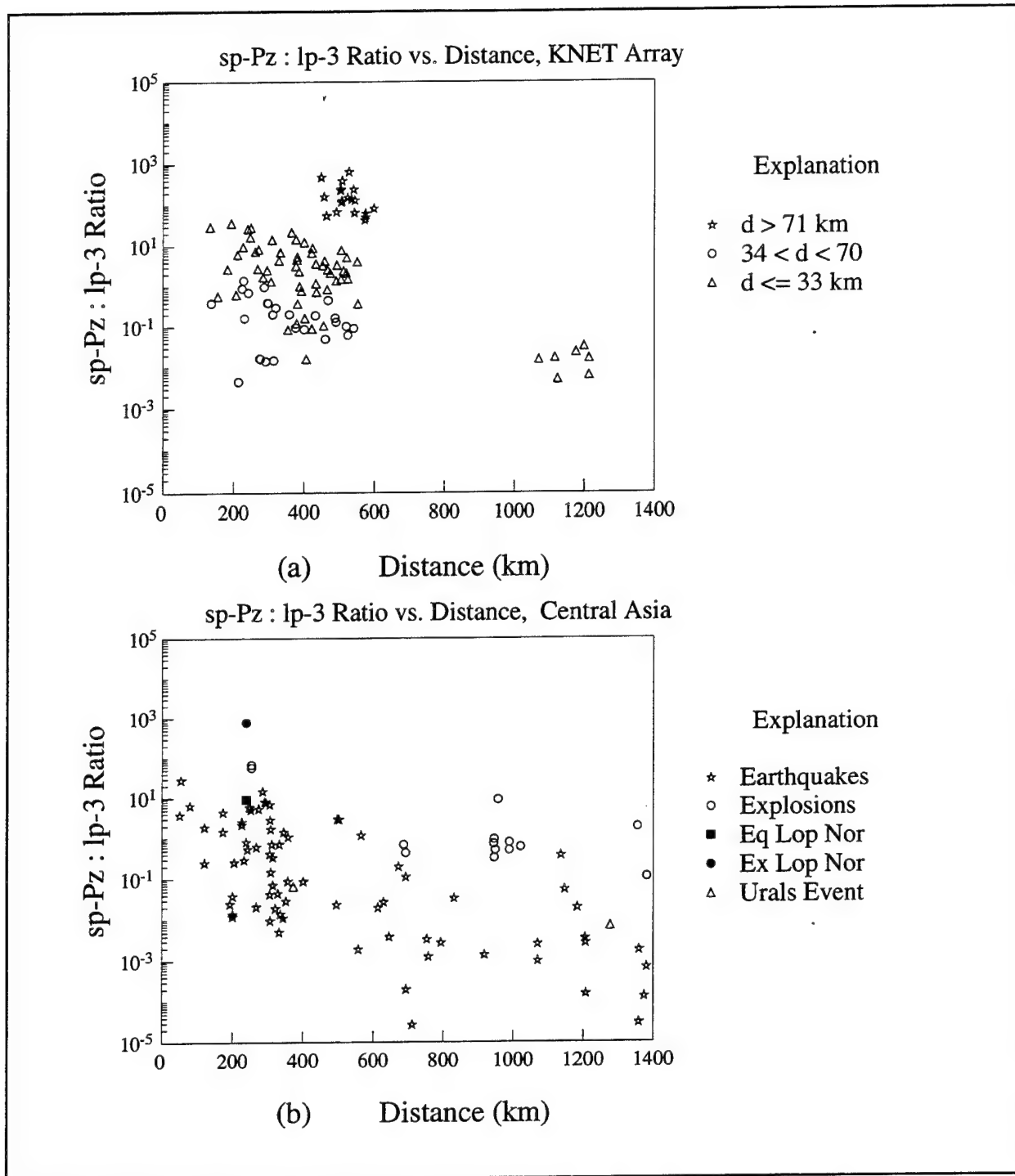
Figure 34. (a) Short-period:long-period energy ratio vs. distance for KNET data. Stars represent deep (mantle) earthquakes, triangles denote intermediate depth events, and circles represent events occurring at less than 33 km depth. (b) Short-period:long-period energy ratio vs. distance for central Asian data. Stars represent earthquakes, circles denote explosions with the filled circle being a Lop Nor test, triangles represent data points of the Ural mine collapse. The one earthquake located nearby the Lop Nor test site is a filled square.

normalization or sorting of empirical discrimination parameters by magnitude is used for other regional discriminants as well (Taylor *et al.*, 1989; and Walter *et al.*, 1995).

The result of applying this correction to the TERRAscope data, where this refinement was first tested, is shown in Figure 35. Comparison of this plot to Figure 2a clearly shows improvement in the separation of the earthquake and explosion populations at the nearer distances. There are two explanations for why this improves the separation. The first is that by multiplying the energy ratio by the short-period magnitude, one is in effect multiplying the short-period integrated energy sum by another measure of the short-period source spectrum, thus enhancing the difference in the short-period:long-period ratio. The other explanation is that the short-period and long-period source spectra scale differently and that what is being done is to normalize the long-period energy level with respect to magnitude. It may be more justifiable to correct with respect to the long-period magnitude, preferably M_w. As there is some correspondence between m_b and M_w, either should give rise to the same type of correction. Also not all events currently have available M_w's. Determining regional M_w estimates is, however, a product of the source inversion scheme discussed in Section 2 of this report.

For the KNET data set the magnitude correction plot shown in Figure 36a does not have an appreciable effect on the relative positions of the deep and shallow/intermediate depth earthquake populations. This observation can be explained by the fact that the two deep events both had magnitudes less than 5, while all but two of the crustal earthquakes were larger than 5. Thus, before the magnitude correction, none of the deep events were large enough magnitude to be "pulled down" into the crustal earthquake population because of their relatively large long-period source levels.

What is apparent from the plot is that the deep earthquakes behave as explosions with respect to this discriminant in that they have high energy ratios relative to the shallower (crustal) earthquakes. This is not surprising in that it is well known that deep earthquakes tend to generate little if any fundamental mode surface wave energy which is what is being measured. The $m_b:M_s$ discriminant has the same pitfall when performed without applying a magnitude depth correction (Marshall and Basham, 1972). The problem is that crustal and mantle earthquakes have

Figure 35. (a) Magnitude-normalized short-period:long-period energy ratio vs. distance for TERRAscope data. (b) Magnitude-normalized short-period:long-period energy ratio vs. distance for the Central Asian data set.
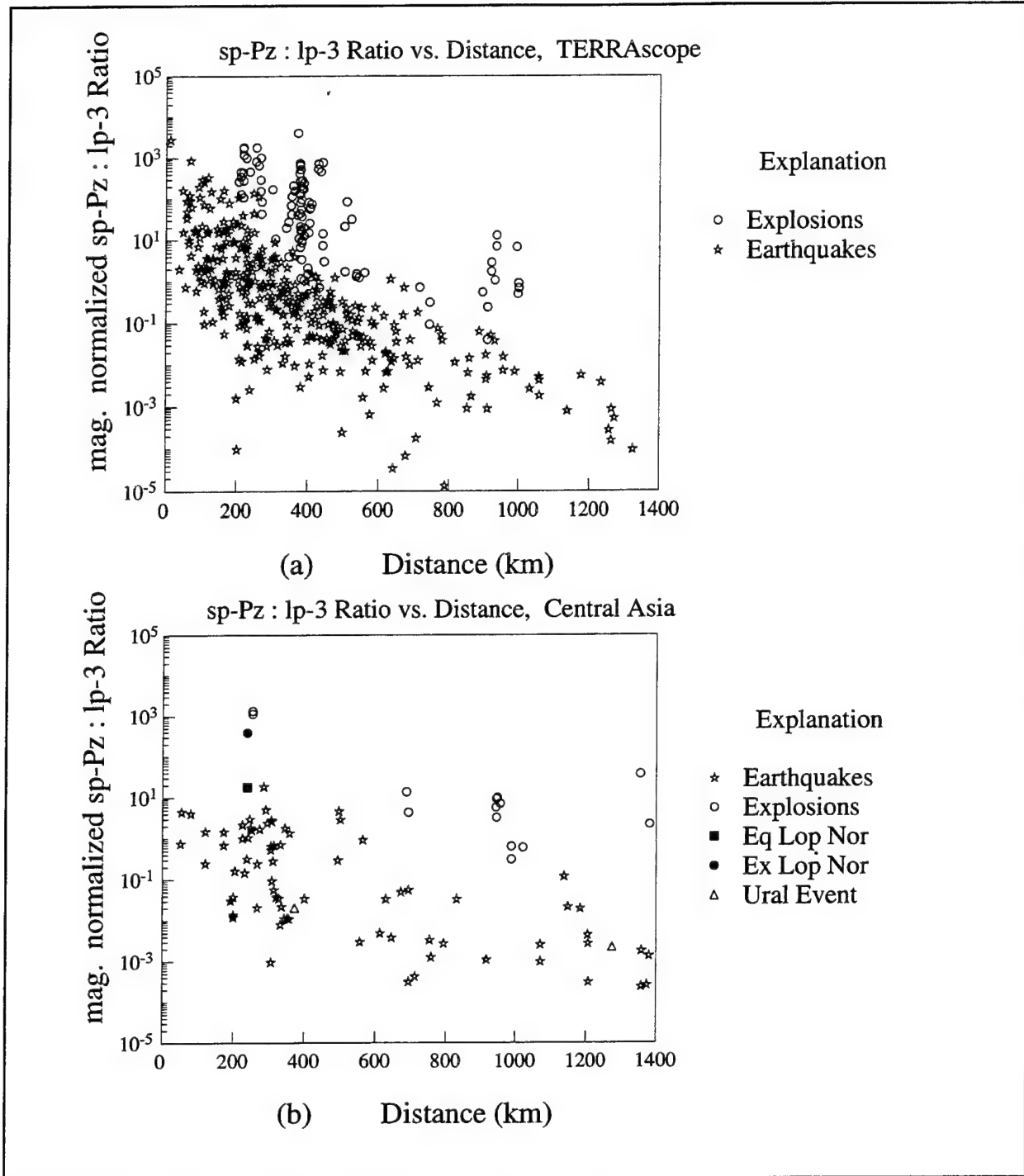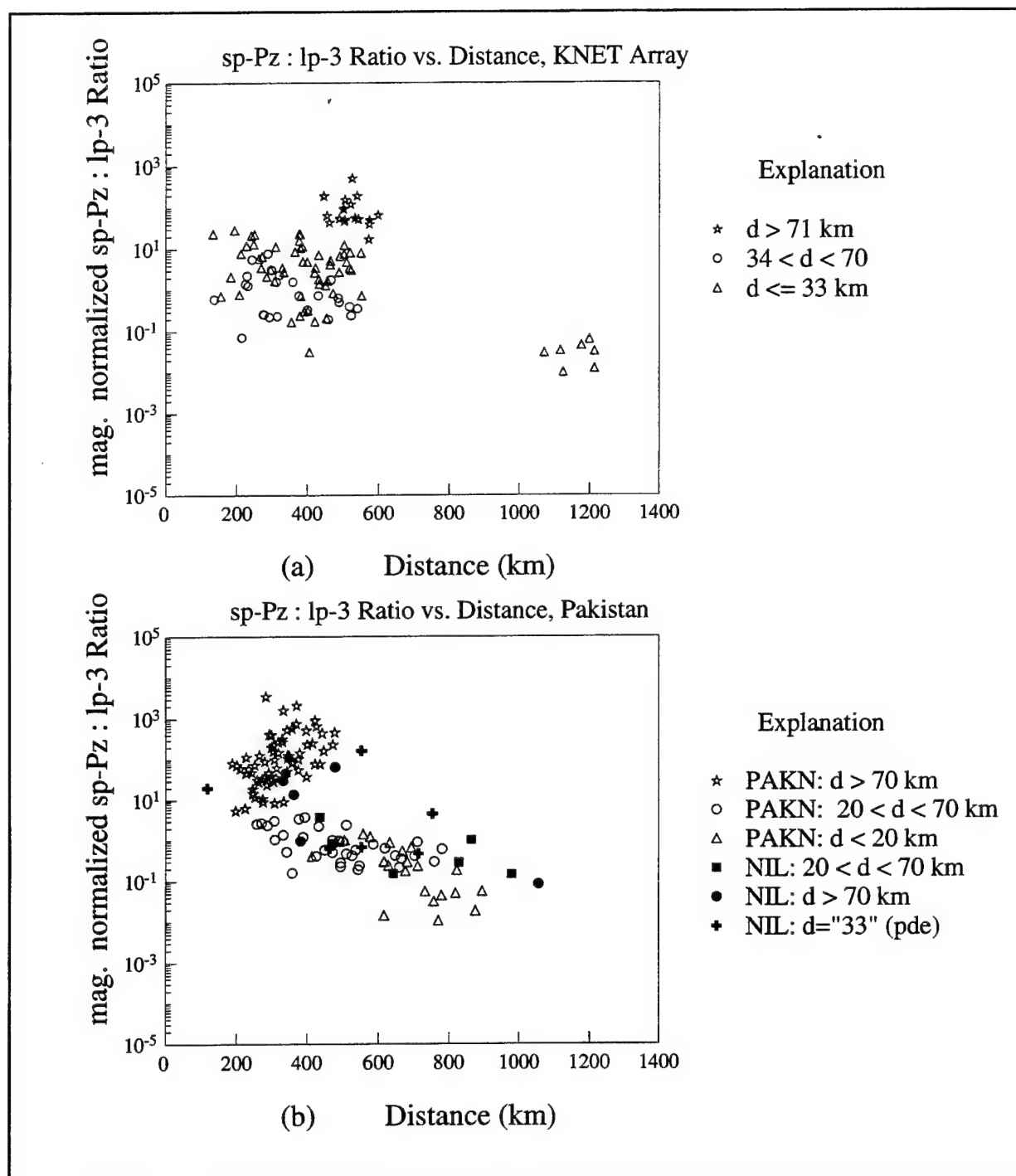
Figure 36. (a) Magnitude-normalized short-period:long-period energy ratio vs. distance for KNET data. (b) Magnitude-normalized short-period:long-period energy ratio vs. distance for the Pakistan data set.

significantly different signal spectra which gives rise to mantle earthquakes looking explosion-like by some criteria.

This difference in energy ratios due to waveform content is borne out in Figures 37 through 39, which show the vertical component records in different bandwidths with their attendant energy curve for a shallow (d = 26 km), intermediate (d = 77 km), and deep (d = 141 km) event, respectively. The top trace in each figure is the broadband velocity record under which is the high-pass (f ≥1Hz) velocity record and its energy curve, followed by the intermediate-period (0.033 < f < 0.125 Hz) velocity record and its energy curve. Note the large surface wave on the 4th trace centered at 220 sec and the corresponding step function in the energy curve.

For the intermediate depth earthquake in Figure 38 there is long-period energy coming in at around 75 sec which is presumed to be due to the long-period S-wave signature. Such energy needs to be windowed out of the later arriving surface wave in order to obtain accurate energy measurements. In Figure 39, a deep earthquake is an even more extreme case, in that by far the largest long-period phase in the record is that due to the S-wave arrival at 120 sec. The later arriving surface wave is much smaller in comparison and the corresponding energy curve also reflects the fact that most of the incoming long-period energy is due to the S-wave.

This is a consideration for time windowing deep events as they often have very strong, fairly long-period S-wave arrivals, as was discussed in Section 3. Should the surface wave time window be too wide, the S-wave (actually a combination of sP_n ... PL phases) energy can appear as surface wave energy. In such cases the event will have too large an apparent long-period integrated energy sum, thereby misplacing the deep event into the crustal earthquake class. This is not a problem for misidentifying explosions, but rather for the estimation of depth of earthquakes.

The magnitude correction does have a pronounced effect on the Pakistan data set plotted in Figure 36b as the deep events separate for the most part from the shallow and intermediate depth earthquakes in comparison to the uncorrected energy ratios in Figure 2b. There are two significant exceptions to this. One is a deep event (filled square) at about 380 km. This event

Figure 37 Vertical component velocity record for a shallow crustal earthquake recorded at NIL. The top trace is the broadband record. The second trace is the high-pass ($f \geq 1$ Hz) play-out with its attendant energy curve under it. The fourth and fifth traces are the long-period ($0.033 \leq f \leq 0.125$ Hz) play-out and energy curve, respectively.
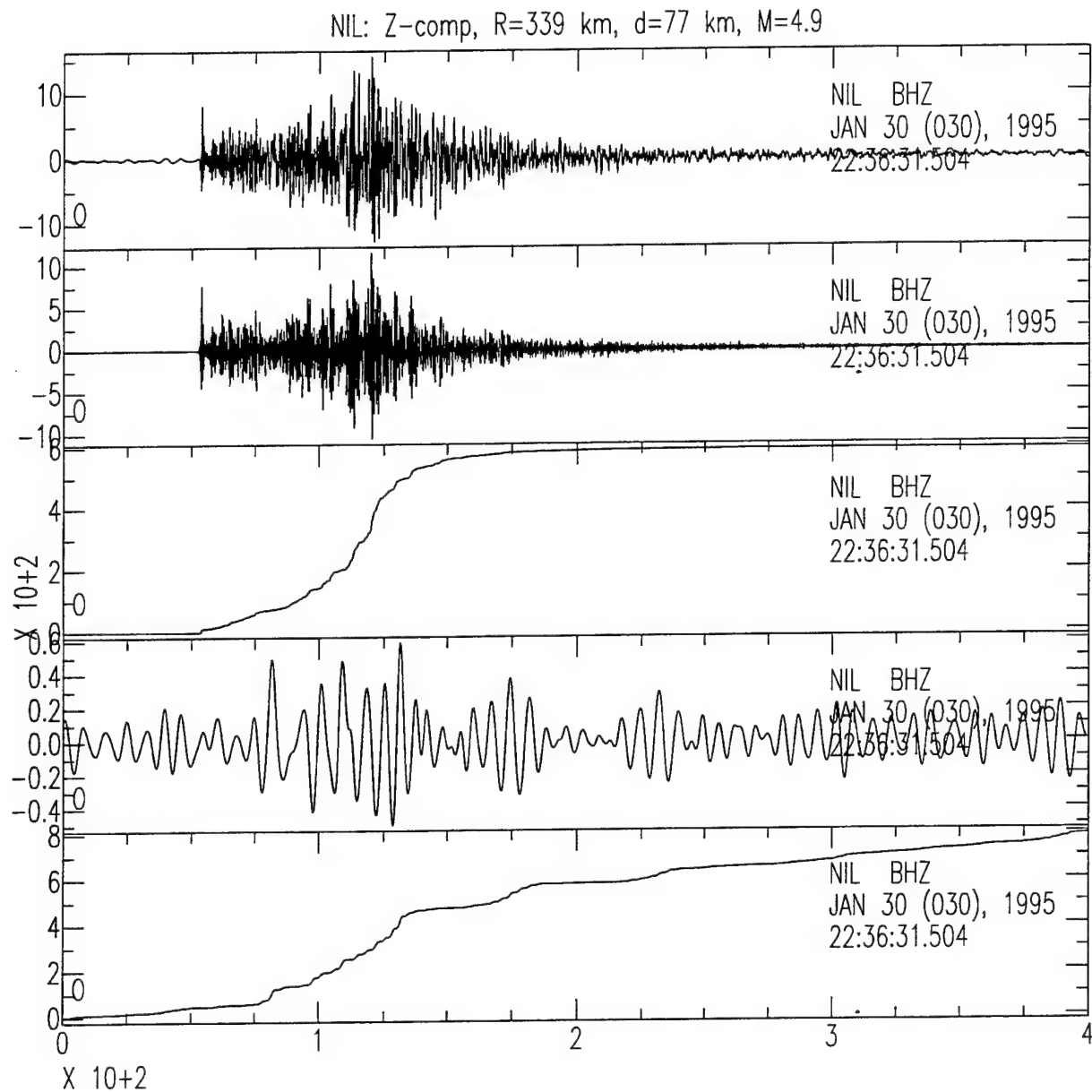
Figure 38 Vertical component velocity record for an intermediate depth earthquake
recorded at NIL. The top trace is the broadband record. The second trace is the high-pass (f
≥ 1 Hz) play-out with its attendant energy curve under it. The fourth and fifth traces are the
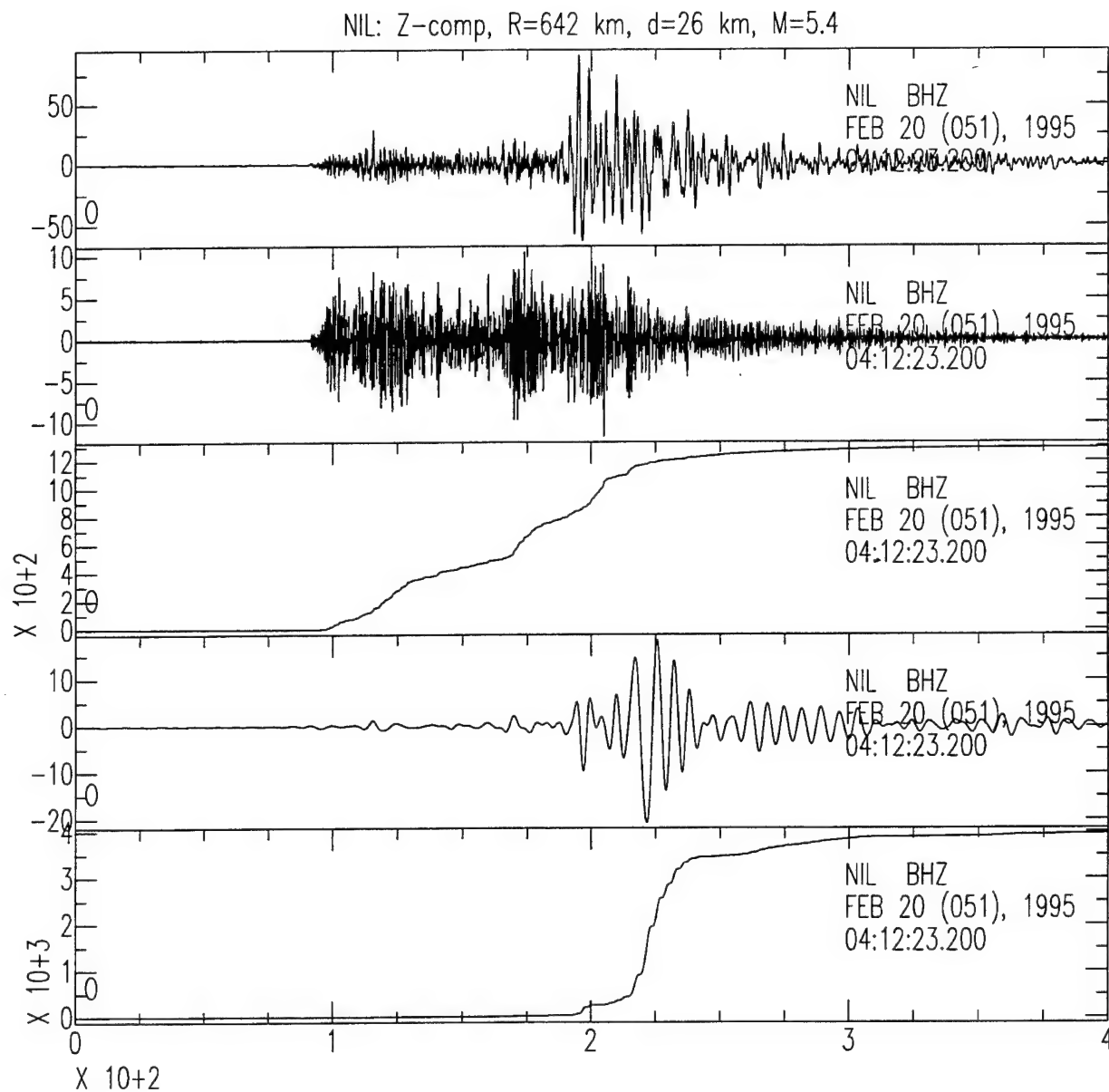long-period (0.033 ≤ f ≤ 0.125 Hz) play-out and energy curve, respectively.

Figure 39 Vertical component velocity record for a deep earthquake recorded at NIL. The top trace is the broadband record. The second trace is the high-pass (f ≥ 1 Hz) play-out with its attendant energy curve under it. The fourth and fifth traces are the long-period (0.033 ≤ f ≤ 0.125 Hz) play-out and energy curve, respectively.
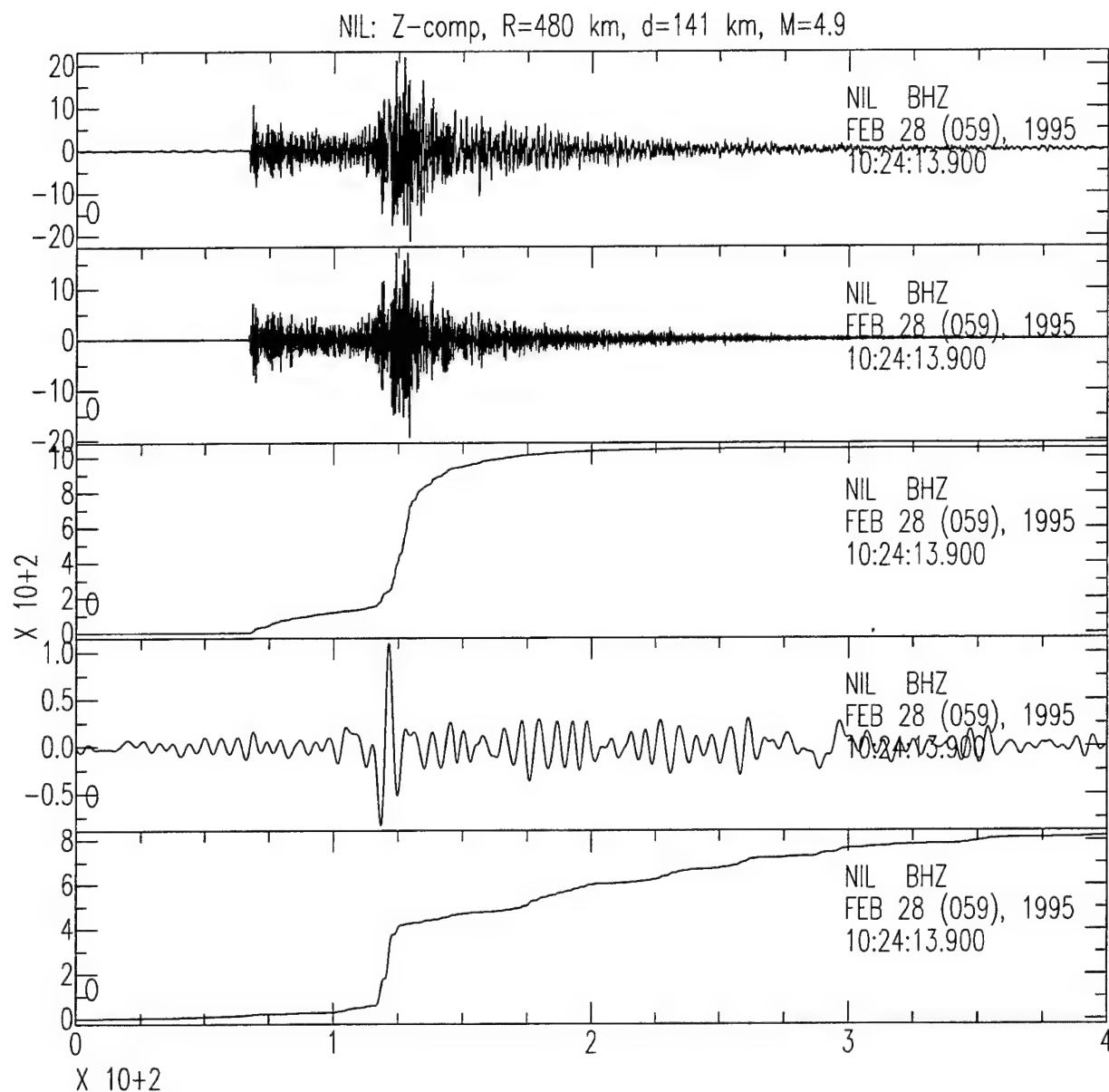
has a very small short-period P-wave arrival relative to the S-wave and is suspected to be an observation at a P-wave node. The other deep event, at a distance of 1060 km, is given a PDE depth of 81 km. This event has not yet been inverted for source depth and mechanism using our procedure, so our best depth estimate may well place this event somewhat shallower, making it a deep crustal earthquake and putting it into the other population.

As far as discrimination is concerned, classifying a deep earthquake as a crustal earthquake is no problem, as the event is then precluded from being an explosion. For the former case of a P-wave node, a secondary discriminant using the ratio of sp-P_z:sp-S_z (Woods and Helmberger, 1996) can ascertain that this event could not be an explosion because of its low short-period P to S ratio.

The earthquakes given PDE depths of 33 km lie throughout the two population regions. We suspect that once their depths are determined by our source inversion procedure, each will plot in the correct depth group. Visual inspection of the records support this, i.e. the earthquakes which plot as deep events with respect to their energy ratio have waveforms that are characteristic of deep events.

Our ne task is to determine the depth of events in this data set in order to clear-up the questionable earthquake datum points in the discrimination plots and to confirm the separation of crustal and mantle earthquakes using this measurement. Also as more data from stations and arrays in the study region become available, this discriminant shall be applied to them.

5. Analysis of Short-Period Array Data and Location of Events

To examine the quality of P and pP waveforms recorded teleseismically by short-period arrays, we have compiled data from five arrays, namely the Alice Springs (ASP) and Warramunga (WRA) arrays from Australia, the Gauribidanur (GBA) array from India, the Chiang Mai (CHG) array from Thailand, and the Geress (GER) array from Germany (Figure 40) for all events from Pakistan studied in Section 2. Of these five arrays, the GBA array is located in the upper-mantle range of 22° - 26° and the CHG array is located in the range of 29° - 33° which
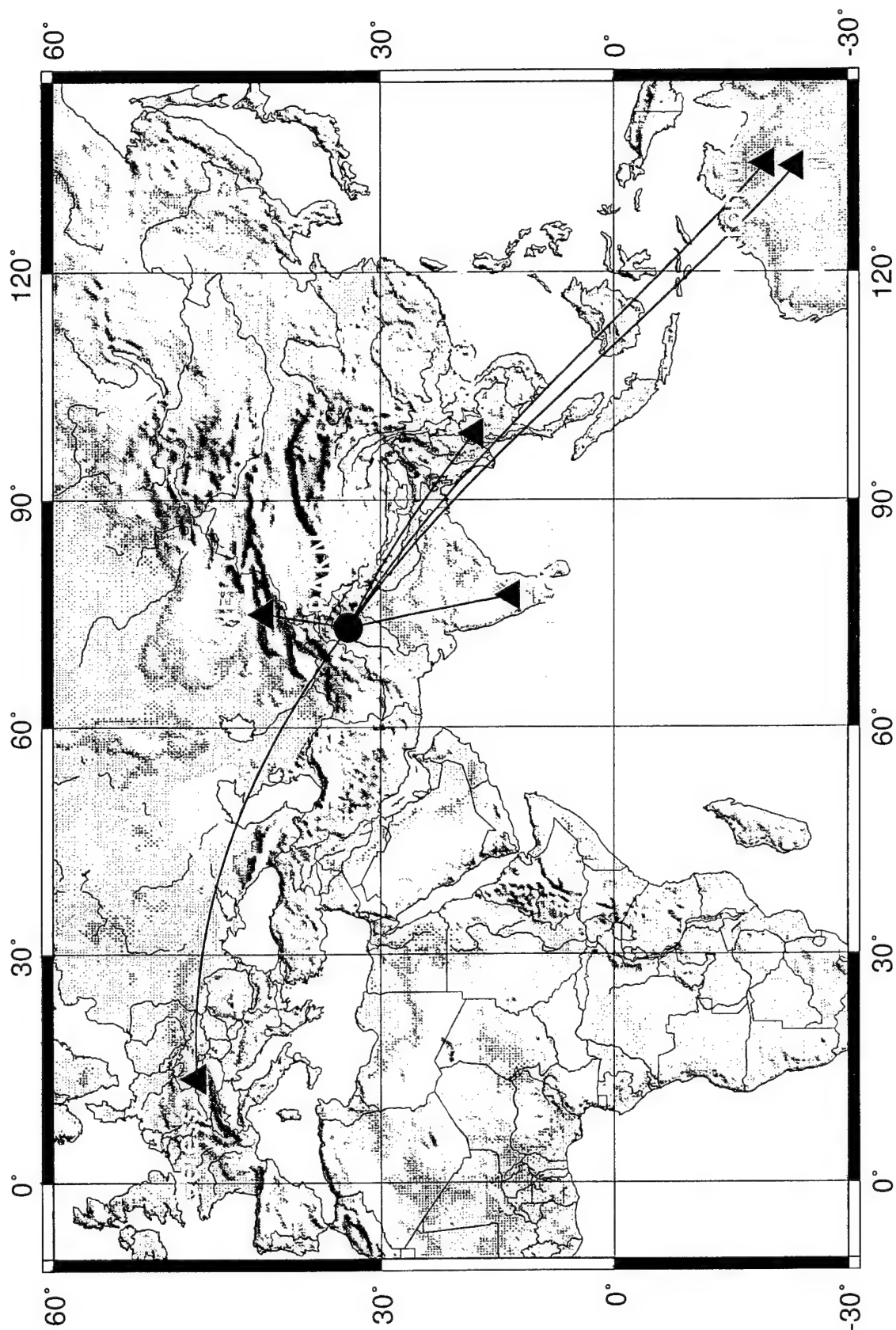
64

Figure 40 Map showing the locations of the Alice Spring (ASP), Warramunga (WRA), Geress (GER), Gauribidanur (GBA) and Chiang Mai (CHG) arrays. Also shown on this map are the PAKN and KNET arrays.

is a transition to the teleseismic range. The Australian arrays are located at about 82° away from the selected events and the waveforms are truly teleseismic.

The initial focus for the installation of short-period arrays was on problems involving seismic detection, location, discrimination, and yield estimation of low-yield events. In addition, array data have proved useful for developing usable empirical discriminants in monitoring regions where there are known earthquakes and explosions (Baumgardt, 1995; Baumgardt and Der, 1994; Fisk *et al.*, 1994). On the other hand, for regions like the Middle East and North Africa where explosion data are lacking and the regions are to be monitored for nuclear technology testing, it is difficult to develop such empirical discriminants. In regions like these, the use of array data becomes restricted to problems related to the detection and location of seismic events. In this section, we investigate the usefulness of teleseismic array data in estimating source depth and source characteristics. This requires analysis of a large data base to understand the strength of the P, pP, and sP phases at a particular array. These phases are dependent on the source mechanism and event size. In particular, we shall show the quality of data recorded by each array and the compatibility of the arrival of the pP phase relative to direct P with the waveforms of these phases predicted by using the depth determined from regional seismograms compiled during the PASCAL experiment in Pakistan (October - December, 1992) and from the KNET array located to the north of PAKR. The PASCAL experiment was performed near the GSETT-3 α array PAKR and GSETT-3 β station NIL (Nilore).

5.1 Data

Both AFTAC (Air Force Technical Application Center, Florida) and CMR (Center for Monitoring Research, Arlington, VA) helped us obtain the short-period data from various arrays. AFTAC provided us with data from the Chiang Mai array in Thailand. They also provided us with their locations for all ten of the events and m_b estimates for 7 events categorized as non-classified. The Geress Array data from Germany was provided by Dr. M. Jost of Ruhr University, Bochum, Germany. Dr. D. Jepsen of CMR provided access to the Alice Springs, Warramunga and Gauribidanur array data. All these data came in the CSS format and were converted to sac format using CSS2SAC version 3. All the "wfdisc" files had calibration period of 1s with the "calib" parameter (gain) equal to unity.

Figure 41 shows examples of array data recorded at station AS03 of the Alice Springs array in Australia plotted in decreasing order of magnitude from the top. The solid vertical line shows the P-wave arrival time from the ISC monthly bulletin. The event 317.2041 occurred on November 12, 1992 and its time series starts 709.8s after the origin time of 20h41m04.6s (PDE). This is a deep event (h=180 km, regional solution) and the other three events are shallow. Clearly, this array is able to record the Pakistani events with good signal-to-noise ratios (SNR) down to a magnitude (M_w) of 4.7. We have plotted the 311.1147 event twice. The top trace represents a processed time series obtained by stacking all the time series recorded by the array. The bottom trace shows the waveform recorded at a single station AS03. Both these time series are filtered with a low cut of 0.7 Hz and a high cut of 5.0 Hz and indicates the typical enhancement achieved by stacking.

Figure 42 shows seismograms recorded at station WR5 of the Warramunga array in Australia. The quality of seismograms recorded by this array is quite good down to a magnitude (M_w) of 4.7 and becomes noisy at 4.0. The event 289.0242 is a small event (M_w=4.0) and its time series were also stacked, with the stacked version is presented in the upper trace. For this event, the stacking did not produce a clear onset like that of the event 311.1147 at ASP. Both these arrays are located at teleseismic distances and seismic rays travel mostly through the lower mantle avoiding the complexity of the upper-mantle and crust, thus making the onset of direct P and depth phases simple and easy to model.

Figure 43 shows waveforms recorded at the GBA array. Although this array is located close to the source region (near 20°), the waveforms are complex except for the deep earthquake 317.2041 as the waves tend to sample the upper-mantle triplications. Although the waveforms do indicate some complexity from the upper-mantle triplication, the added strength of arrivals allows the array to efficiently detect events down to M_w of 4.0, including the shallow events, as shown, for example in the time series of 289.0242. For these events, a major portion of the wave propagation path is through the more homogeneous shield structure of Southern India and could be the reason for this detection capability.

Figure 41. Seismograms recorded at AS03 station of the ASP array from several Pakistani events. These waveforms are shown as a function of magnitude. The solid vertical lines are the arrivals of P waves from the ISC monthly bulletin. The bottom two waveforms are a filtered version (bandpassed with a low cut of 0.7 Hz and a high cut of 5.0 Hz). The top seismogram for event 311.1147 is the stacked version of all time series recorded at ASP.

Figure 42. Seismograms recorded at WR5 station of the WRA array from several Pakistani events. These waveforms are shown as a function of magnitude. The solid vertical lines are the arrivals of P waves from the ISC monthly bulletin. The bottom two waveforms are a filtered version (bandpassed with a low cut of 0.7 Hz and a high cut of 5.0 Hz). The top seismogram for event 289.0242 is the stacked version of all time series recorded at WRA.

WAVEFORM OF PAKISTANI EARTHQUAKES (1992)
GAURIBIDANUR ARRAY, INDIA
Station: GBR5 (Approx:22-25 Deg)

328.2311
23h11m06.7s
308.3s
.557E+03
M_w=5.1

322.0238
02h38m50.1s
279.7s
.719E+02
M_w=4.7

311.1147
11h47m42.9s
272.5s
.254E+02
M_w=4.3

289.1942
19h42m11.8s
296.2s
.449E+02
M_w=4.2

289.0246
02h42m06.3s
322.7s
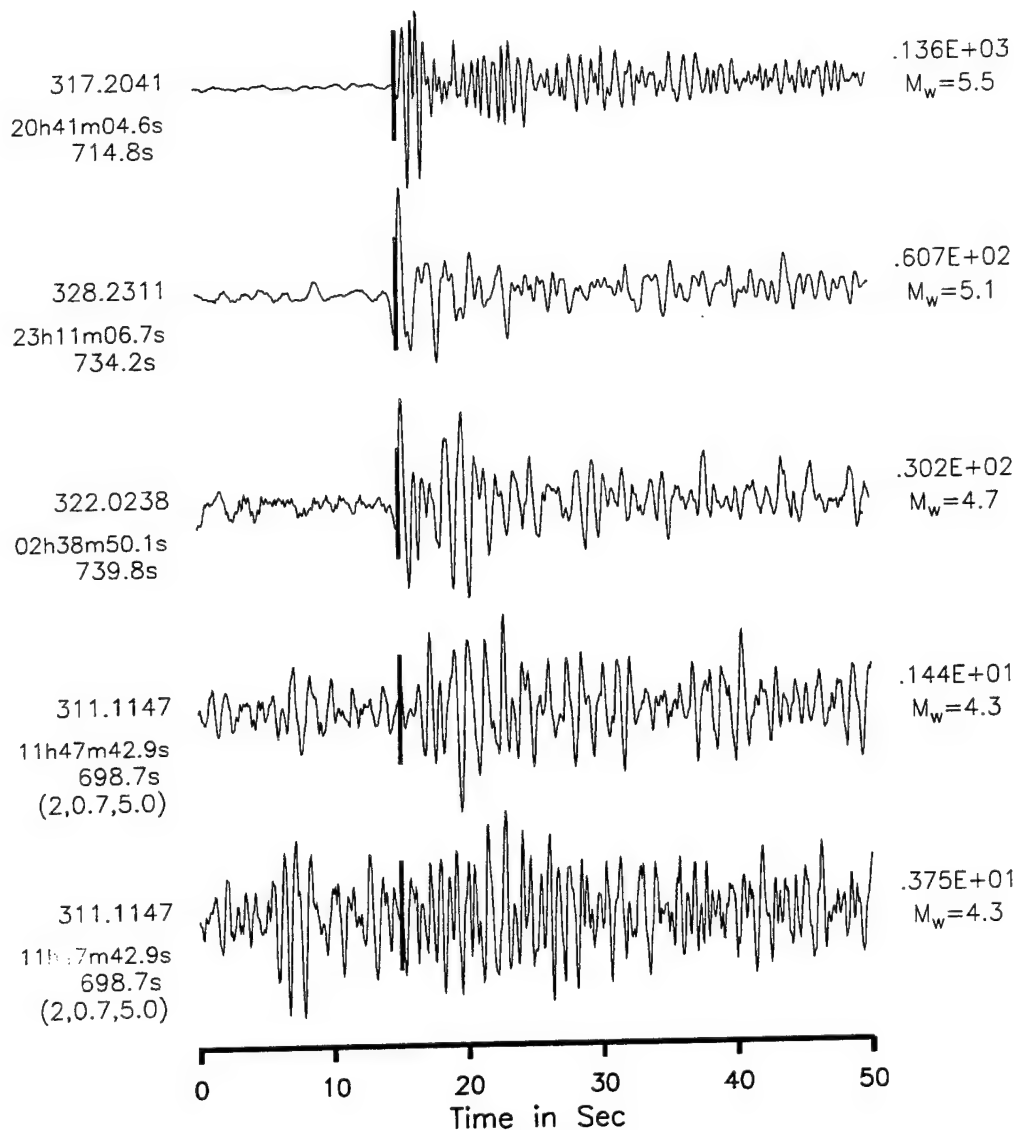.105E+02
M_w=4.0

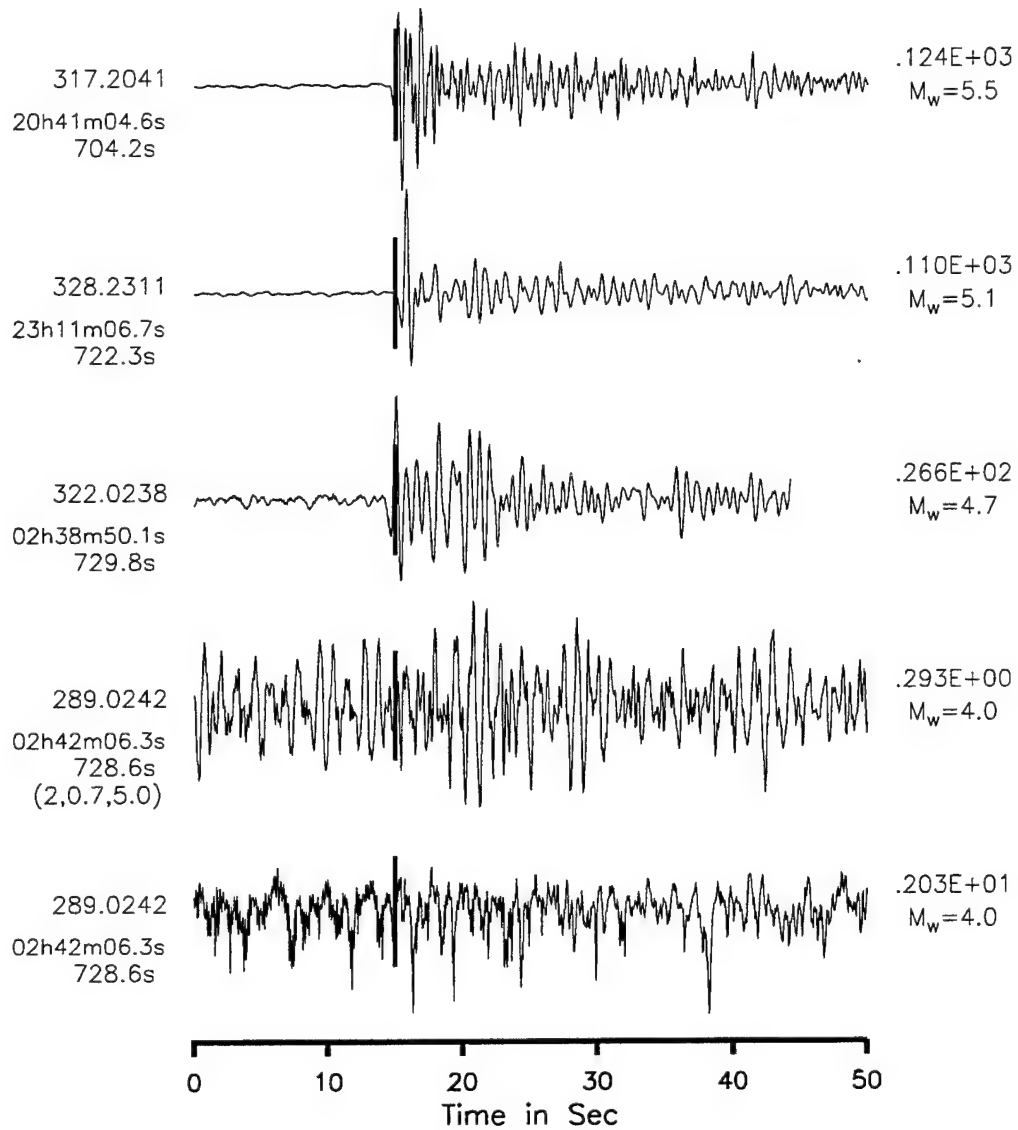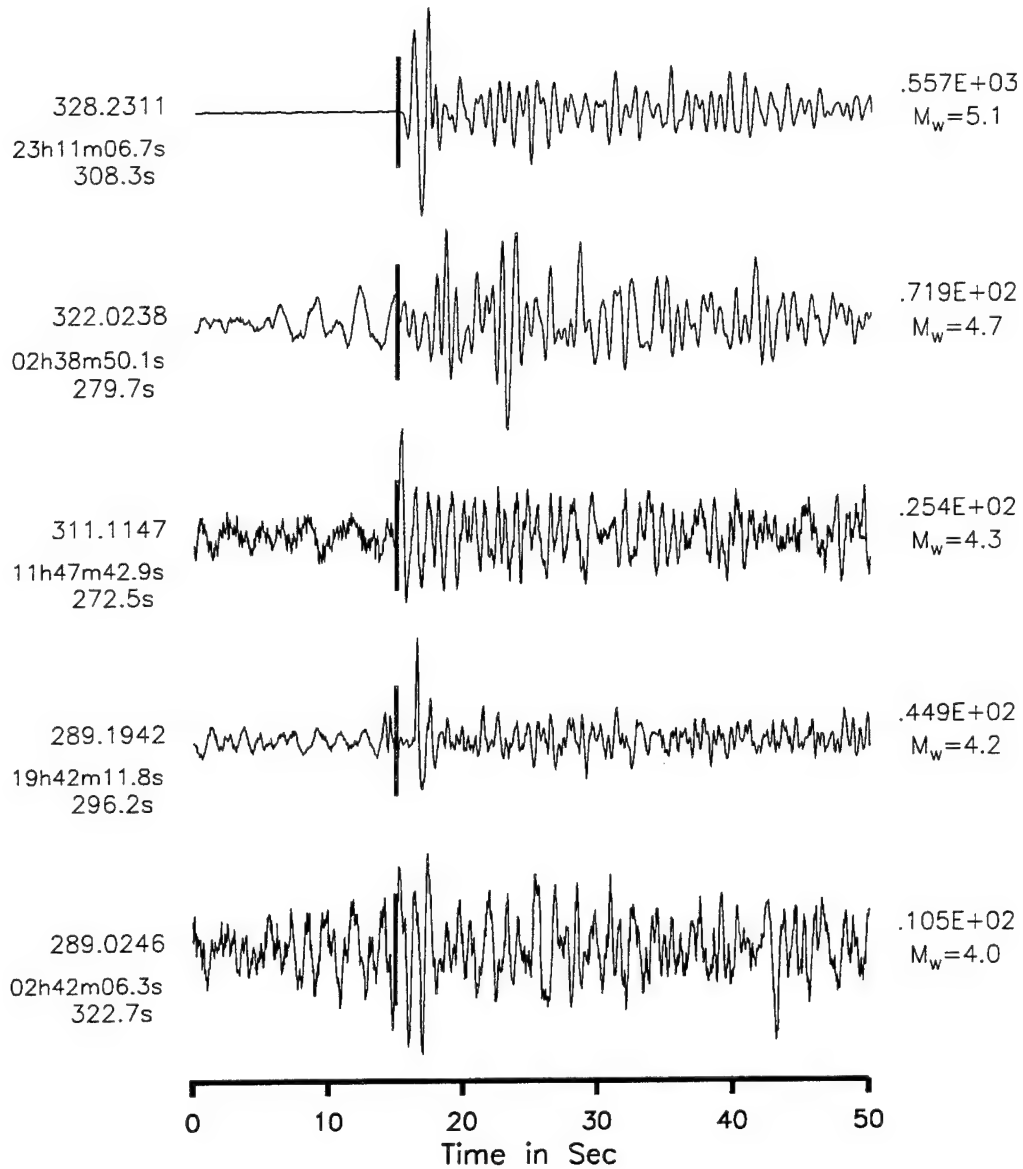0   10   20   30   40   50
Time in Sec

Figure 43. Seismograms recorded at GBR5 station of the GBA array from several Pakistani events. These waveforms are shown as a function of magnitude. The solid vertical lines are the arrivals of P waves from the ISC monthly bulletin.

70

The Chiang Mai array in Thailand is located near the onset of the teleseismic range and shows more complexity in the seismograms, probably due to the influence of complex path near the receiver (see Figure 44). The major portion of the path from the source region to this array is through the Himalayan geology of Northern India and more conspicuously through the most complicated crustal geology of Indo-Burma at the receiver. The detection capability of this network for Pakistani events is probably around M_w of 4.4. For all these events, the Geress array data are dominated by high-frequency noise. However, signals could be recovered in the bandwidth of 0.7 to 2.0 Hz, a filter which was suggested by Dr. Jost (personal communication).

Appendix I shows more examples of seismograms from different stations for several small magnitude Pakistani earthquakes from the five short-period arrays. Each event is accompanied by a caption which includes its depth and magnitude as reported by the monthly PDE bulletin. The reason for including these waveforms in this report is to demonstrate that for small events, teleseismic identification of depth phases can be quite ambiguous, especially for small events with poor signal-to-ratio. The small deep events are generally problematic as they appear explosion like in the discriminant analysis.

5.2 Instrument Response

The instrument response files of individual arrays were provided by AFTAC and CMR either in the form of poles and zeroes or in the form of amplitude and phase values at discrete frequencies between 0.1 and 10 Hz. The normalization frequency for all these arrays is 1 Hz except for the Geress array instruments for which the normalization frequency is 5 Hz. Of the five arrays, the instrument responses for GBA, WRA and GER arrays are constructed using the poles and zeroes. To confirm the accuracy of the gain and sensitivity of the instrument response files including the unit which is nanometers, we collected the broadband seismograms recorded at Chiang Mai station (CHTO; 18.79°N, 98.977°E) for the largest event, 317.2041. The CHTO station is located close to CM18 (18.4577°N, 98.9627°E), a station of the Chiang Mai short-period array. Figure 45 shows the comparison of the data recorded by different stations. The uppermost seismogram is the broadband seismogram recorded by CHTO in digital counts. This recording instrument has a sensitivity of 9.74981×10^8 with a normalization frequency of 0.02 Hz. The second seismogram is the actual ground motion in "micron" obtained after removing the

WAVEFORM OF PAKISTANI EARTHQUAKES (1992)
CHIANG MAI ARRAY, THAILAND
Station: CM05 (Approx:30 Deg)

317.2041
20h41m05.2s
338.8s
.457E+03
M_w=5.5

328.2311
23h11m06.7s
351.5s
.609E+02
M_w=5.1

322.0238
02h38m50.1s
367.9s
.159E+02
M_w=4.7

311.1758
17h58m30.0s
371.0s
.467E+01
M_w=4.4

289.0242
02h42m06.3s
358.7s
(2,0.7,5.0)
.271E+01
M_w=4.0

289.0242
02h42m06.3s
358.7s
(2,0.7,5.0)
.439E+01
M_w=4.0

0   10   20   30   40   50
Time in Sec
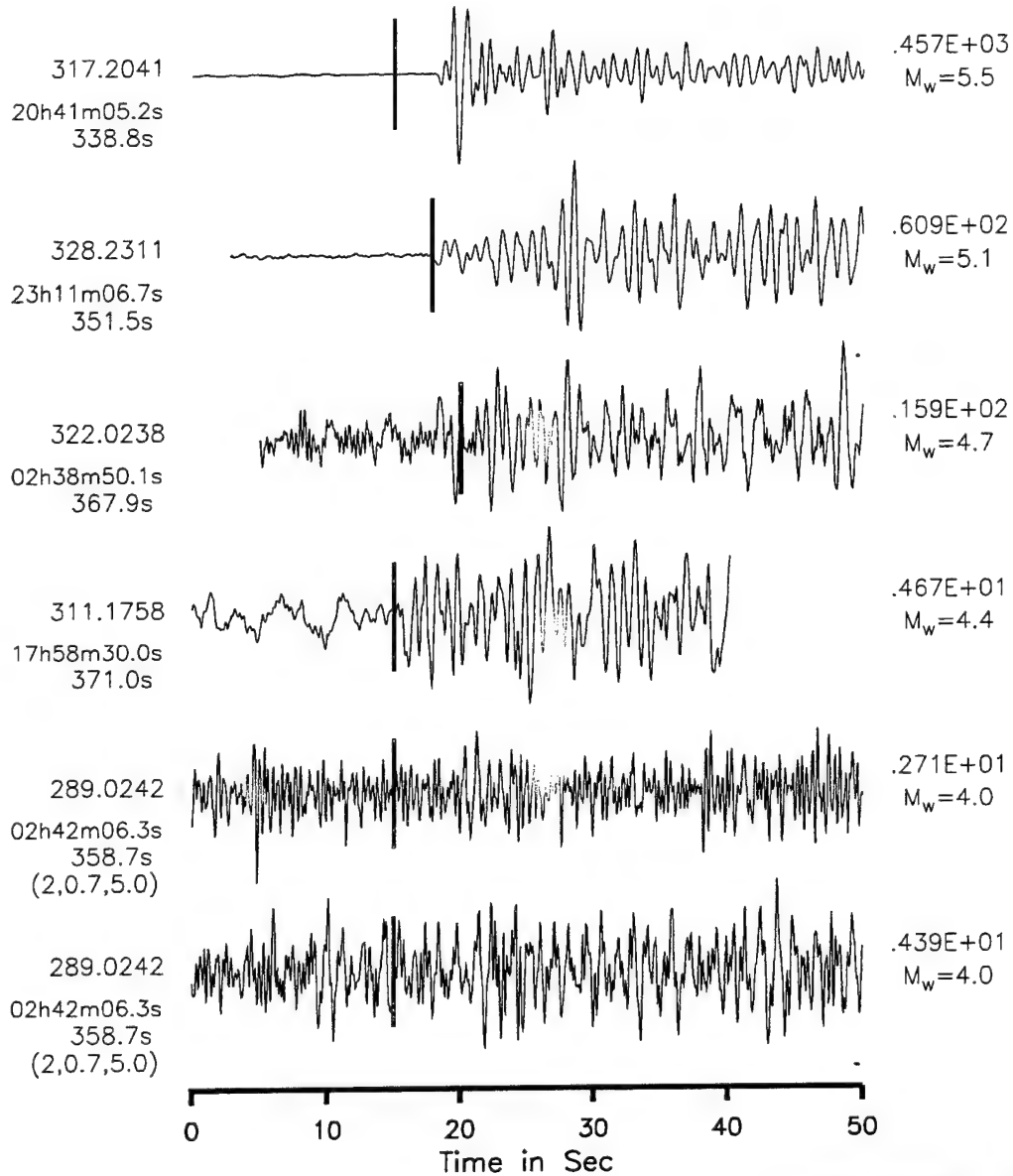
Figure 44. Seismograms recorded at CM05 station of the CHG array from several Pakistani events. These waveforms are shown as a function of magnitude. The solid vertical lines are the arrivals of P waves from the ISC monthly bulletin. The bottom two waveforms are a filtered version (bandpassed with a low cut of 0.7 Hz and a high cut of 5.0 Hz). The top seismogram for event 289.0242 is the stacked version of all time series recorded at CHG.

CHIANG MAI BROADBAND VS ARRAY DATA (CM18,CM02-CM04)
317.2041: 11/12/92 02:41m:4.6s h=198.0km Mb=5.7

CHTO BroadBand — .21773E+04 Counts

DCON — .94900E+00

Simulated to Cheng Mai — .12798E+03 200 Counts at 1 Hz

CM18 — .54465E+03

CM02 — .58841E+03

CM03 — .54237E+03

CM04 — .49495E+03

Time in Sec
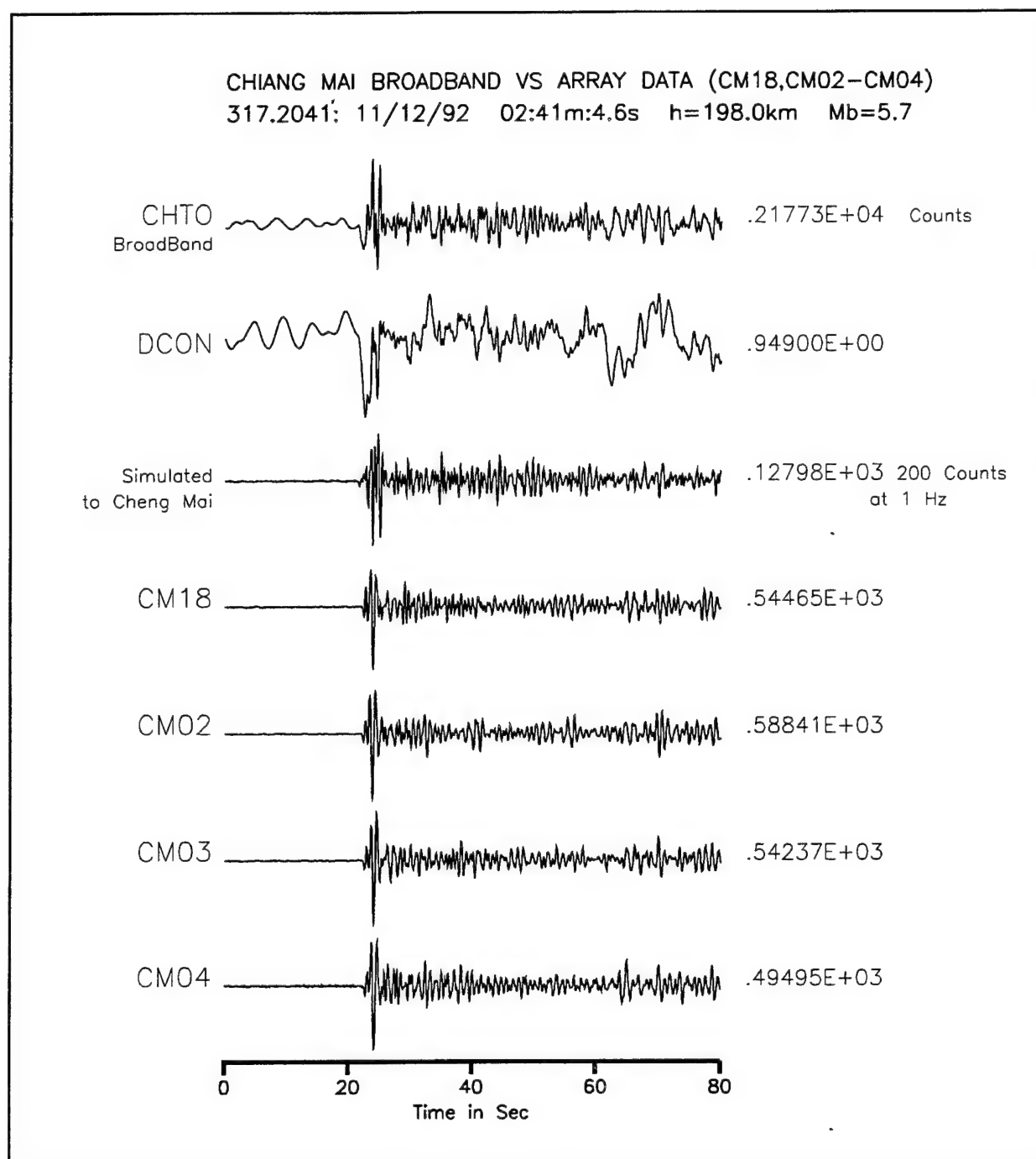
Figure 45. Comparison of simulated CHG seismogram (third from top) with the actual seismograms recorded at CM18, CM02, CM03 and CM04 (stations of Chiang Mai array) for event 317.2041. We deconvolved the broadband instrument response from the CHTO seismogram to obtain DCON (units in microns). DCON was convolved with the instrument response of the CHG array which has 200 counts at 1 Hz. The peak amplitude of this simulated waveform is within a factor of 5 of the peak amplitudes recorded at other CHG stations.

broadband instrument response. We are able to successfully model this waveform and match its peak amplitude using teleseismic modeling techniques. The third seismogram is after convolving the second waveform (units in cm) with the instrument response of the Chiang Mai short-period array. This seismogram has a peak motion of 0.128×10^3 counts. For an input time series in nanometers (10^{-3}microns), the peak motion of this simulated Chiang Mai waveform will have a value of 0.128×10^6 counts. The fourth through sixth waveforms are the actual seismograms recorded by the stations of the short-period Chiang Mai array and the peak amplitudes are in counts. Thus, it appears that the Chiang Mai short-period array instrument response is in "microns" which is assumed while modeling the interaction of P and pP waves.

Figure 46 shows an example of the match in the synthetic peak amplitudes of the direct P waves at ASP, WRA, CHG and GER for this event with the observed peak amplitudes in counts assuming that ground motions are in "microns". Also, the ratios of the observed time series to the synthetic time series included in this figure show that they are in excellent agreement at GER and relatively good agreement at other arrays. For example, the synthetic time series at ASP is within a factor of 0.8 of the observed time series. The largest discrepancy is found at CHG with a factor of 5.2, which is followed by a factor of 4.4 at WRA.

5.3 Variation of Peak Amplitude

The objective of this amplitude study is to determine whether peak ground motions recorded by different short-period arrays show any dependence on the radiation pattern. If it does, then estimating the m_b bias can be seriously influenced unless the radiation effect is adequately accounted for. The influence on the m_b bias will be marginal when peak amplitudes recorded at different arrays lying at various azimuths show a proportionality to the seismic moment M_o. To perform a systematic analysis of this peak amplitude variation, an ideal data set consisting of many waveforms from many large events ($M_w \geq 4.5$) is needed. Our data set is limited and does not allow a rigorous analysis because of the quality of SNR of many of the events. However, we have two large events, namely 317.2041 and 328.2311, which are recorded with good signal-to-noise ratios by a minimum of at least four arrays. These events have different focal mechanisms and source depths. Event 317.2041 has a depth of 180 km and event 328.2311 has a depth of 10 km. Figure 47 shows a comparison of ground motions (in cm) recorded at

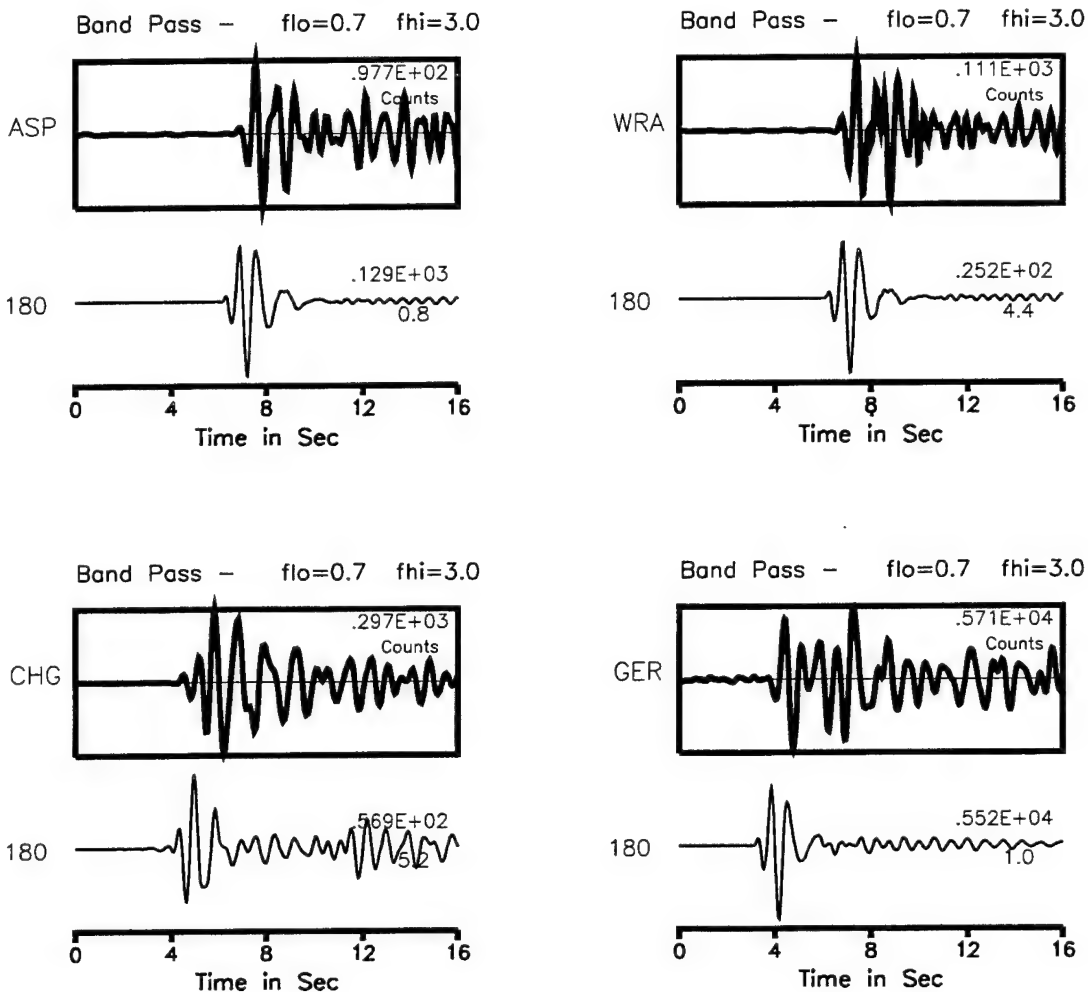Figure 46. Comparison of the synthetic seismograms with the observed seismograms recorded at the ASP, WRA, CHG and GER arrays for event 317.2041. The largest misfit in peak amplitudes (in counts) is at CHG which is within a factor of 5.2. AT GER and ASP, they show excellent agreement. The synthetics are computed with a source depth of 180 km using the focal mechanism and seismic moment presented in Table 3.
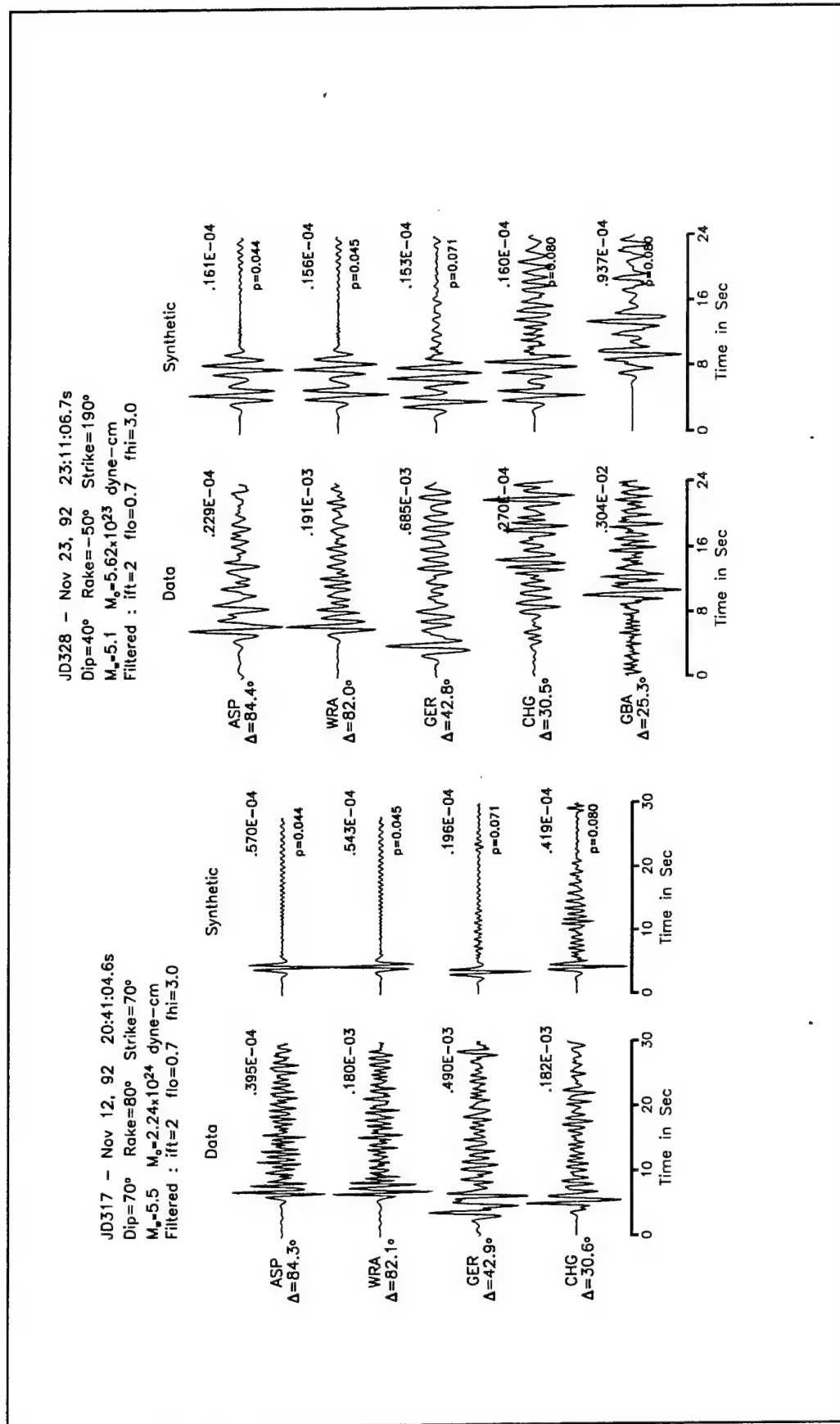
Figure 47. Comparison of the peak synthetic amplitudes with the observed peak amplitudes of the seismograms recorded at ASP, WRA, GER, CHG and GBA arrays for events 317.2041 and 328.2311. The synthetics for event 317.2041 are computed at an azimuth of 124.6° and for event 328.2311 at 126°. The focal mechanism is taken from Table 3. For the radiation effect to be negligible, we expect empirical geometrical spreading to match the theoretical geometrical spreading, but this does not occur.

individual arrays with the ground motions predicted using focal mechanism and source depths from the regional modeling. The correspondence between the recorded and synthetic seismograms at ASP is quite good, but the' observed signal at WRA is stronger by a factor of about 3.5 for event 317.2041 even though the distances to the two arrays are comparable and the azimuths are similar. Note that the peak amplitude ratio changed to over 12.24 for the shallow event 328.2311. The deep event has an amplitude discrepancy of a factor of 25 at GER, but this discrepancy goes away if we account for the radiation pattern (see Figure 46). This type of variation is typical for explosions at NTS, so it is not surprising. Even variation in amplitude by a factor of 25 between WWSSN stations from the same explosion is observed, see Figure 5 of Lay *et al.* (1984) for example. Thus, it becomes quite difficult to recognize radiation patterns without extensive individual station calibration relative to a large network. Probably the most usable information in these waveforms is in the identification of depth phases and the relative size of arrivals on the same seismogram.

5.4 Modeling of the pP Phase

By examining the waveform data, we noticed that depth phases are distinctly observed as well separated from the direct P waves for the deep events. When the events are shallow, the depth phase arrives close to the direct P, and sometimes when the array location is in the upper-mantle triplication range, the interaction is even more complicated as is seen in the GBA data. Arrivals from the 400 km and 600 km discontinuities also appear in this distance range. We have pursued the modeling of depth phases for several reasons. First, we found that locating seismic events using travel times produces depths significantly different from one another depending upon the kind of information used in the location scheme. For example, the ISC and AFTAC locations for event 311.0721 have depths at 21 and 48 km, respectively. For the same event, we obtained a depth of 15 km (see Table 6) by modeling regional seismograms recorded at the PAKN (a temporary network of 11 broadband stations near the proposed PAKN array) and KNET (Kirghyzia network) arrays. We have also located this event using the P and S travel times picked from the PAKN and KNET arrays which produced a source depth of 22.9 km. Augmenting the travel times of the PAKN and KNET arrays with the travel times of impulsive P waves of teleseismic stations from the ISC bulletin increases the depth to 62.6 km. Figure 48 shows the individual locations based on travel times of seismic waves determined by different
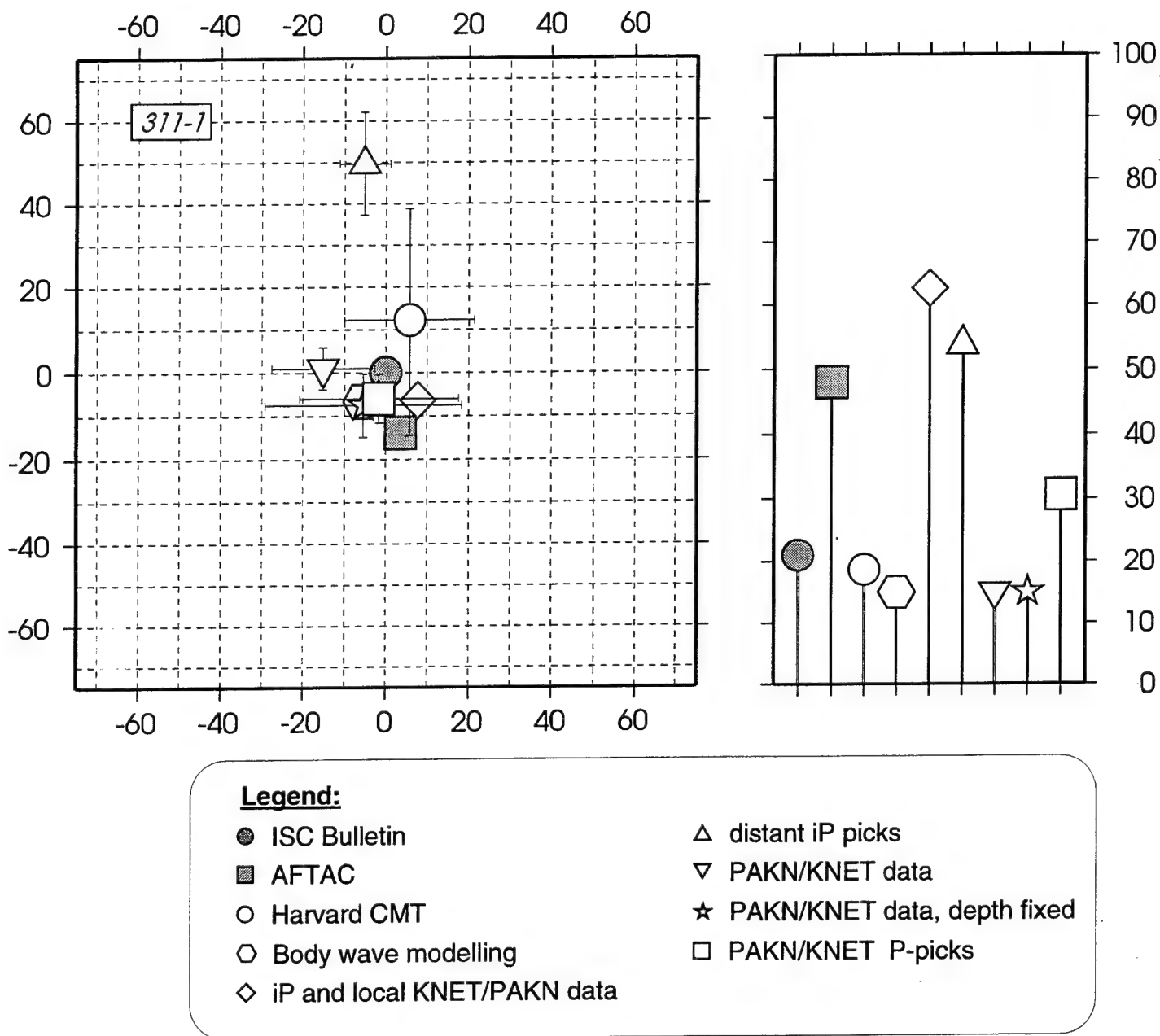
77

Figure 48 Comparison of locations (left panel) and depth (right panel) obtained using different data sets for the event on 92/11/06 07:21 (311-1). All distances are in kilometers. The epicenters are plotted relative to the ISC location. These values are tabulated in Table 9.

organizations. In this figure, we show (X,Y) locations of these sources relative to the ISC location which is centered at (0,0) and their corresponding depths. Such variation in the source location appears to be quite common with all the Pakistani events which is the next topic of our discussion. Teleseismic modeling of pP, as well as the sP phase, can provide some resolution to this depth problem. Secondly, we found that the short-period:long-period regional discriminant cannot differentiate deep earthquakes from explosions (Figure 36b). For such events, knowing the true depth greatly strengthens our regional discriminant.

5.4.1 Modeling Approach

In this study, we follow the standard technique of modeling teleseismic seismograms in the range of 30°-90° (Langston and Helmberger, 1975) and approximate ground motion displacement seismograms using the following expression

$$W(t) = V(t) * I(t) * S(t) * Q(t)$$

$$V(t) = R_{PZ}[\frac{d}{dt}\phi + R_{pP}\frac{d}{dt}\phi . H(t - \Delta t_1) + (R_{sP}\frac{\eta_\alpha}{\eta_\beta})\frac{d}{dt}\Omega . H(t - \Delta t_2)] \qquad (8)$$

where

R_{PZ} = vertical P-wave receiver function

R_{pP} = reflection coefficient of pP

R_{sP} = reflection coefficient of sP

$S(t)$ = far-field dislocation function

$Q(t)$ = attenuation Q operator

$I(t)$ = Instrument $\qquad\qquad$ (9)

Δt_1 = time lag of pP relative to the direct P

Δt_2 = time lag of sP relative to the direct P

η_α = vertical slowness for P wave

η_β = vertical slowness for S wave

$H(t - \Delta t)$ = lagged heavyside step function

Expressions for Φ and Ω can be found in Langston and Helmberger (1975).

5.4.2 Data Modeling

The five arrays from which we have short-period data scan distances from 22° to 86°, sampling different regions as well as different tectonic settings. The GBA array is located within a shield region and to model seismograms recorded at GBA we used the S25 (LeFevre and Helmberger, 1989) Canadian Shield velocity model and for the other arrays we used the PREM (Dziewonski and Anderson, 1983) velocity model. Green's functions were computed using these models and were convolved with the sources and instruments to obtain the predictions. For each event, we predicted waveforms for a suite of depths, including the regional waveform modeling solution. We display the observed seismograms within the rectangular boxes. The observed waveform selected in each box is from a station within the individual array having the best signal-to-noise ratio, except for the Geress array. The Geress Array data were stacked to obtain the best signal-to-noise ratio. Peak amplitudes are given in counts. Whenever a filter was needed to enhance the signal, we used a causal sixth-order bandpass butterworth filter with the low cut "flo" and high cut "fhi" values given in each figure.

Figure 49 shows the agreement of observed waveforms with synthetics for the event 322.0238. The observed pP phase is distinct and has the same strength as that of the direct P, a feature which is nicely modeled in the synthetics. Of the five arrays, ASP shows a distinctive pP phase in the data and its timing separation of about 3s from the direct P is compatible with a source depth of 10 km which is in agreement with the regional depth estimate. At WRA, some strong ringing appears 2 seconds after the pP phase which suggests the presence of some receiver related phenomena which cannot be produced in the synthetics using our simple modeling approach. The pP phase also is picked up by the remaining three arrays. At GBA, the onset of the direct P wave is somewhat complicated due to noise. The strong phase 3s ahead of the pP phase is the likely onset of direct P. We notice three distinct phases in the waveform recorded by CHG, of which the first two are the direct P and pP, respectively. The third strong phase is probably produced by a reflector located at about 600 km which is not modeled as strongly on the synthetic, but this phase can be seen on the seismogram generated for a source depth of 5 km. The agreement observed in travel-time separation for pP and P phases at GER also suggests

Figure 49. Comparison between data and a suite of synthetic seismograms at ASP, WRA, GBA and CHG for event 322.0238. The depth of each synthetic waveform is given at the left of the trace. The number at right and below the trace is the ratio of observed to synthetic peak amplitude. Peak amplitudes are in digital counts.

81
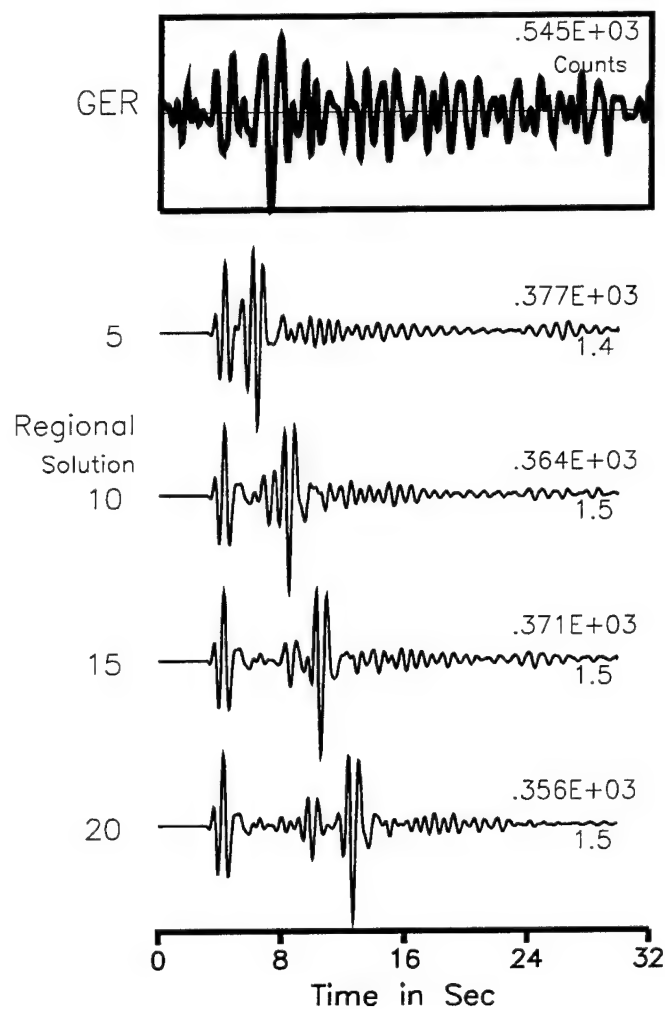
Figure 49. (Continued). Comparison of data with synthetic seismograms for GER. Regional depth of 10km produces the best agreement.

that this event is located at a depth of 10 km. The depth of this event was estimated at 35 km and 33 km by ISC and AFTAC, respectively with the (X,Y) coordinates of AFTAC being offset by (0.08°,0.08°) from the ISC location.

The only usable data for the event 289.0242 is from the Geress Array (Figure 50). The regional source solution has a depth of 20 km for this event. The teleseismic analysis of this event has failed to confirm this depth. In fact, we could not identify a depth phase on the teleseismic data.

Figure 51 shows comparisons of the observed waveforms with synthetics for source depths of 5, 10, 15 and 40 km for event 328.2311. This is a shallow event and regional modeling yielded a source depth of 10 km (see Table 2) or perhaps slightly deeper (15 km) depending on the constraints (Table 6). Although the regional waveform modeling of this event produced a focal mechanism only slightly different from that of event 322.0238, the depth phase does not separate distinctively from the direct P wave. The significant second pulse following the direct P is likely the pP phase. The synthetic waveforms show a distinct move-out for the pP phase relative to direct P and indicates that pP is as strong as the direct P. This feature could not be observed clearly in the ASP, CHG, GBA and GER array data, but only by WRA which indicates that the event may be shallower than 10 km. Both PDE and AFTAC estimated the depth of this event at 41 km which is significantly deeper. The observed data do not show any strong arrival around the time window of the pP phase that can be seen on the synthetic computed for 40 km source depth.

Figure 52 shows the depth phase modeling for event 311.0721. This is a shallow event and has a depth of 10 km from Table 2 and 15 km from Table 6. The depth phase is clearly observed at both ASP and WRA, roughly between $M = 10$ and $h = 15$. Teleseismic modeling shows excellent agreement with the regional depth estimate. The waveforms are complicated at both GBA and CHG arrays. Figure 53 shows the prediction for teleseismic depth phase for event 311.1758 which is a relatively small event ($M_w=4.4$). For this event, we found it almost impossible to identify the teleseismic depth phase.
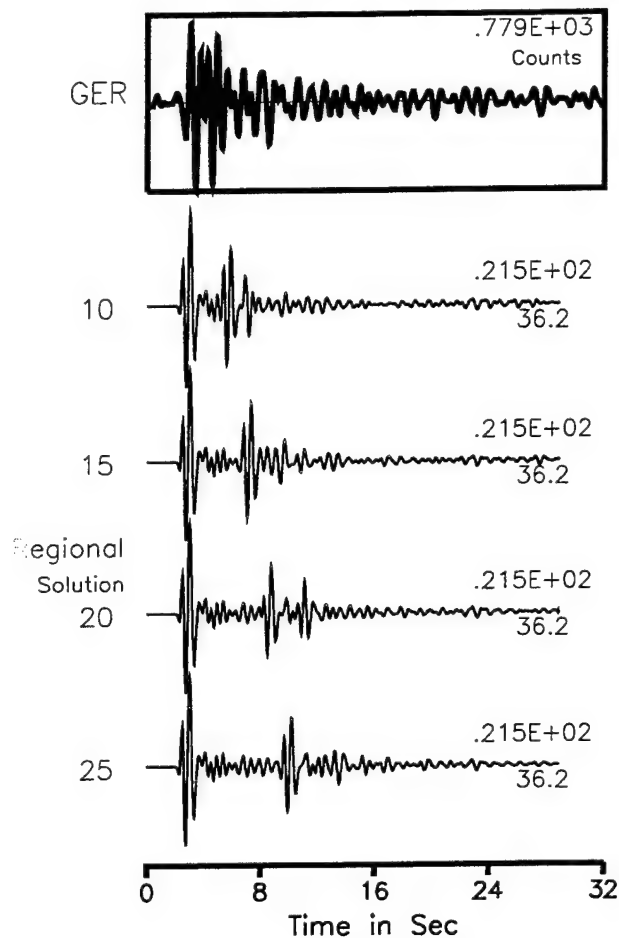
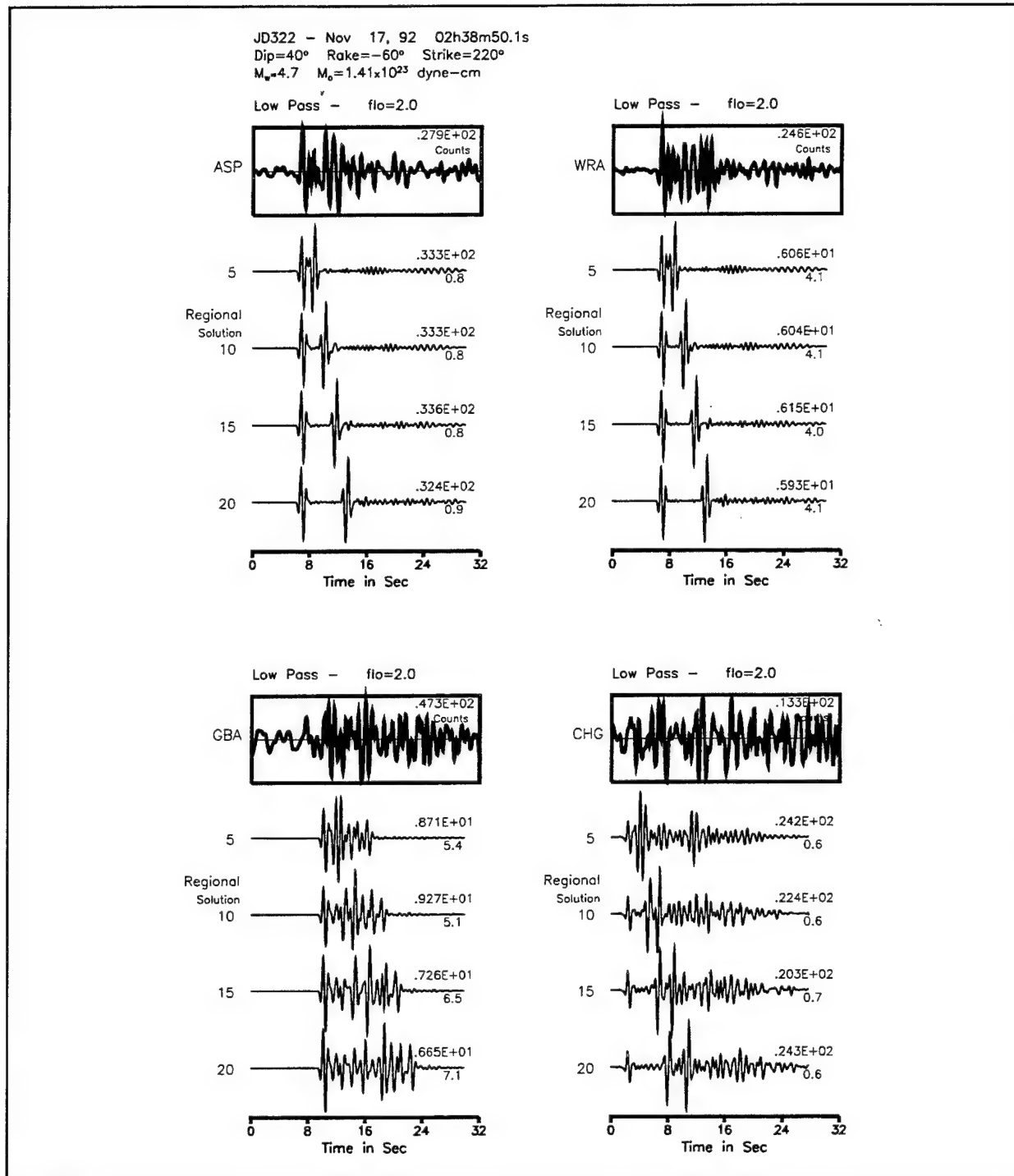Figure 50.   Comparison between data and a suite of synthetic seismograms at GER for event 289.0242.   The depth of each synthetic waveform is given at the left of each trace. The number at the right and below the trace is the ratio of the observed to the theoretical peak amplitude. Peak amplitudes are in digital counts.

Figure 51. Comparison between data and a suite of synthetic seismograms at ASP, WRA, GBA and CHG for event 328.2311. (Peak amplitudes are in digital counts).

JD328 — Nov 23, 92 23h11m6.7s
Dip=40° Rake=−50° Strike=190°
M_w=5.1 M_o=5.62x10^{23} dyne−cm

Band Pass — flo=0.7 fhi=2.0

GER

.601E+04
Counts

5

.174E+03
34.5

Regional
Solution

10

.138E+03
43.6

15

.138E+03
43.6

40

.138E+03
43.6

0   8   16   24   32
Time in Sec

Figure 51 (contd). Comparison between data and a suite of synthetic seismograms at GER for event 328.2311.

Figure 52. Comparison between data and a suite of synthetic seismograms at ASP, WRA, GBA and CHG for event 311.0721. Peak amplitudes are in digital counts.

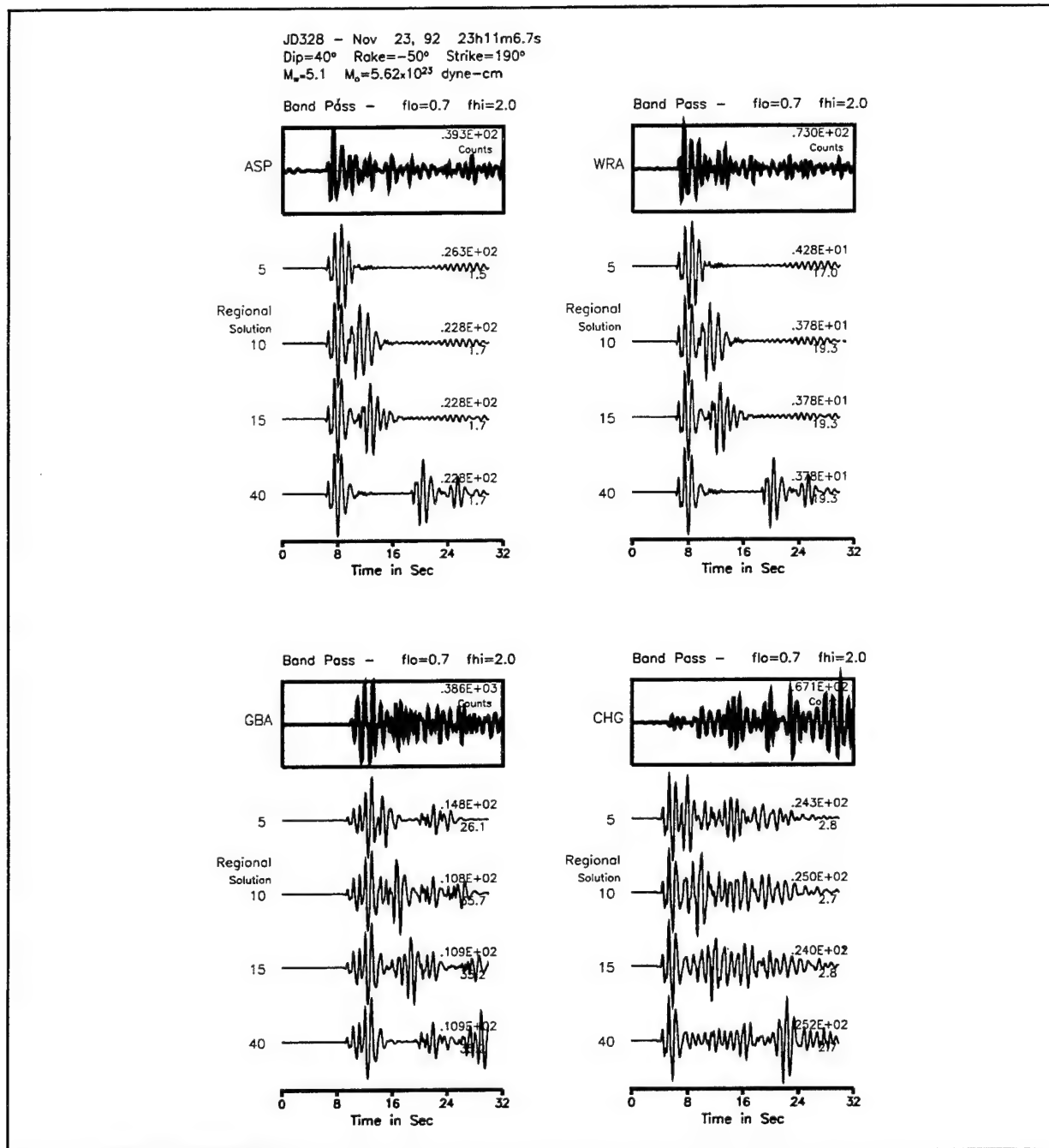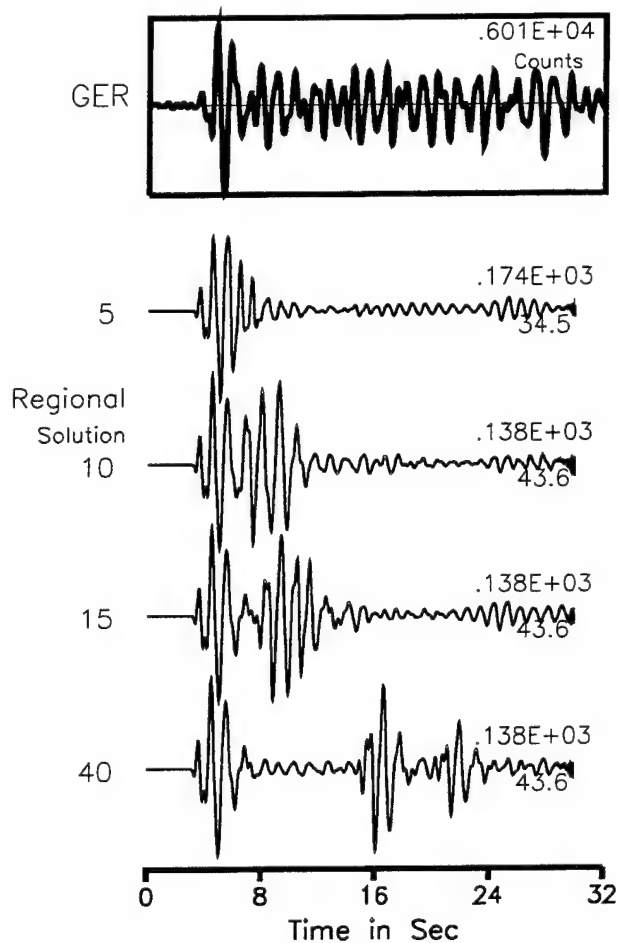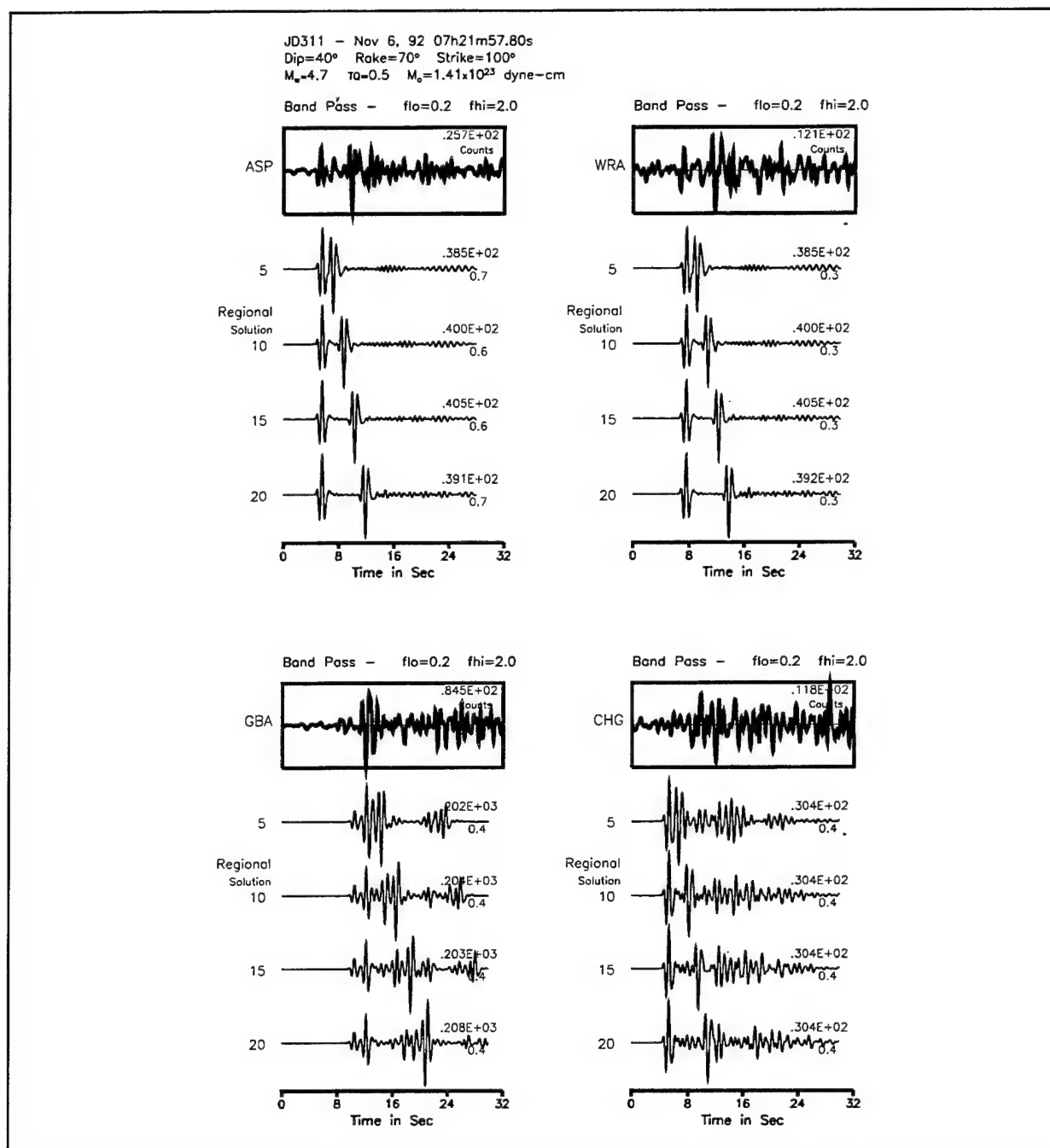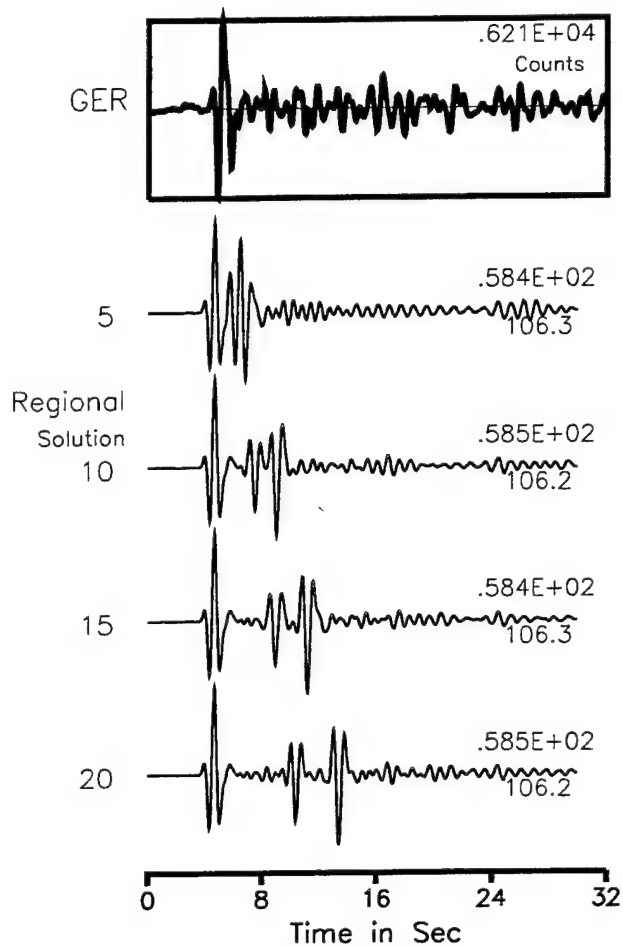Figure 52 (contd). Comparison between data and a suite of synthetic seismograms at GER for event 311.0721.
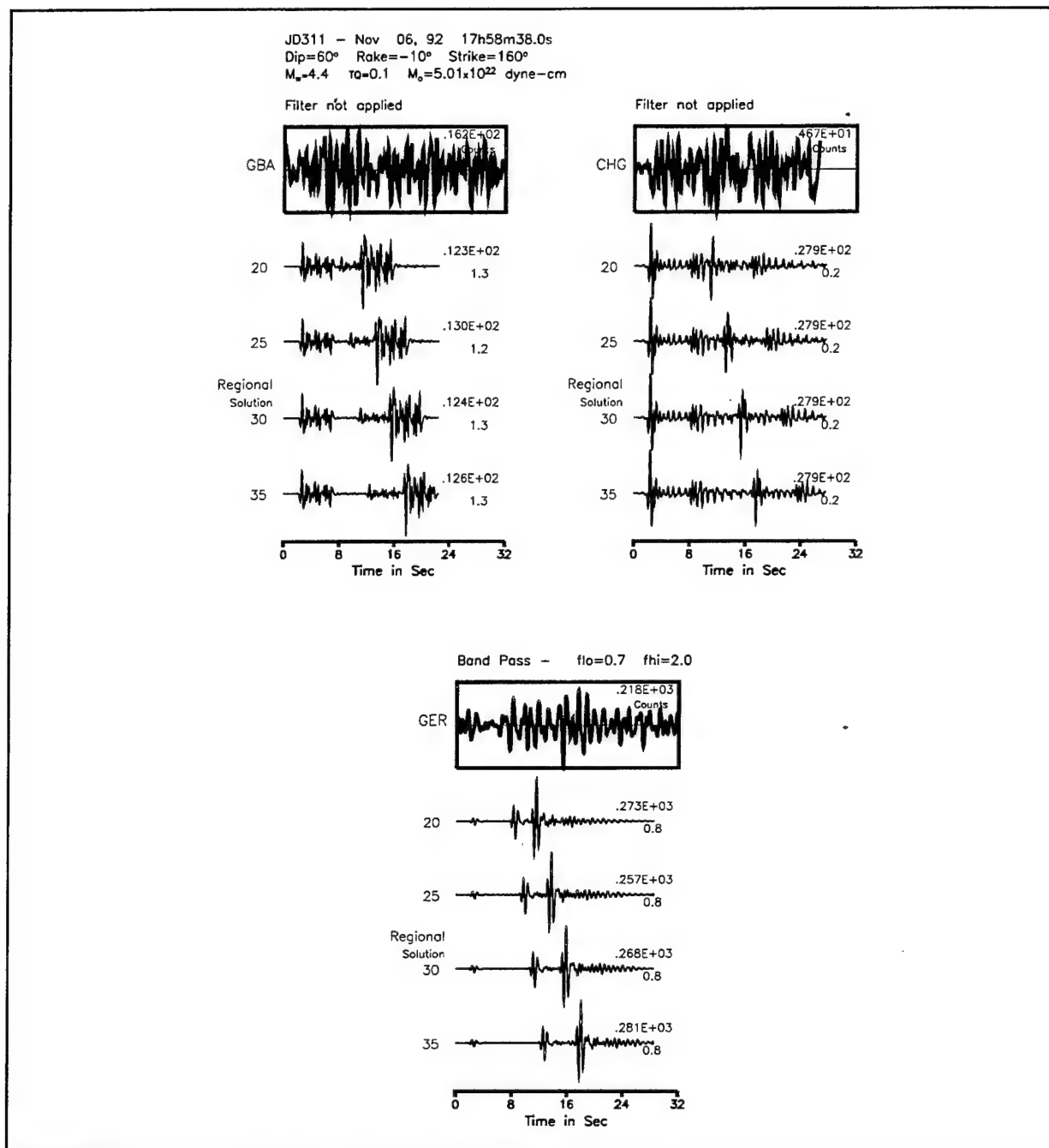
Figure 53. Comparison between data and a suite of synthetic seismograms a GBA, CHG and GER for event 311.1758. Peak amplitudes are in digital counts.

In summary, our experience with the analysis of limited array data indicates that the short-period teleseismic data alone cannot provide sufficient evidence for source depths for the Pakistani earthquakes, especially for the low-magnitude events. However, of the stations studied, the array ASP seems to be naturally calibrated in amplitude (agrees very well with local data) and thus quite useful in predicting the true strengths of events from the Hindu-Kush region. We plan to further document such calibrations as the NIL study is developed.

5.5 Relocation

In this section, we relocated all the Pakistani events using the HYPOCENTER program developed by Lienert and Havskov (1995). We used travel times of impulsive P (iP) from the ISC bulletins and augmented these travel times with additional travel time picks from the PAKN and KNET stations to determine the locations. For locations which include teleseismic picks, we used the iasp91 model (Kennett and Engdahl, 1991). For locations using the local (KNET and PAKN) arrays we used several other crustal models, namely the Tibet model of Zhu and Helmberger (1995), the crustal model suggested in Roecker *et al.* (1993) and a new model developed to fit regional data (see Figure 29). This model consists of twelve flat layers and works better than the first two and we will present those results only. We also relocated the events by keeping the depth fixed at the depth determined by modeling discussed earlier in Section 3 (Table 6).

Table 9 and Figure 54 show a comparison of our various locations with the ISC bulletin locations, and AFTAC locations, as well as the Harvard CMT locations whenever available. The ISC and AFTAC locations are generally in agreement. In general, the locations using the Pakistani array data or using the combined PAKN and KNET data remain within one-half a degree of the locations provided by AFTAC or ISC.

In the following discussion, we refer to our results from the inversion of KNET and PAKN travel time data as "local" results. Whenever we did not have KNET data, we included the P-wave travel time pick from the ISC bulletin for station FRU, which is located within the KNET locale. We also inverted only the P-wave travel times picked from the ISC bulletins for stations

Table 9: Hypocenter Locations by Various Methods

	yr/mo/dy	,h:m:s	Lat. °N	Long. °E	depth	method
276.1432						
1	92/10/02	14:38:46.4	38.08	73.12	139.0	ISC
2	92/10/02	14:38:51.6	38.043	73.014	168.0	AFTAC
4	92/10/02	14:38:46.8	38.10	73.12	150.0	Grid search
5	92/10/02	14:38:47.60	38.049	73.149	135.2	all
6	92/10/02	14:38:45.7	38.106	73.107	113.3	distant-p
7	92/10/02	14:38:47.3	38.134	73.195	84.1	local
8	92/10/02	14:38:46.5	38.135	73.064	150.0	local-fixed
9	92/10/02	14:38:46.1	38.132	73.061	161.3	local-p
289.0242						
1	92/10/15	02:42:06.7	39.24	72.80	16.0	ISC
2	92/10/15	02:42:14.1	39.337	72.924	58.0	AFTAC
4	92/10/15	02:42:08.0	39.50	72.96	20.0	Grid search
5	92/10/15	02:42:12.00	39.616	72.523	15.0	all
6	92/10/15	02:42:22.2	39.139	70.084	15.0	distant-p
7	92/10/15	02:42:06.8	39.516	73.347	0.0	local
8	92/10/05	02:42:08.0	39.548	72.943	20.0	local-fixed
9	92/10/15	02:42:07.0	39.539	72.963	9.6	local-p
289.1942						
1	92/10/15	19:42:13.8	38.20	74.44	157.0	ISC
2	92/10/15	19:42:19.7	38.180	74.278	188.0	AFTAC
4	92/10/15	19:42:13.4	38.24	74.40	160.0	Grid search
5	92/10/15	19:42:12.60	38.495	72.152	15.6	all
6	92/10/15	19:42:15.0	38.169	74.262	147.4	distant-p
7	92/10/15	19:42:14.3	38.279	74.125	126.2	local
8	92/10/15	19:42:13.5	38.275	74.167	160.0	local-fixed
9	92/10/15	19:42:13.5	38.276	74.162	159.9	local-p
292.1614						
1	92/10/18	16:14:46.1	42.14	73.13	19.0	ISC
2	92/10/18	16:14:49.1	42.132	73.117	26.0	AFTAC
5	92/10/18	16:14:50.60	42.280	73.234	36.6	all
6	92/10/18	16:14:49.5	42.457	73.143	18.1	distant-p
7	92/10/18	16:14:45.4	42.212	73.042	15.0	local
8	92/10/18	16:14:46.7	42.131	73.205	19.0	local-fixed
9	92/10/18	16:14:46.5	42.116	73.212	15.0	local-p

Table 9: Hypocenter Locations by Various Methods (Continued)

	yr/mo/dy	h:m:s	Lat. °N	Long. °E	depth	method
311.0721						
1	92/11/06	07:21:56.0	41.09	72.50	21.0	ISC
2	92/11/06	07:22:00.7	40.965	72.550	48.0	AFTAC
3	92/11/06	07:21:58.7	41.20	72.58	18.7	Harvard
4	92/11/06	07:21:54.3	41.03	72.42	15.0	Grid search
5	92/11/06	07:22:01.40	41.032	72.609	62.6	all
6	92/11/06	07:22:03.4	41.537	72.428	53.8	distant-p
7	92/11/06	07:21:53.4	41.099	72.288	15.0	local
8	92/11/06	07:21:54.3	41.022	72.424	15.0	local-fixed
9	92/11/06	07:21:55.6	41.036	72.478	30.6	local-p
311.1758						
1	92/11/06	17:58:39.0	34.87	69.15	25.0	ISC
2	92/11/06	17:58:38.8	34.922	69.294	9.0	AFTAC
4	92/11/06	17:58:36.4	34.67	69.23	20.0	Grid search
5	92/11/06	17:58:37.20	34.838	68.998	0.0	all
6	92/11/06	17:58:40.1	34.841	69.311	20.8	distant-p
7	92/11/06	17:58:32.1	34.776	68.877	15.0	local
8	92/11/06	17:58:35.9	34.707	69.155	20.0	local-fixed
9	92/11/06	17:58:43.0	34.777	69.443	100.7	local-p
317.2041						
1	92/11/12	20:41:05.2	36.45	70.87	204.0	ISC
2	92/11/12	20:41:09.8	36.404	70.863	233.0	AFTAC
3	92/11/12	20:41:08.0	36.57	70.78	188.0	Harvard
4	92/11/12	20:41:04.6	36.55	70.85	190.0	Grid search
5	92/11/12	20:41:05.80	36.433	70.925	196.3	all
6	92/11/12	20:41:05.5	36.400	70.910	194.7	distant-p
7	92/11/12	20:41:03.9	36.578	71.058	204.1	local
8	92/11/12	20:41:04.7	36.627	70.989	190.0	local-fixed
9	92/11/12	20:41:04.1	36.586	71.071	210.7	local-p
322.0238						
1	92/11/17	02:38:50.7	33.83	67.53	35.0	ISC
2	92/11/17	02:38:52.3	33.75	67.46	33.0	AFTAC
3	92/11/17	02:38:49.1	33.15	67.18	33.0	Harvard
4	92/11/17	02:38:45.4	33.89	67.47	10.0	Grid search
5	92/11/17	02:38:51.80	33.950	67.300	34.3	all
6	92/11/17	02:38:51.2	33.775	67.446	26.6	distant-p
7	92/11/17	02:38:55.2	34.509	68.284	0.0	local
8	92/11/17	02:38:43.6	33.916	67.207	10.0	local-fixed
9	92/11/17	02:38:41.8	33.867	67.104	5.0	local-p

Table 9: Hypocenter Locations by Various Methods (Continued)

|	yr/mo/dy	, h:m:s	Lat. °N	Long. °E	depth	method
328.2311						
1	92/11/23	23:11:06.9	38.57	72.65	43.0	ISC
2	92/11/23	23:11:09.0	38.602	72.746	41.0	AFTAC
3	92/11/23	23:11:07.9	38.70	72.38	44.0	Harvard
4	92/11/23	23:11:03.7	38.63	72.63	15.0	Grid search
5	92/11/23	23:11:04.70	38.857	72.942	15.0	all
6	92/11/23	23:11:06.3	38.849	72.634	15.0	distant-p
7	92/11/23	23:11:01.9	38.615	73.071	0.3	local
8	92/11/23	23:11:02.6	38.627	72.593	15.0	local-fixed
9	92/11/23	23:10:51.0	38.732	70.184	15.0	local-p
341.0344						
1	92/12/06	03:44:29.3	37.79	72.19	122.0	ISC
2	92/12/06	03:44:29.5	37.815	72.243	100.0	AFTAC
4	92/12/06	03:44:28.9	37.83	72.19	110.0	Grid search
5	92/12/06	03:44:31.40	37.689	72.353	137.2	all
6	92/12/06	03:44:30.1	37.666	72.361	126.5	distant-p
7	92/12/06	03:44:29.6	37.466	72.231	15.0	local
8	92/12/06	03:43:50.4	40.673	71.942	110.0	local-fixed
9	92/12/06	03:44:28.9	37.531	72.186	18.7	local-p
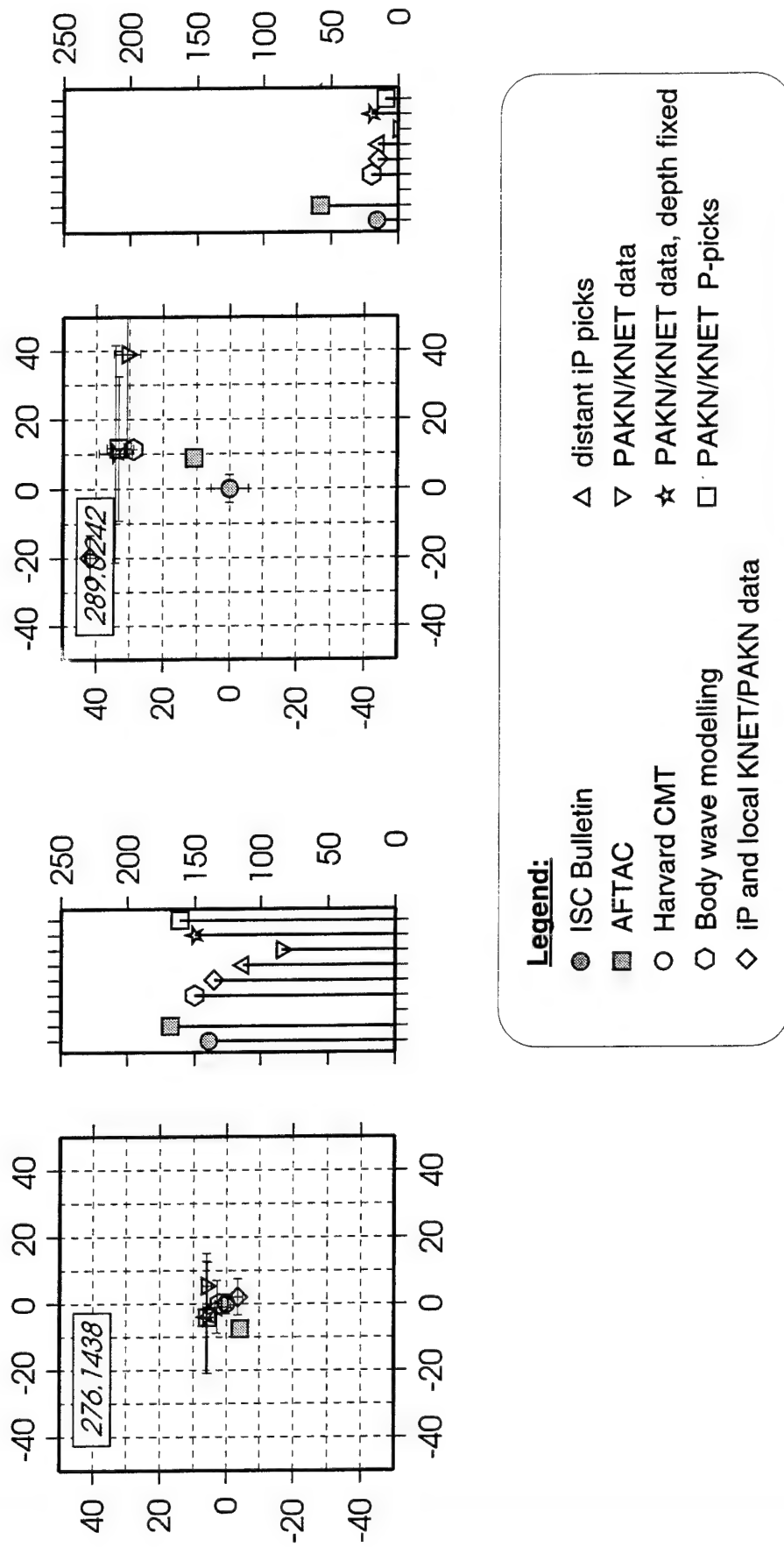
Figure 54 Epicentral location relative to the ISC Bulletin location (left panel) and depths (right panel) determined using the various methods and/or datasets described in the text. Distances and depth scales are in kilometers. Note that the ISC locations are used for the body-wave modelling.
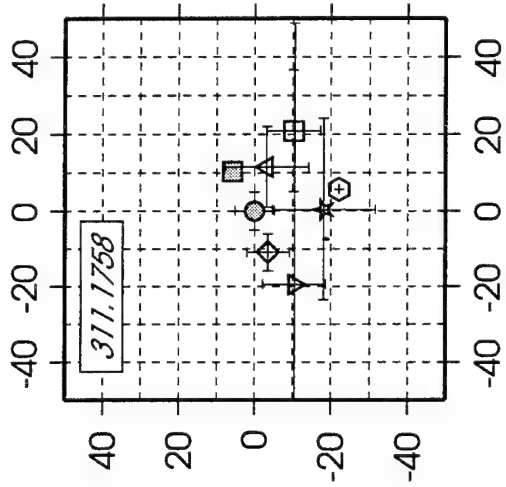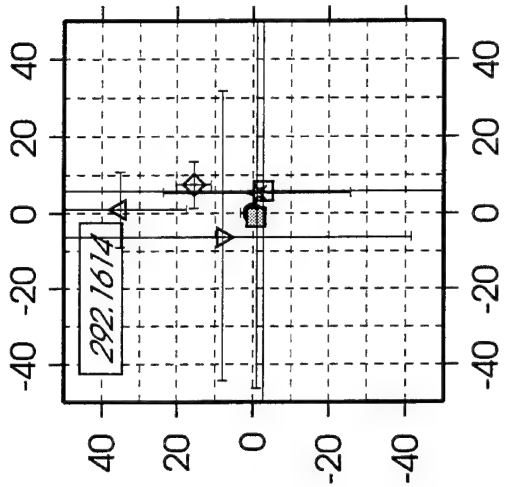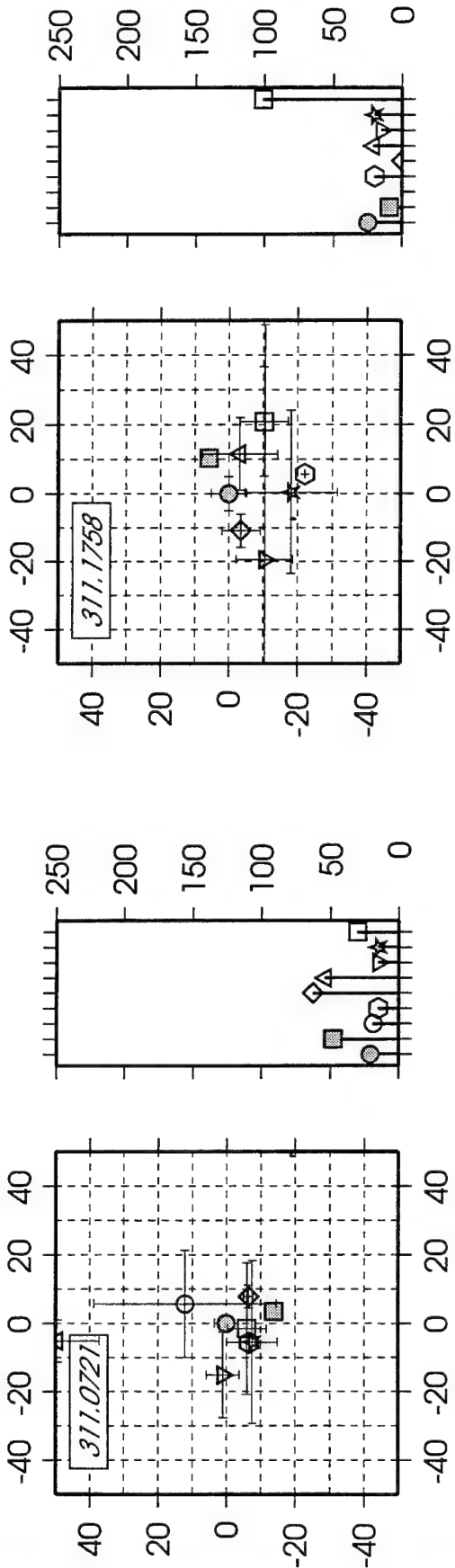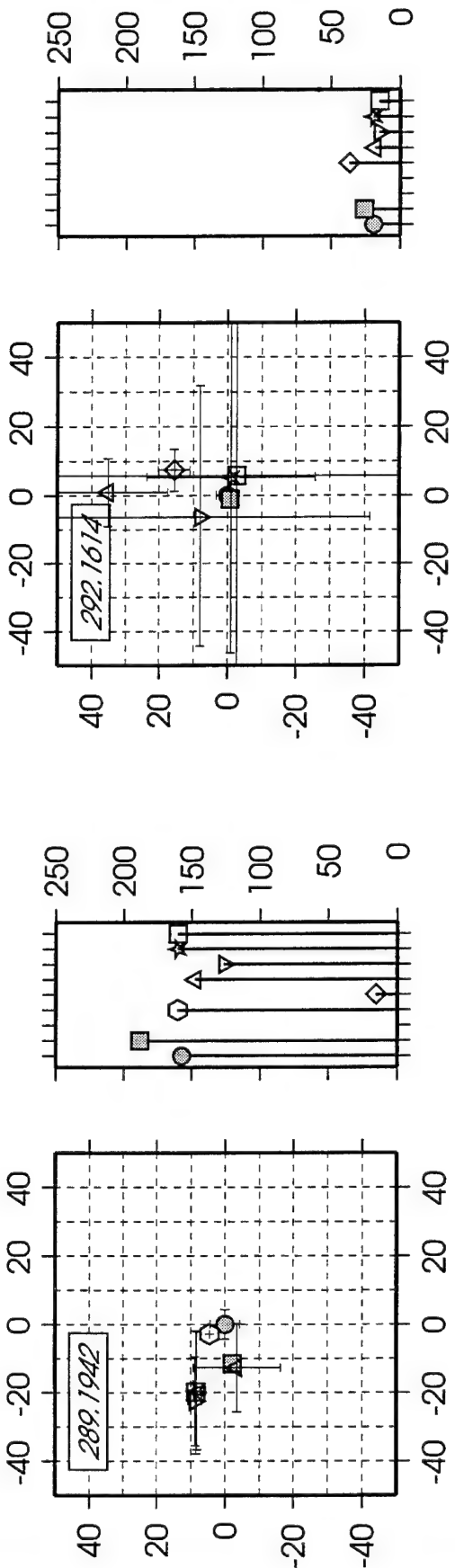
Legend:
- ● ISC Bulletin
- ■ AFTAC
- ○ Harvard CMT
- ◇ Body wave modelling
- ◇ iP and local KNET/PAKN data
- △ distant iP picks
- ▽ PAKN/KNET data
- ★ PAKN/KNET data, depth fixed
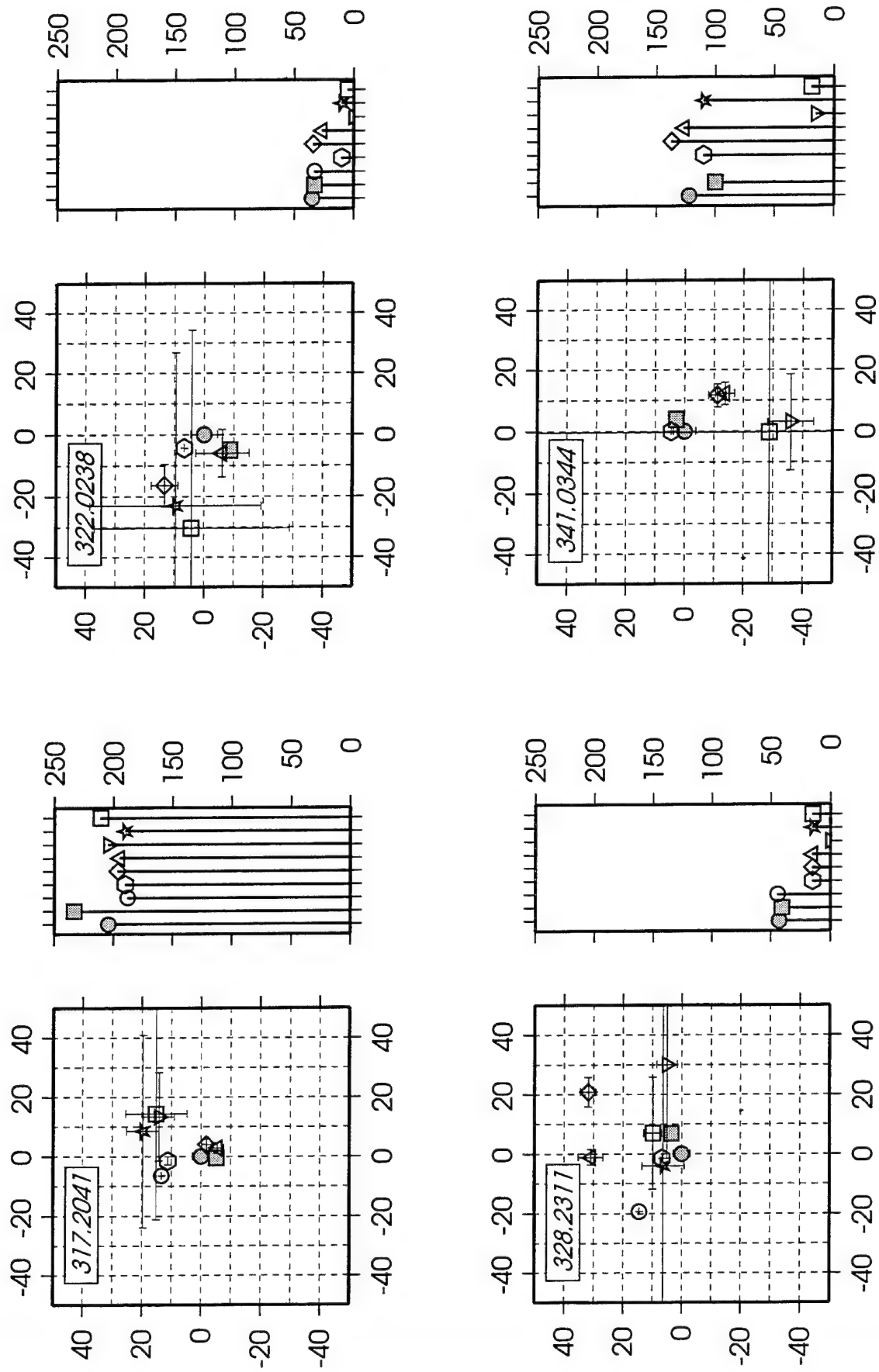- □ PAKN/KNET P-picks

Figure 54 (cont.)

95

Figure 54 (cont.)

96

at distances larger than 1000 km from the epicenter, and the locations obtained from this inversion are referred to as "distant P" locations in Table 9.

First, we shall briefly comment on the quality and characteristics of the ISC locations, which may well be appropriate for the AFTAC locations as well. The ISC locations rely heavily on the identification and timing of P picks, and sometimes pP for depth control. These picks are sometimes further classified as emergent and impulsive. Obviously, the emergent picks are prone to timing errors since it is difficult to pick the exact beginning of such phases. Furthermore, at triplication distances, Δ = 15-30 degrees for P waves, there is a significant possibility of misidentification of the P wave with its triplication. Also, at these distances as well as distances shorter than 15 degrees, theoretical travel-times can be strongly influenced by crustal and upper mantle heterogeneity. This is obvious from a comparison of travel-time residuals for regional and teleseismic distances for the larger events. Residuals for local and regional distances are on the order of 5 sec and can be as high as 10 sec, whereas the teleseismic residuals are on the order of .5 sec., and rarely exceed 1 sec.

For the Hindu-Kush area, there is an additional problem with the azimuthal coverage. In the distance range of 35 to 55 degrees, there are very few stations outside Europe reporting. For larger events, like event 328.2311 (M_w = 5.1), this is not a problem since there are many impulsive P picks both locally as well as at teleseismic distances with a good azimuthal distribution. For smaller events however, like events 289.0242 and 311.1758, these problems are quite serious. At distances larger than 30 degrees, there are few P-picks, 37 and 17 respectively, and about three quarter of these picks are listed as emergent, and only about 5 picks are impulsive. Furthermore, only two or three of the teleseismic picks are from non-European azimuths. Therefore, the solutions rely heavily on local and regional (0-15 degrees) and triplication (15-30 degrees) distances so that effects of laterally inhomogeneous structure or, even just the fact that the local structure does not resemble the model used by the ISC, gives rise to poor locations. In order to test the reliability of the locations using only the more distant P picks from the ISC bulletin we performed an inversion with these phases only using the IASPEI model. These results show that in some cases the locations are quite close to the ISC locations but in other cases are more than 30 km away from both the ISC or our locally obtained locations.

97

Using the locally recorded broadband data gives us some real advantages over the teleseismic location. For the smaller events, the P arrivals are still clearly and distinctly visible; and since the data are digitally recorded, they can be picked very accurately. When picks from both the KNET and PAKN arrays are available, or even when only station FRU is available in lieu of KNET, our hypocenter locations, as well as depths, are usually within 20 km of the ISC and AFTAC locations and in many cases for the larger events the difference is on the order of 5 km. In some cases where the difference with the ISC location is larger, for example events 289.0242 and 311.1758, we suspect that the ISC and AFTAC locations are poorly constrained, as discussed earlier. We conclude that using local good quality P picks from two nearby arrays, even when one of the arrays has only one station reporting, is sufficient for good epicenter determinations. Even for smaller earthquakes ($M_W < 4.2$), such a location scheme can give better results than the methods used by the ISC.

Adding S picks to the data set does not produce significant improvement in the solutions and for the deeper events they actually give worse results, especially for depths (for example, see Table 9 for events 276.1438, 289.1942). This is probably caused by misidentification of the sPmP phase for an S phase (see Section 3).

For event 341.0344 neither the KNET data nor a P-pick from station FRU was available and it is clear that the location based on the PAKN data alone is unreliable. If we fix the depth, the location moves further away from the other locations. If we do not constrain the depth, we obtain a reasonable epicenter, but the depth moves to 15 km from 110 km. This very strong tradeoff between depth and hypocenter is not surprising if only one array, effectively one station, is being used.

Harvard CMT solutions (Dziewonski and Salganik, 1992) were available for four of the events, namely 311.0721, 317.2041, 322.0238 and 328.2311. Of these events, the first two events had centroid depths consistent with the depths from the local networks, and the other two had centroid depths significantly greater than our depths, but close to those of ISC and AFTAC.

Finally, we found that the locations obtained using waveform modeling of regional data are better, especially for the smaller shallow events. Further relocating the regional solutions by first finding the depth based on minimizing error between the data and synthetic misfit through iteration over several depths, and then fixing the depth and minimizing the travel-time residuals iterating over the (X,Y) coordinates produced better locations for all the events. We discuss this work in the next section but intend to point out that while for the large events and the small deep events there is no scatter in (X,Y) coordinates, the scatter was quite significant for the shallow small events (Mw < 5.0).

6. Discussion

Attempts at calibrating teleseismic paths and regional paths prove quite difficult. Many times only ISC travel time picks are available. While these are quite valuable in refining locations, they can be misleading as one changes event magnitude. For example, P_n can be easily missed for small events. Working with AFTAC data is difficult in that to calibrate stations, m_b bias for example, requires the study of many events and the relationship of each station behavior relative to global networks. For example, we find that GERESS amplitudes are 20 times larger than those on the ASP array. Of course, these excellent recordings can be used in determining depth phases but this does not look very promising for this complex region. Thus, we plan a rather restricted data analysis relying entirely on local data.

In particular, we want to ascertain what we can achieve using the PAKN array, when operating, by using the broadband stations NIL and AAK to retrieve source information. We can address this situation by performing the location and estimation of seismic characteristics of the 10 events discussed in detail by allowing SBRA to be the proxy for NIL. Note that these two station locations are quite close (see Table 7). Thus, we will repeat the above analysis for the two stations SBRA and AAK assuming the ISC locations as a starting model and compare our results against the array results. Since the Tibetan model was used in determining the mechanisms discussed earlier, we will use this model in this demonstration. The results are given for the crustal events in Figure 55 and deep events in Figure 56. While some events are not well constrained, for example event 311.1758, most events are well determined by using the two
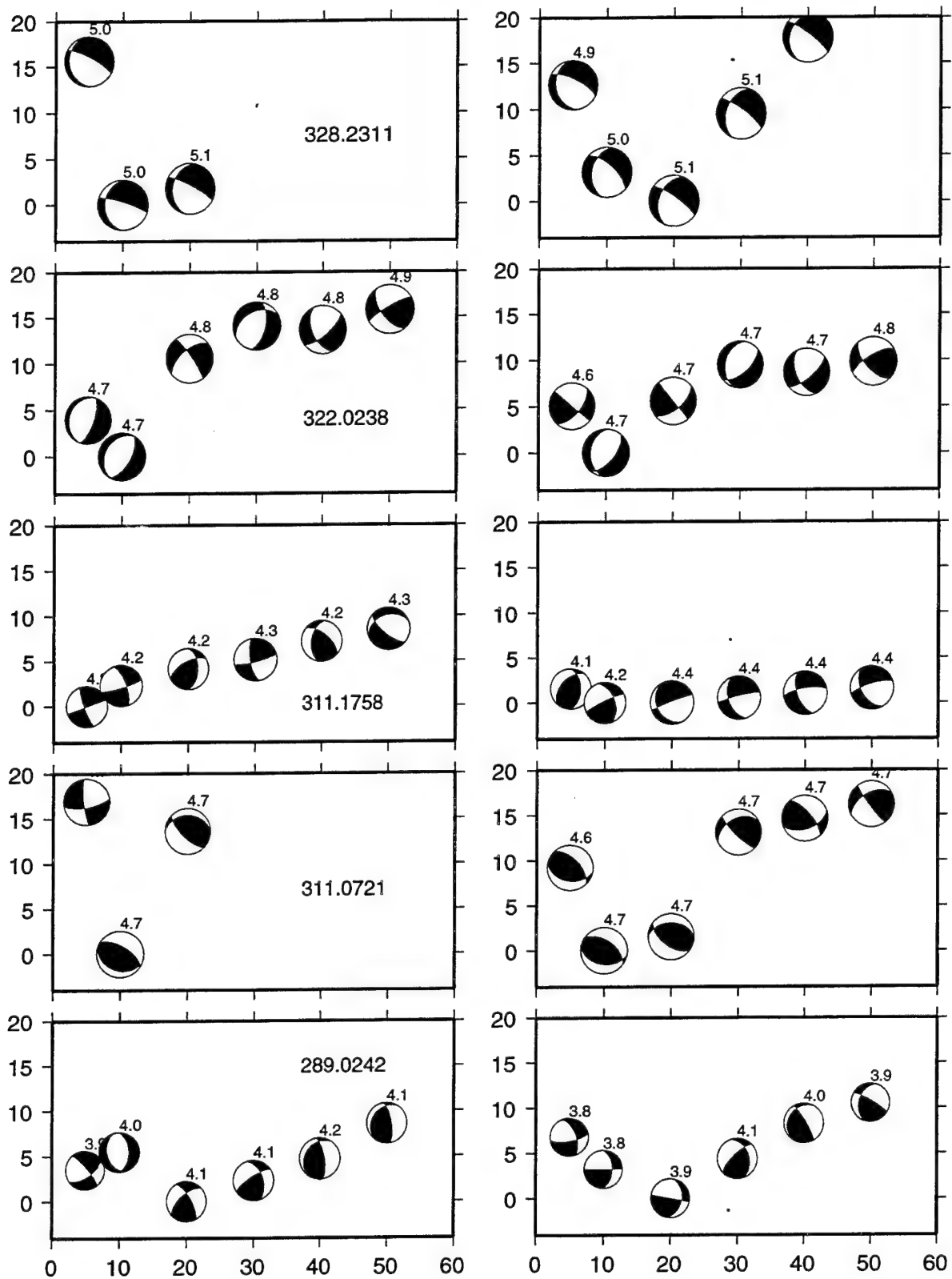
Figure 55 Comparison of misfit errors for the crustal events with the two station results on the left against the full arrays on the right.
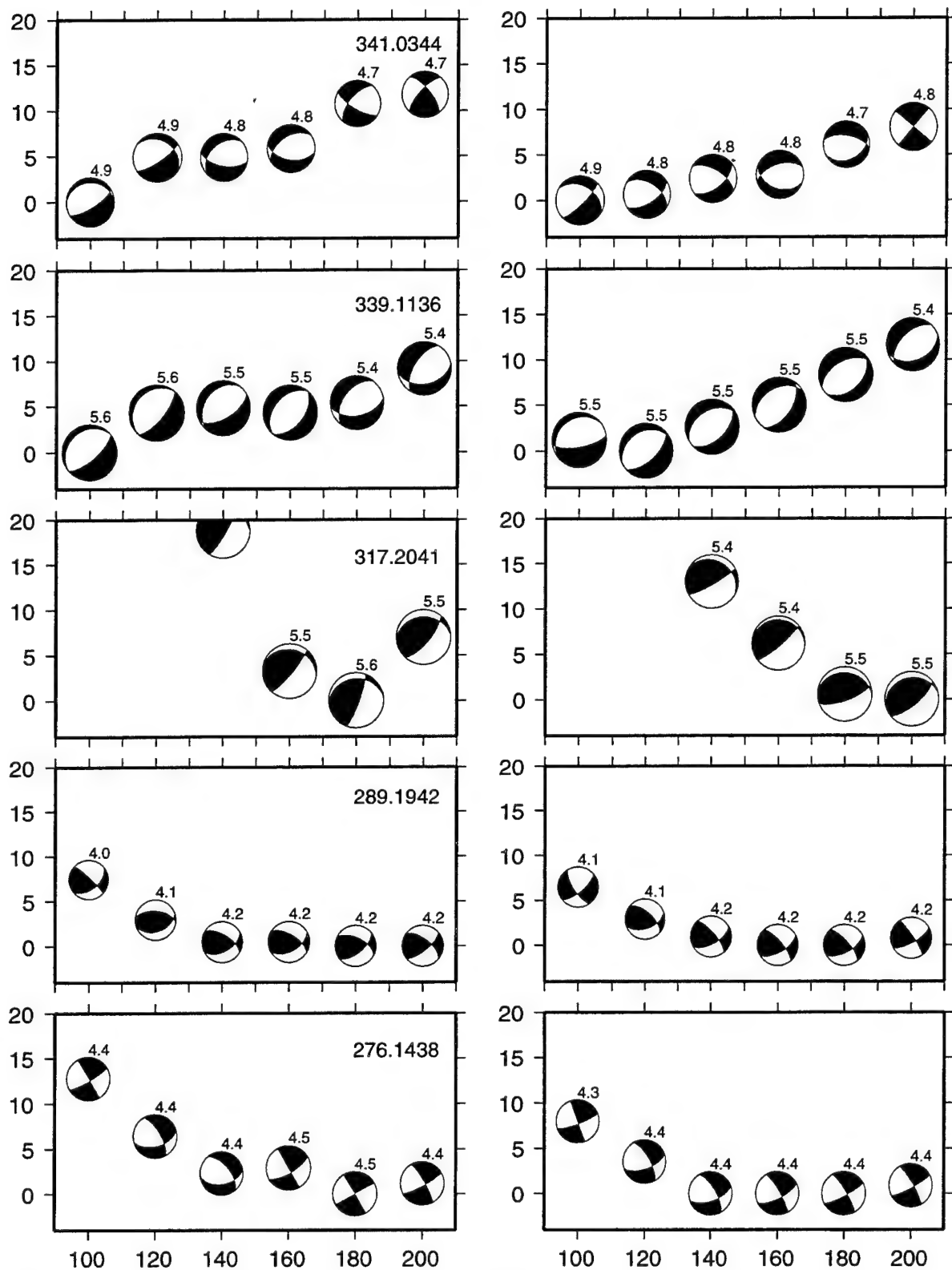
Figure 56   Comparison of misfit errors for the deep events with the two station results on the left against the arrays on the right.

stations. Figure 57 displays the depth resolution comparison where only event 311.1758 causes difficulties.

The relocations using the two arrays vs. the two stations are given in Tables 10 and 11, respectively. The results are very similar except for the problematic event 311.1758. Comparing this table with that derived by the full arrays (Table 6) we find excellent agreement. Note the same two events 289.0242 (M_w = 4.0) and 311.1758 (M_w = 4.4) moved relative to the ISC locations. Small, shallow events cause problems in ISC locations as discussed earlier.

Just as two-station source inversion estimates yield results compatible with estimates by the full network, so too is it possible to obtain useful source and location information from one station (3 component) observations. Currently TERRAscope has a real time, automated source retrieval system at each station to locate and estimate the source parameter for incoming events. An event trigger detects the P-wave after which the three-component data are searched for the S-wave. The horizontal records are rotated to the best separated SV-SH component system to obtain the back azimuth.

This same online procedure will be modified for use in the IDC monitoring system. Besides yielding location information, once the distance is found, regional magnitudes, M_L, m_b (m_b (L_g)), and M_S, can be calculated and the energy ratio discriminant, as well as others requiring distance information, can be applied. Should the event be determined an outlier, i.e. fall outside the earthquake population, then it will be analyzed by the source inversion grid search for mechanism and depth. Events for which a good-fitting earthquake mechanism and a deep source depth are obtained then can be ruled out as possible explosions.

This procedure is already fairly well developed and we will apply it to the current data sets in order to analyze its performance by testing it against the above 10 master events. It will then be ready for incorporation into the IDC monitoring system. Thus, we plan to extend this sparse network source retrieval method to other GSETT-3 stations further to the west in the Middle East and into North Africa and portions of the Mediterranean.
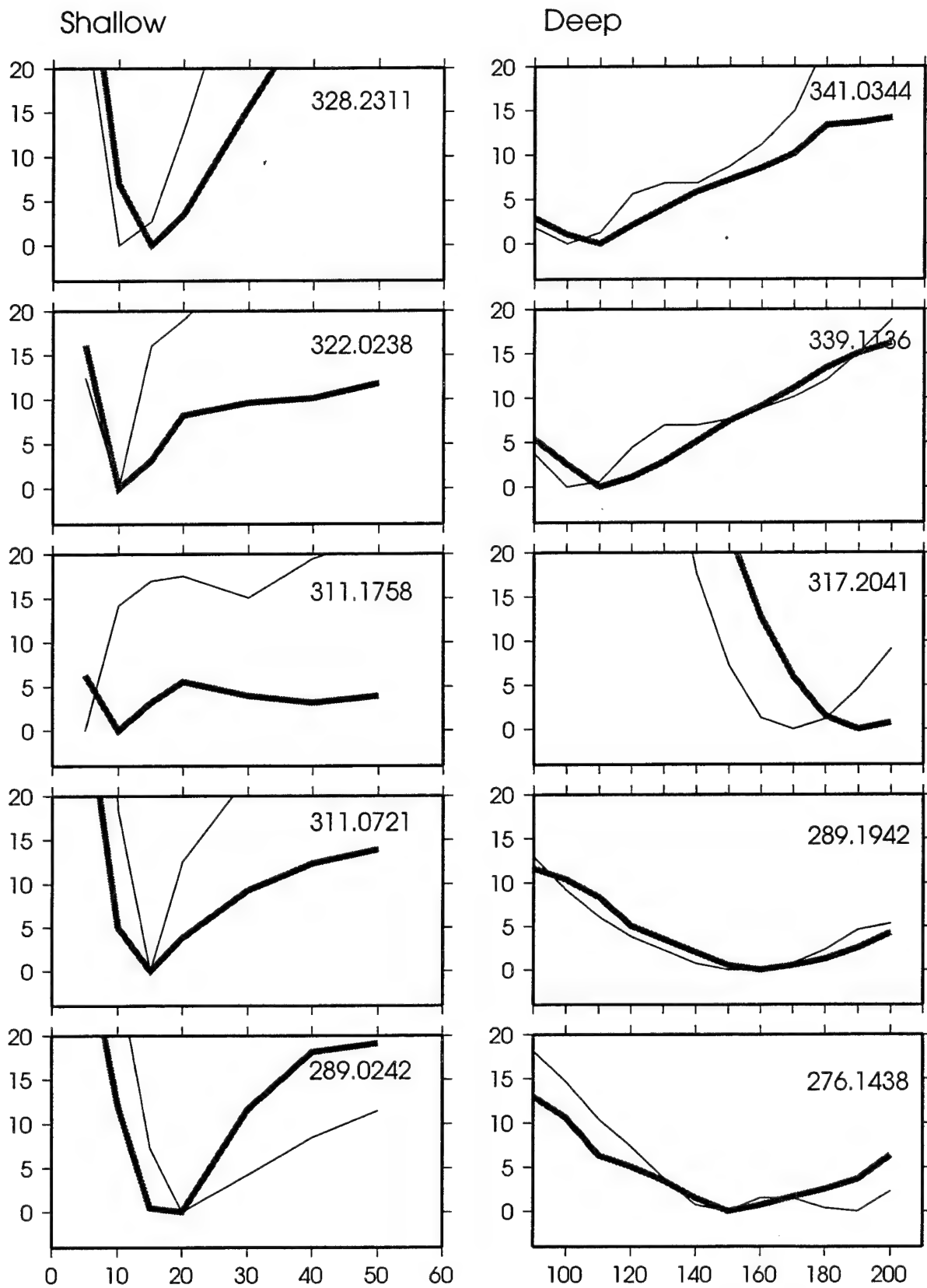
Figure 57   Comparison of two-station against arrays for the best source depth estimate. The thick grey line shows the results for the arrays, the thin black line shows the results using two stations.

Table 10: Relocation Result Using PAKN and KNET Arrays

Event	Δt_0	Lat.	Long.	Δx	Az.	h	ISC h
276.1438	0.41	38.10	73.12	2	0	150	139.0
289.0242	1.32	39.50	72.96	32	25	20	16.0
289.1942	-0.36	38.24	74.40	5	321	160	157.0
311.0721	-1.75	41.03	72.42	9	225	15	21.0
311.1758	-2.60	34.67	69.23	23	161	20	25.0
317.2041	-0.57	36.55	70.85	11	350	190	204.0
322.0238	-4.35	33.89	67.47	8	320	10	35.0
328.2311	-3.16	38.63	72.63	6	345	15	43.0
339.1136	0.10	37.85	72.21	6	0	110	114.0
341.0344	-0.45	37.83	72.19	4	0	110	122.0

Table 11: Relocation Result Using Station AAK and SBRA

Event	Δt_0	Lat.	Long.	Δx	Az.	h	ISC h
276.1438	0.62	38.08	73.20	7	89	150	139.0
289.0242	1.31	39.50	72.86	29	10	20	16.0
289.1942	-0.00	38.22	74.44	2	0	150	157.0
311.0721	-1.12	40.99	72.50	11	180	15	21.0
311.1758	-4.51	34.63	69.19	26	172	5	25.0
317.2041	-0.40	36.57	70.81	14	338	170	204.0
322.0238	-4.16	33.91	67.49	9	337	10	35.0
328.2311	-2.30	38.61	72.71	6	49	15	43.0
339.1136	0.04	37.83	72.25	5	38	110	114.0
341.0344	-0.20	37.85	72.21	6	14	100	122.0

The resolution of source depth is not only useful as a stand alone discriminant, but also has been found to be necessary information for sorting out outliers from the crustal earthquake population. Employing the integrated short-period:long-period energy ratio discriminant, with this depth information, this discriminant appears to work on a global basis with the exception of regions with the severest of scattering or "blocking" or attenuation. We will expand upon the comparative data set by analyzing events further to the west in the Middle East, into North Africa, and add into the repertoire of tested tectonic provinces events traversing the Mediterranean Sea.

7. Conclusions

We have established a successful basis for locating and discriminating seismic events in the Hindu-Kush region using regional seismograms recorded at the new broadband station at NIL in Pakistan, a GSETT-3 β station, and at the IRIS station AAK in Kyrgyzstan. This has involved developing a 1-D model for obtaining source parameters through waveform inversion. The mechanisms obtained are similar to the CMT solutions, although we have gone to lower magnitudes and have obtained more accurate depth estimates. Our source depth location study has been comprehensive, making use of local travel-time data, analysis of regional broadband waveforms with respect to depth phases and the strength of P_{nl} waves relative to surface waves, and analysis of teleseismic depth phases. The method that we have developed is highly effective for events with magnitude down to M_w of 4.0 which are not always clearly recorded at teleseismic and far-regional distances, especially their depth phases.

While the large events ($M_w > 5$) can be observed globally and located reasonably well using teleseismic data, problems start for events at the lower margin of this magnitude threshold. Locating these events is difficult because the P_n waves, which are often the first arrivals, are below the noise level. While the short-period teleseismic arrays are useful in detecting small events using the beam forming technique, in most cases they do not provide good depth phases for the Hindu-Kush events, except for the Alice Springs array in Australia which can be very useful.

By locating events with a source inversion scheme using regional seismograms from all stations of PAKN and KNET networks, and comparing their source solutions to those obtained using only two stations, SBRA (NIL) and AAK, we have demonstrated that the latter also can provide accurate hypocentral information for events as small as $M_w = 4$ in the Hindu-Kush region. This regional modeling takes advantage of the timing separation between sPmP and P for the deep events and the ratio of P_{nl} to the surface waves for the shallow events in constraining the source depth. We have successfully tested the automation of this process with interactive software for 10 master events ranging from shallow to deep and small (M_W 4.0) to large.

Our preferred short-period:long-period energy ratio discriminant produces an earthquake population similar to that obtained from the TERRAscope data (for the southwestern U.S.) for crustal earthquakes, but gives consistently high ratios when applied to deep earthquakes. These high ratios are similar to those estimated for NTS explosions (Woods and Helmberger, 1996) and so these events will probably look like explosions on the discrimination chart. The ratios are high because for deep events, the surface waves are weak relative to the body waves. Therefore, in regions of CTBT interest such as the Middle East, including the Hindu-Kush region, where deep and intermediate depth earthquakes are quite common (see Figure 3), the ability to determine the source depth becomes crucial for effective discrimination. Any event that plots outside of the crustal earthquake population, but cannot be proven to be deep, could be an explosion, thus the importance of the above regional modeling capabilities.

References

Barazangi, M., D. Seber, M. Vallve, E. Fielding and B. Isacks (1995). A geological and geophysical information system for Eurasia, the Middle East and North Africa, digital data base development for the Middle East and North Africa, PL-TR-94-2092, *Scientific Rept. 1 to Phillips Laboratory*, Hanscom AFB, MA, 82p., ADA297018.

Baumgardt, D. (1995). Case studies of seismic discrimination problems and regional discriminant, PL-TR-95-2106, *Final Rept. to Phillips Laboratory*, Hanscom AFB, MA. 73p.

Baumgardt, D. and. Z. Der (1994). Investigation of the transportability of the P/S ratio discriminant to different tectonic regions. PL-TR-94-2299, *Scientific Rept #1 to Phillips Laboratory*, Hanscom AFB, MA, 66p., ADA292944.

Dreger, D. and D.V. Helmberger (1993), Determination of source parameters at regional distances with three-component sparse network data, *J. Geophys. Res.*, **98**, 8107-8125.

Dziewonski, A.M. and D.L. Anderson (1983). Preliminary reference earth model, *Phys. Earth Planet. Inter.*, **25**, 297-356.

Dziewonski, A.M. and E.G. Salganik (1992). Centroid-Moment Tensor Solutions for October-December. *Physics of the Earth and Planetary Interiors*, **80**, 89-103.

Fan, G.W. and T.C. Wallace (1991). The determination of source parameter for small earthquakes from a single very broadband seismic station, *Geophys. Res. Lett.*, **18**, 1385-1388.

Fan, G.W., S.L. Beck and T.C. Wallace (1994). The seismic source parameters of the 1991 Costa Rica Aftershock sequence: Evidence for a transcurrent plate boundary, *J. Geophys. Res.*, **98**, 15,759-15,778.

Fielding, Eric J., B.L. Isacks and M. Barazangi (1992). A geological and geophysical information system for Eurasia, F29601-91-K-DB08, *Semiannual Tech. Rept. #1 to Phillips Laboratory*, Kirtland AFB, NM, 18p.

Fisk, M.D., H.L. Gray and G.D. McCartor (1994). Preliminary assessment of seismic CTBT/NPT monitoring capability, PL-TR-94-2300, *Scientific Rept. #1 to Phillips Laboratory*, Hanscom AFB, MA, 39p., ADA293188.

Helmberger, D.V. (1983). Theory and application of synthetic seismograms, Earthquakes: Observation, Theory and Interpretation, *LXXXV Corso Soc. Italiana di Fisica*, Bologna, Italy, 174-222.

Helmberger, D.V. and X. Song (1995). Development of regional discriminants, *Proceedings of 17th Seismic Research Symp.* sponsored by PL/AFOSR/DOE, 58-67, PL-TR-95-2108.ADA310037

Kennett, B.L.N. and E.R. Engdahl (1991). Traveltimes for global earthquake location and phase identification, *Geophys. J. Int.*, **105**, 429-465.

Langston, C. and D.V. Helmberger (1975). A procedure for modeling shallow dislocation sources, *Geophys. J. R. Soc.*, **42**, 117-130.

Lay, T., T.C. Wallace and D.V. Helmberger (1984). The effects of tectonic release on short-period P waves from NTS explosions, *Bull. Seis. Soc. Am.*, **74**, 819-842.

LeFevre, L.V. and D.V. Helmberger (1989). Upper mantle P velocity structure of the Canadian shield, *J. Geophys. Res.*, **94**, 17,749-17,765.

Lienert, B.R., Havskov, J. (1995). A computer program for locating earthquakes both locally and globally. *Seismological Research Letters*, **66**, 5, 26-36.

Marshall, P.D. and P.W. Basham (1972). Discrimination Between Earthquakes and Underground Explosions Employing an Improved M_S Scale, *Geophys. J. R. Astr. Soc.*, **28**, 431-458.

McNamara, D.E., T.J. Owens and W.R. Walter (1995). Observations of Regional Phase Propagation Across the Tibetan Plateau, *J. Geophys. Res.*, **100**, 22,215-22,229.

Owens, T.J., G.E. Randall, F.T. Wu and R.S. Zeng (1993). PASSCAL instrument performance during the Tibetan Plateau passive seismic experiment, *Bull. Seis. Soc. Am.*, **83**, 1959-1970.

Patton, H.J. (1980). Reference point method for determining the source and path effects of surface waves, *J. Geophys. Res.*, **85**, 821-848.

Pavlis, G.L. and H. Mahdi (1995). The spatial stability of Rayleigh wave amplitudes and path dependent propagation characteristics of central Asia, *Proceedings of 17th Seismic Research Symp.* sponsored by PL/AFOSR/DOE, 291-298, PL-TR-95-2108. ADA310037

Ritsema, J. and T. Lay (1993). Rapid source mechanism determination of large $M_W > 5$ earthquakes in the western United States, *Geophys. Res. Lett.*, **20**, 1611-1614.

Roecker, S.W., T.M. Sabitova, L.P. Vinnik, Y.A., Burmakov, M.I. Golyanov, R. Mamatkanova and L. Munirova (1993). Three-dimensional elastic wave structure of the western and central Tien Shan. *J. Geoph. Res.*, **98**, 15,779-15,795.

Saikia, C.K., D.V. Helmberger, L and L. J. Burdick. (1992). Regional wave propagation and high-frequency/low-frequency energy level discriminant, *Proceedings of 14th Seismic Research Symp.* sponsored by PL/DARPA, 351-360, PL-TR-92-2210, ADA256711.

Sandvol, E., J. Ni and T. Hearns (1994). Seismic azimuthal anisotropy beneath the Pakistan Himalaya, *Geophys. Res. Lett.*, **21**, No 15., 1635-1638.

Taylor, S.R., M.D. Denny, E.S. Vergino and R.E. Glaser (1989). Regional discrimination between NTS explosions and western United States earthquakes, *Bull. Seis. Soc. Am.*, **79**, 1142-1176.

Thio, H.K. and H. Kanamori (1995). Moment-tensor inversion for local earthquakes using surface waves recorded at TERRAscope, *Bull. Seis. Soc. Am.*, **85**, 1021-2038.

Wallace, T.C. and D.V. Helmberger (1982). Determination of seismic parameters of moderate-size earthquake from regional waveforms, *Phys. Earth. Planet. Inter.*, **30**, 185-196.

Walter, W.R. (1993). Source parameters of the June 29 Little Skull Mountain earthquake from complete regional waveforms at a single station, *Geophys. Res. Lett.*, **20**, 403-406.

Walter, W.R., K.M. Mayeda and H.J. Patton (1995). Phase and Spectral Ratio Discrimination between NTS Earthquakes and Explosions. Part I: Empirical Observations, *Bull. Seis. Soc. Am.*, **85**, 1050-1067.

Woods, B.B. and C.K. Saikia (1995). The Portability of Some Regional Seismic Discriminants and Related Broadband Waveform Modeling, *Proceedings of 17th Seismic Research. Symp.* sponsored by PL/DARPA, 138-151, PL-TR-95-2108. ADA310037

Woods, B.B. and D.V. Helmberger (1996). Regional Seismic Discriminants using Wavetrain Energy Ratios, *Bull. Seis. Soc. Am.*, (submitted)

Zhao, L-S. and D.V. Helmberger (1991) Geophysical implications from relocations of Tibetan earthquakes: Hot lithosphere, *Geophys. Res. Lett.*, **18**, 2205-2208.

Zhao, L-S. and D.V. Helmberger (1993). Source retrieval from broadband regional seismograms; Hindu Kush region., *Phys. Earth. Planet. Inter.*, **78**, 69-95.

Zhao, L-S. and D.V. Helmberger (1994). Source estimation from broadband regional seismograms, *Bull. Seis. Soc. Am.*, **84**, 92-104.

Zhao, L-S. and D.V. Helmberger (1995). Regional moment, energy level, and new discriminants, *Pure. Appl. Geophys.*, Vol **146**, 1168-1192.

Zhu, L. and D.V. Helmberger (1995). Focal mechanism determination and propagation characteristics of high frequency S- waves on the Tibetan Plateau, *Proceedings of 17th Seismic Research Symp.* sponsored by PL/AFOSR/DOE, 702-710, PL-TR-95-2108. ADA310037

Zhu, L., T.J. Owens and G.E. Randall (1995). Lateral variation in crustal structure of the northern Tibetan plateau, *Bull. Seis. Soc. Am.*, **85**, 1531-1540.

Zhu, L. and D.V. Helmberger (1996). Advancement of source retrieval from broadband regional seismograms, *Bull. Seis. Soc. Am.*, (submitted)
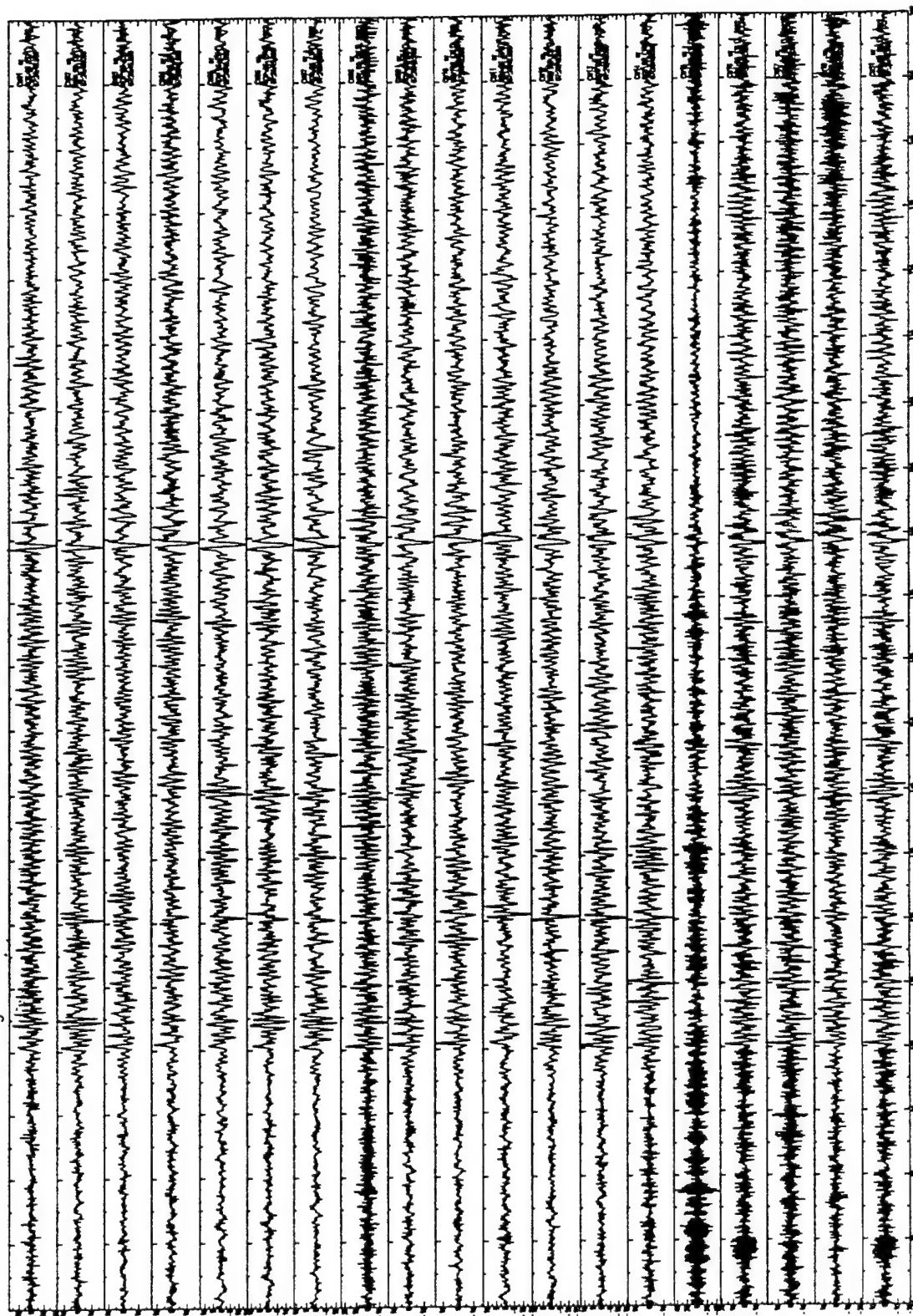
APPENDIX - I

Examples of seismograms recorded by short-period arrays at different stations.   Each figure is accompanied by array name (for example ASP for Alice Springs), event id in julian day, origin time, depth from the PDE monthly bulletin, and magnitude.
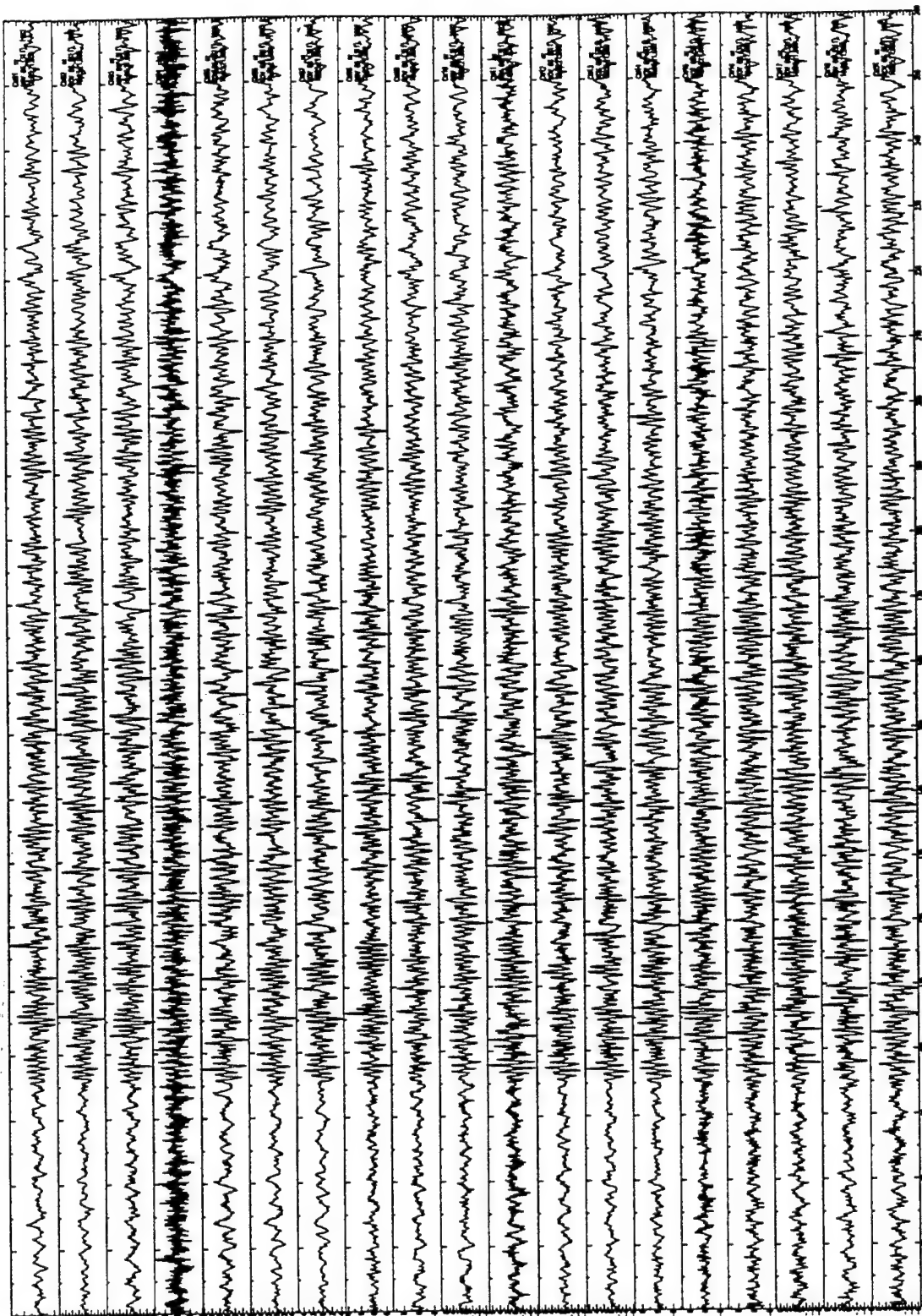
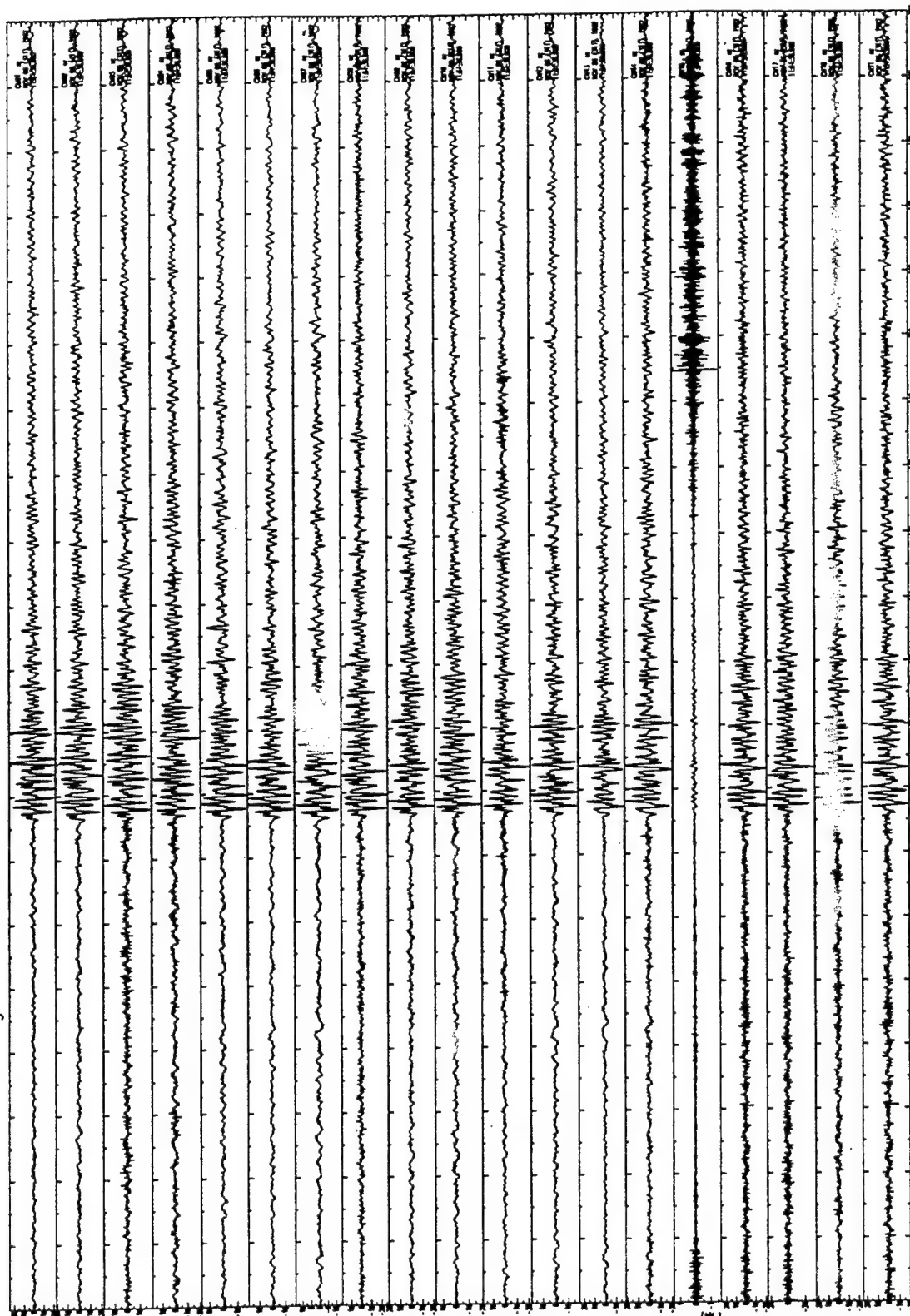Chiang Mai — JD292   Oct 18. 1992   16h 14m 45.5s   h=19.0km   mb=5.1
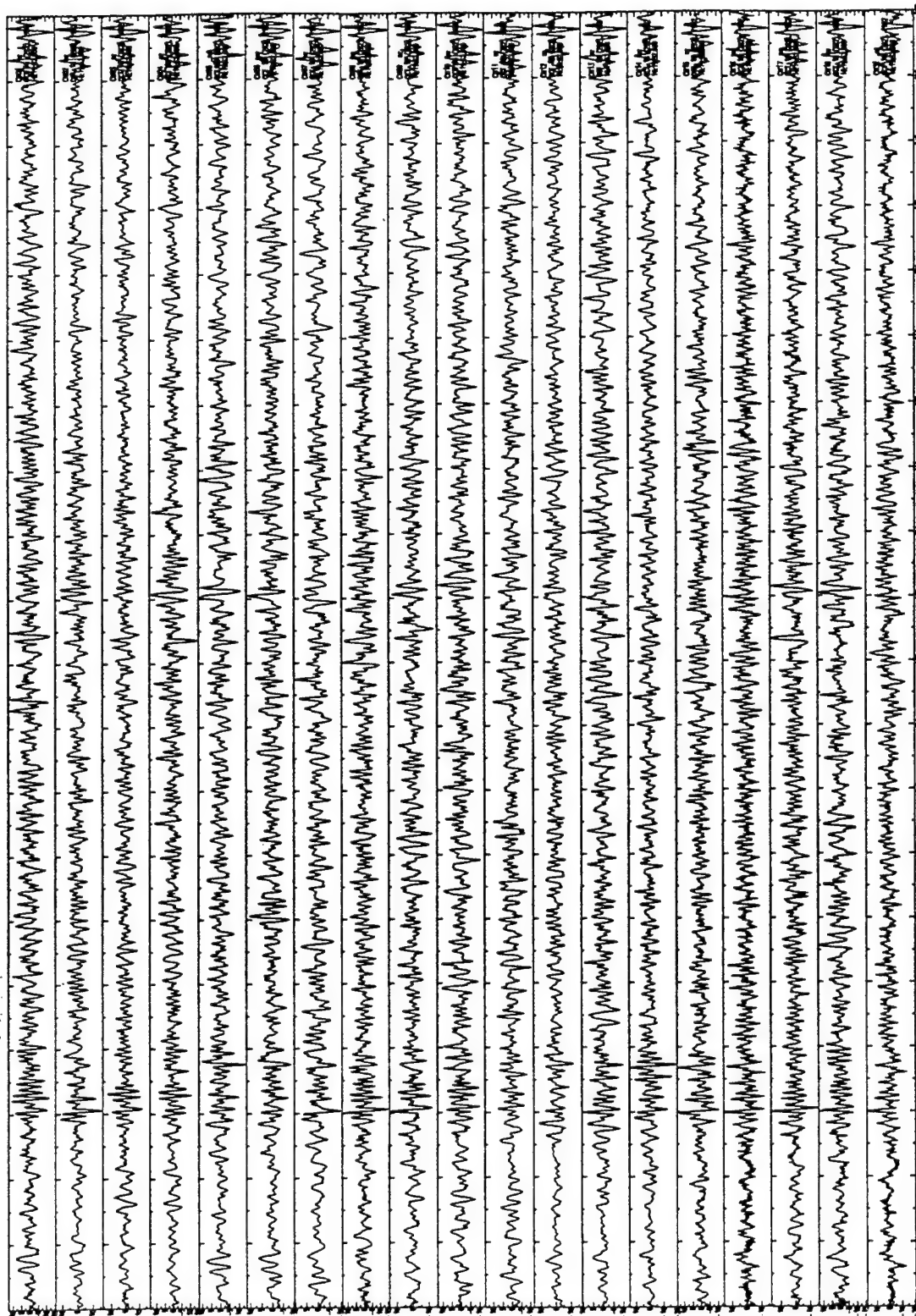
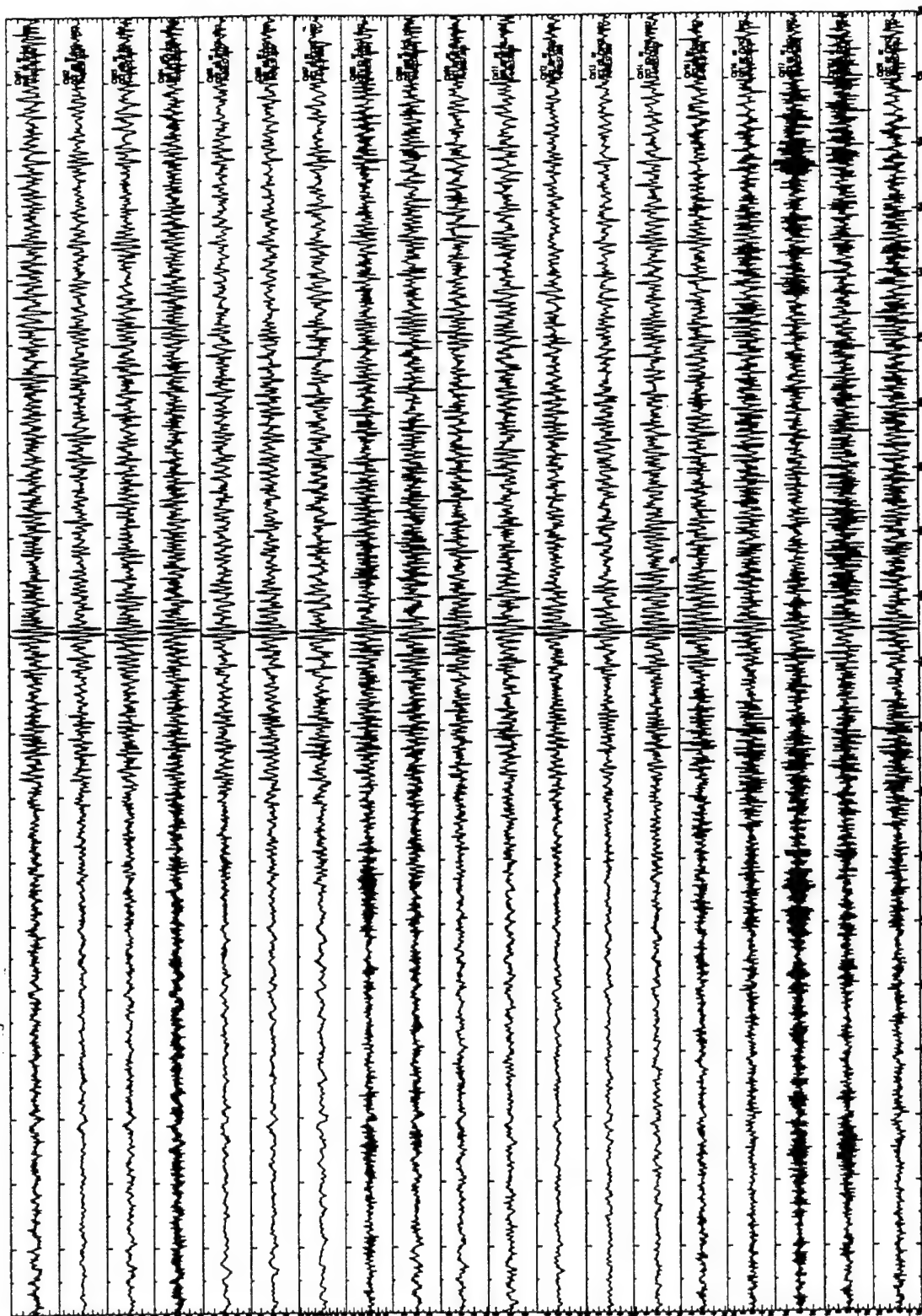Chiang Mai - JD311 Nov 6, 1992 07h 21m 57.8s h=40.0Km Mb=5.1

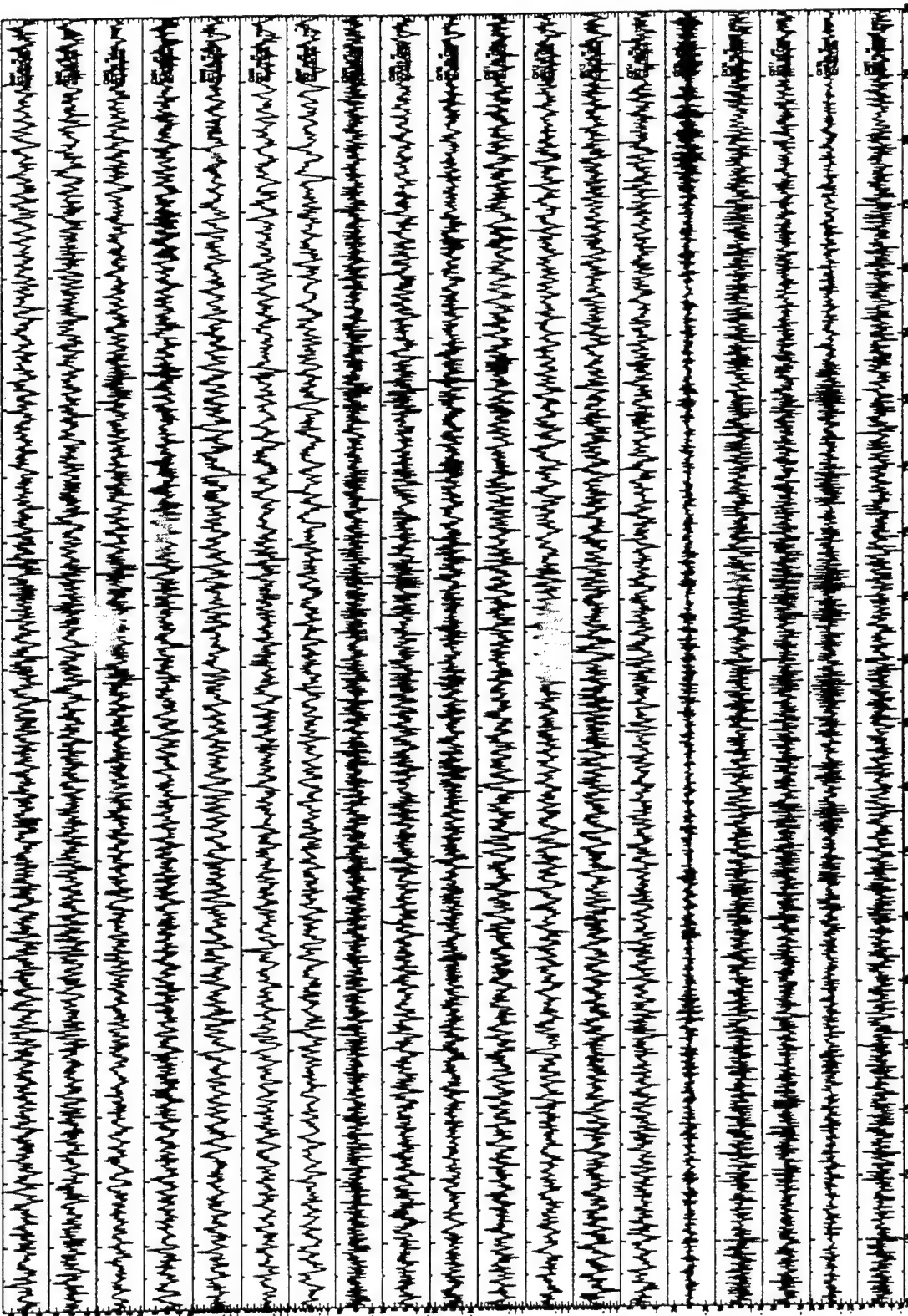Chiang Mai – JD311 Nov 6, 1992 17h 58m 38.0s h=33.0km Mb=4.5

Chiang Mai – JD311 Nov 6, 1992 11h 47m 42.9s h=12.0Km mb=4.6

Chiang Mai – JD276   Oct 2, 1992   14h 38m 44.0s   h=118.0Km   Mb=4.9

117

Chiang Mai - JD289   Oct 15, 1992   02h 42m 06.3s   h=16.0Km   Mb=4.6

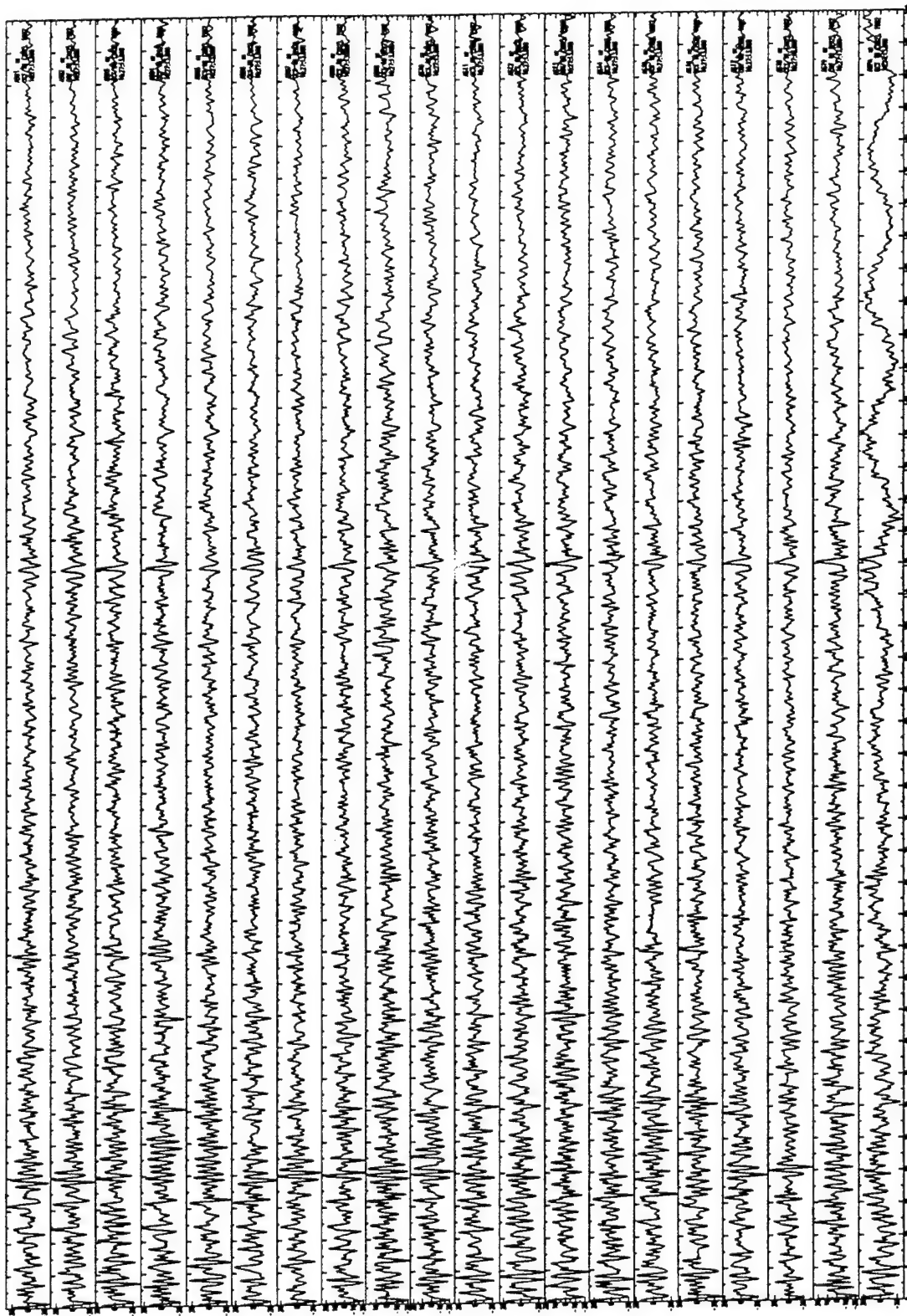Alice Spring – JD311 Nov 6, 92   17h58m 38.0s   h=33.0Km   M=4.5
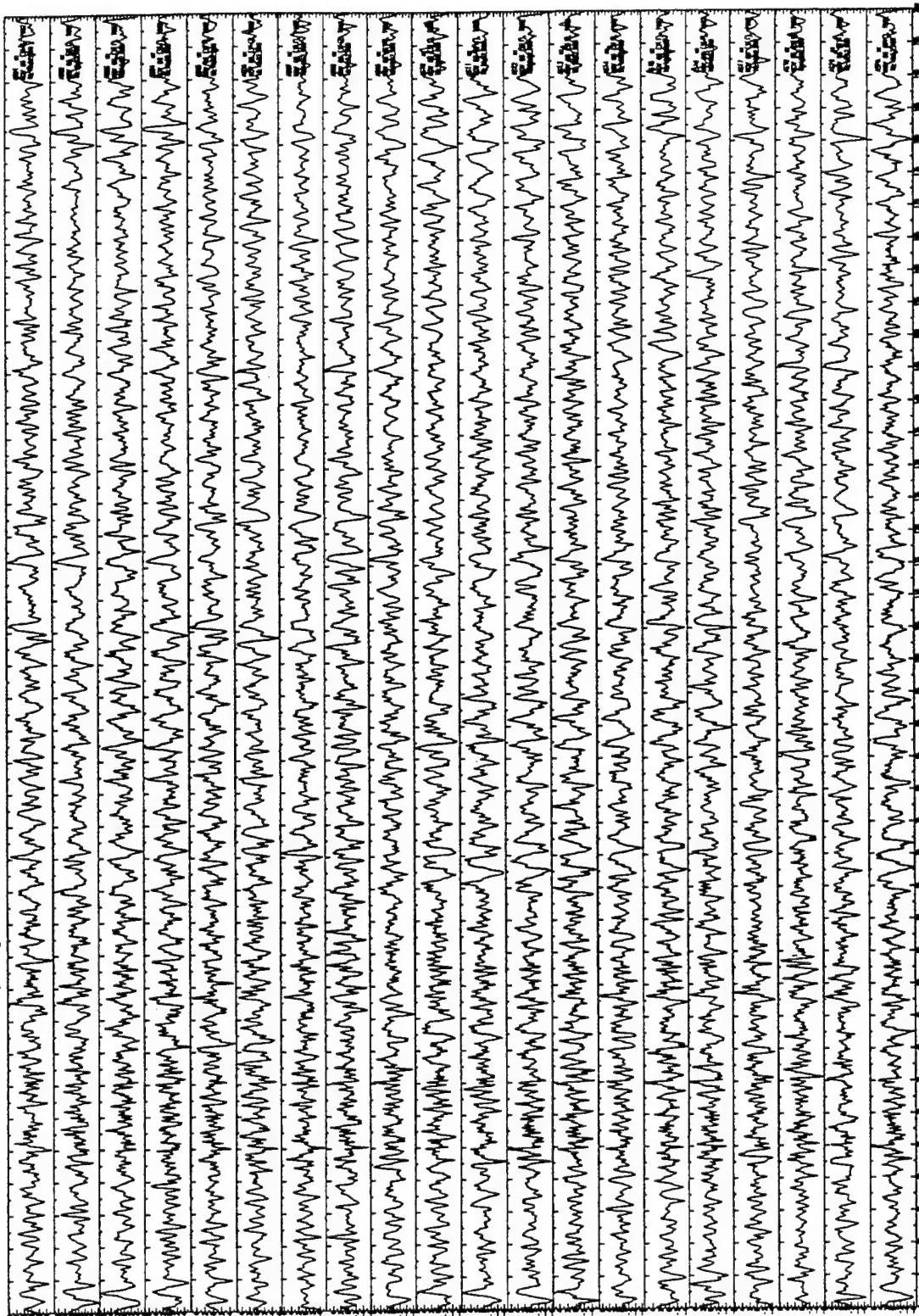
ASP – JD311 Nov 6, 1992 11h 47m 42.9s 12.0Km Mb=4.6 HP=1.0
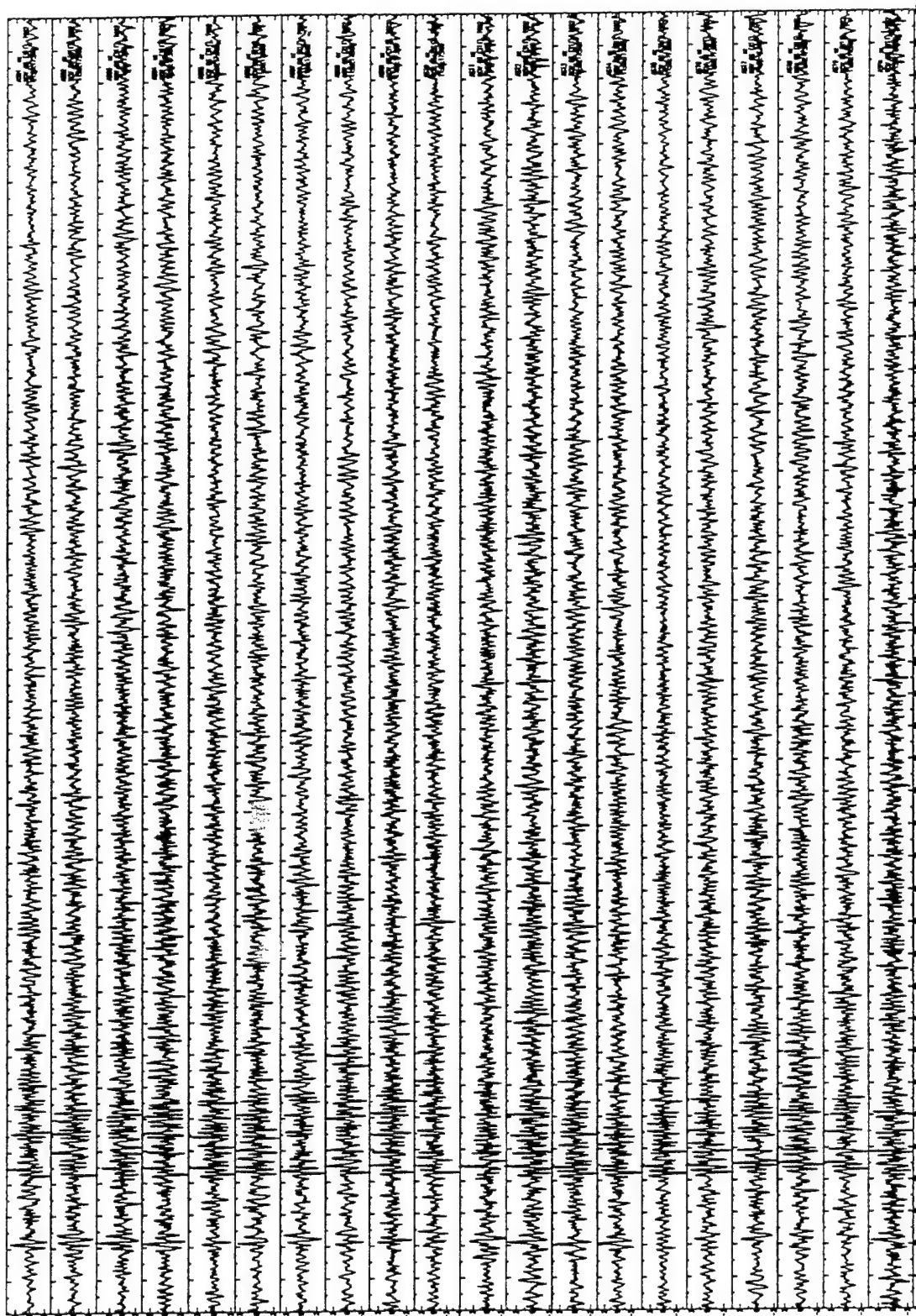
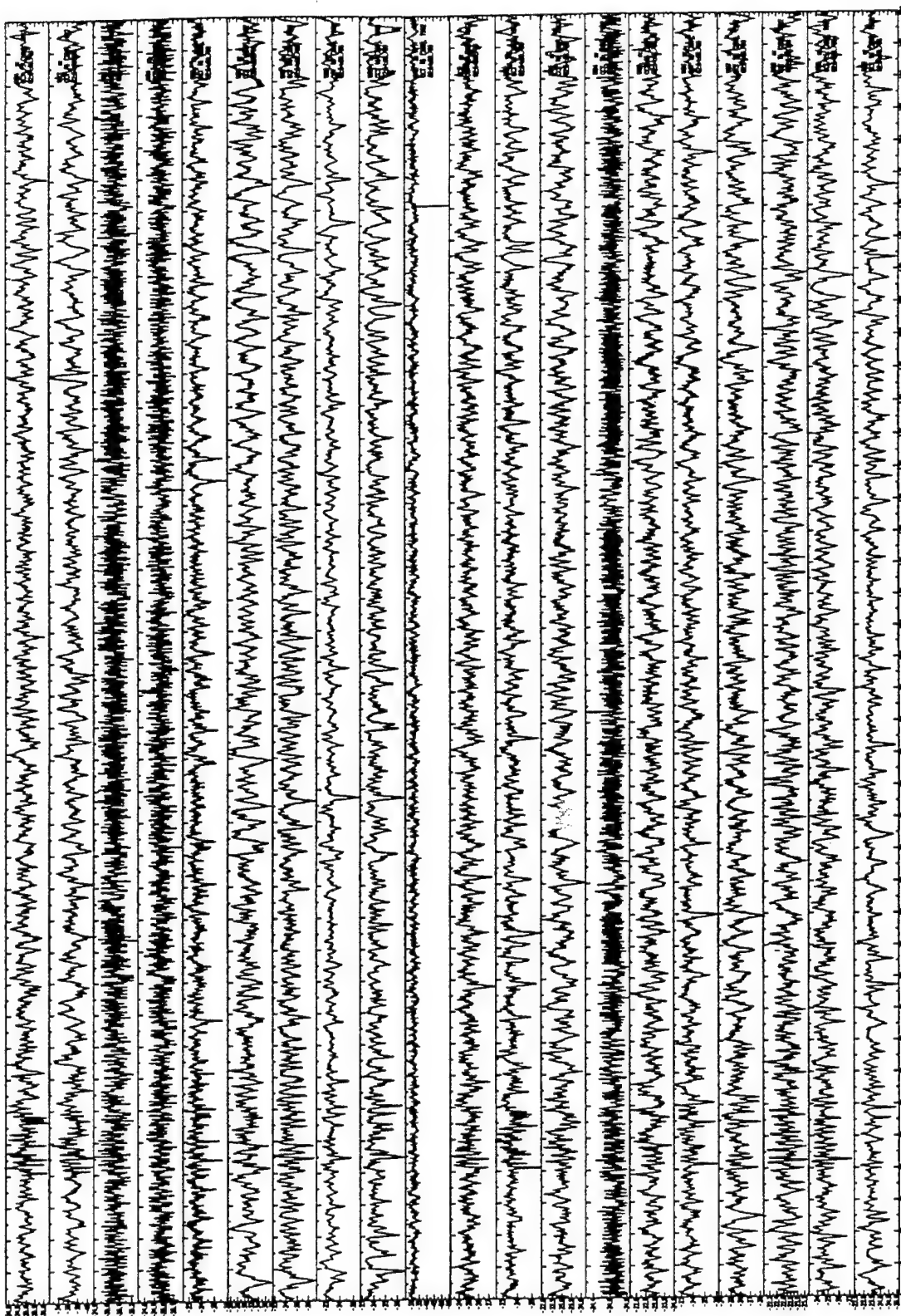Alice Spring – JD311   Nov 6, 92   07h21m57.8s   h=40.0Km   M=5.1
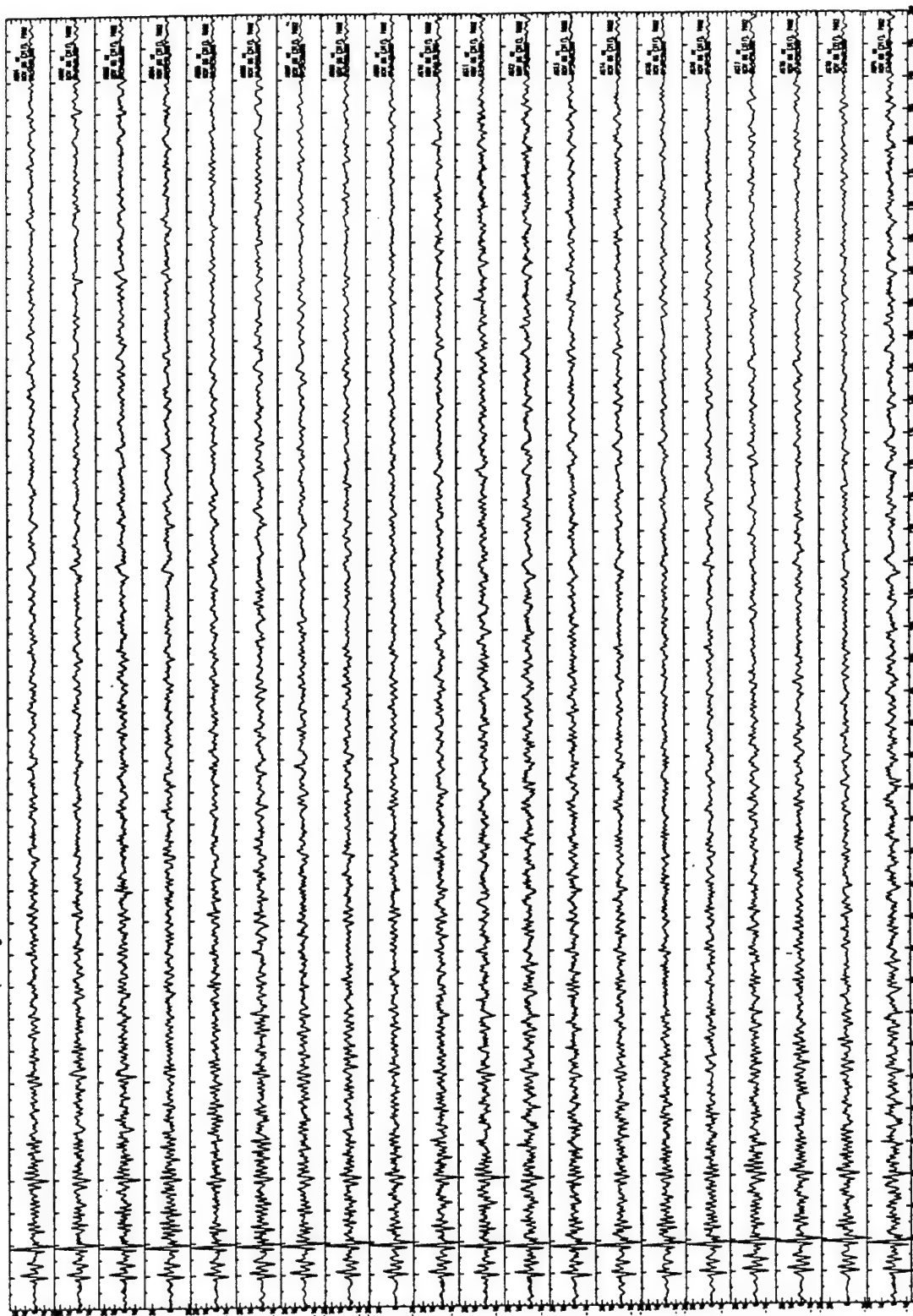
Alice Spring - JD292   Oct 18, 92   16h14m 45.5s   h=19.0Km   M=5.1
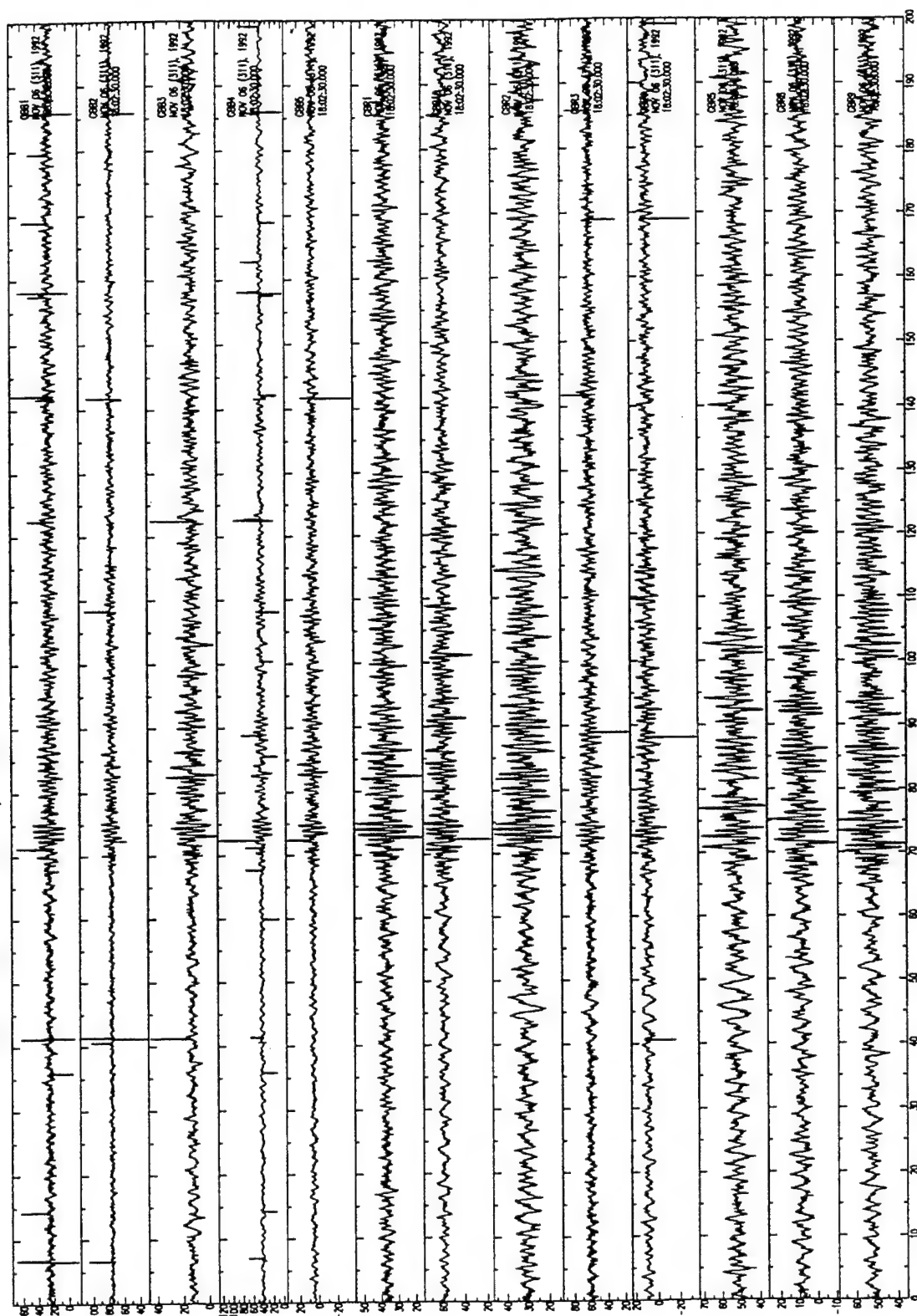
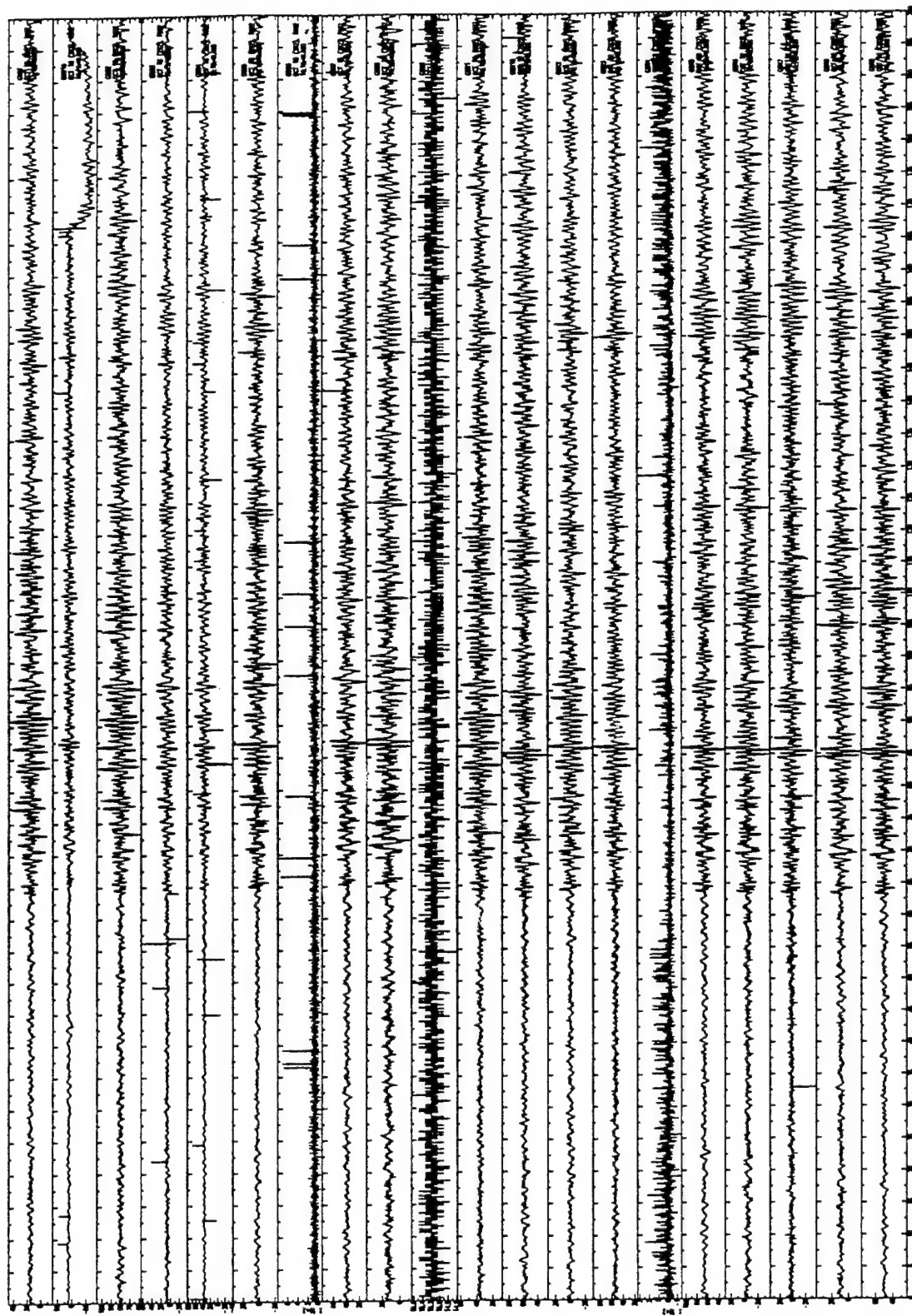WRA -JD311 Nov 6, 1992 07h 21m 57.8s H=40.0Km mb=5.1

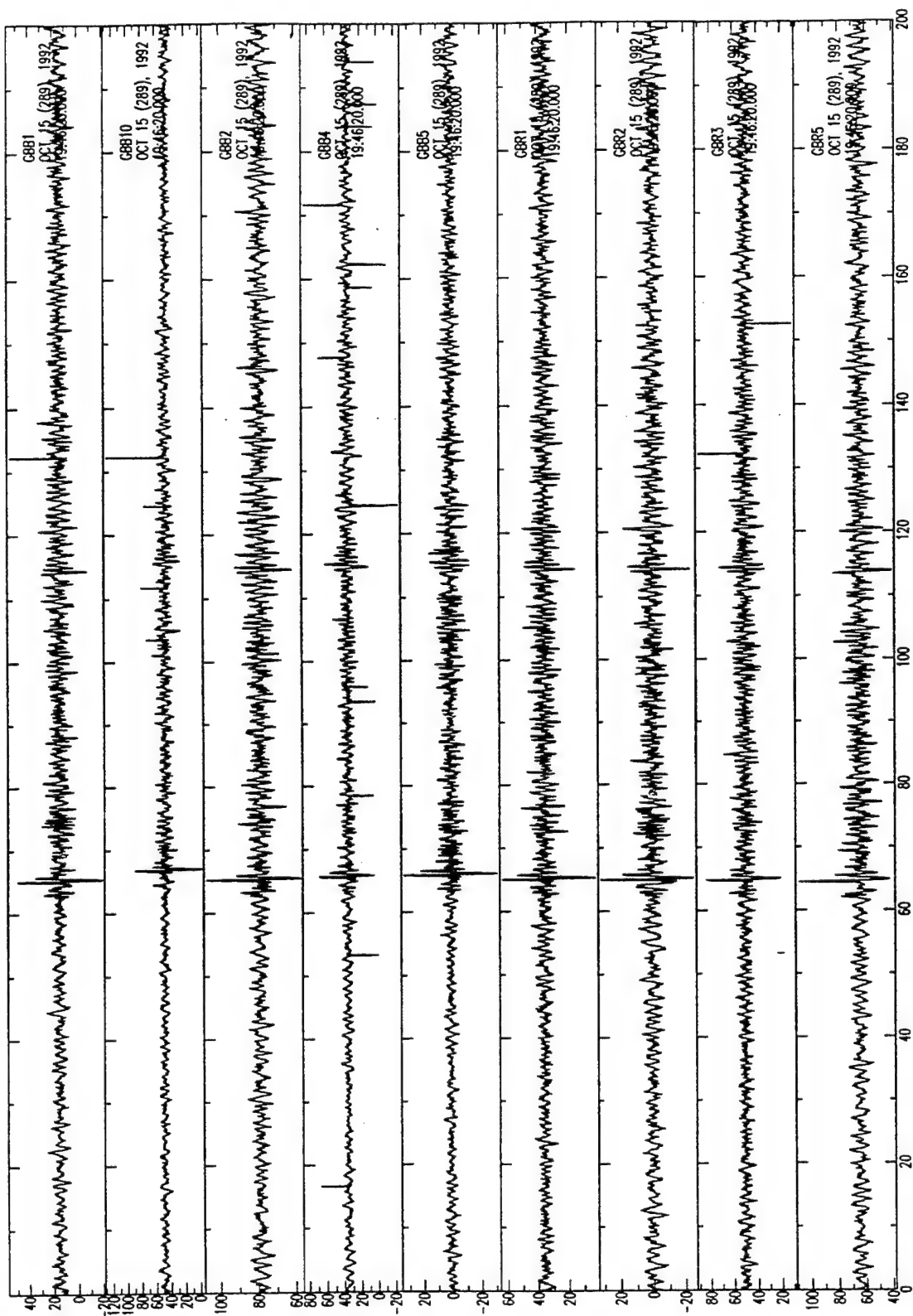WRA - JD289 Oct 15, 92 02h42m 06.3s 39.212N 72.798E 16.0Km 4.6

GBA   JD311 – Nov 6, 1992   17h 58m 38.0s   h=33.0Km Mb=4.5
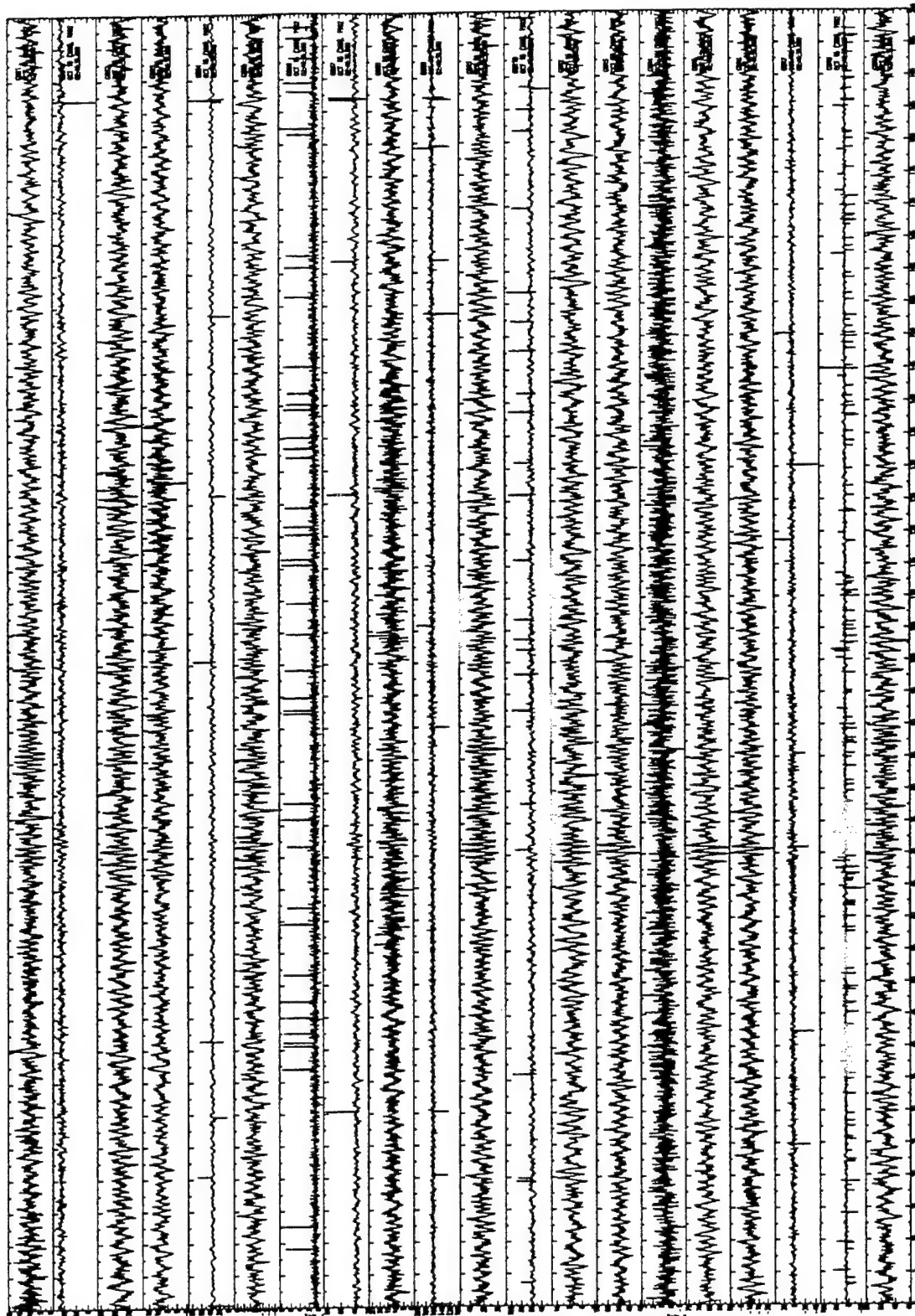
GBA - JD292   Oct 18, 1992 16h 14m 45.5s   h=19.0km   Mb=5.1
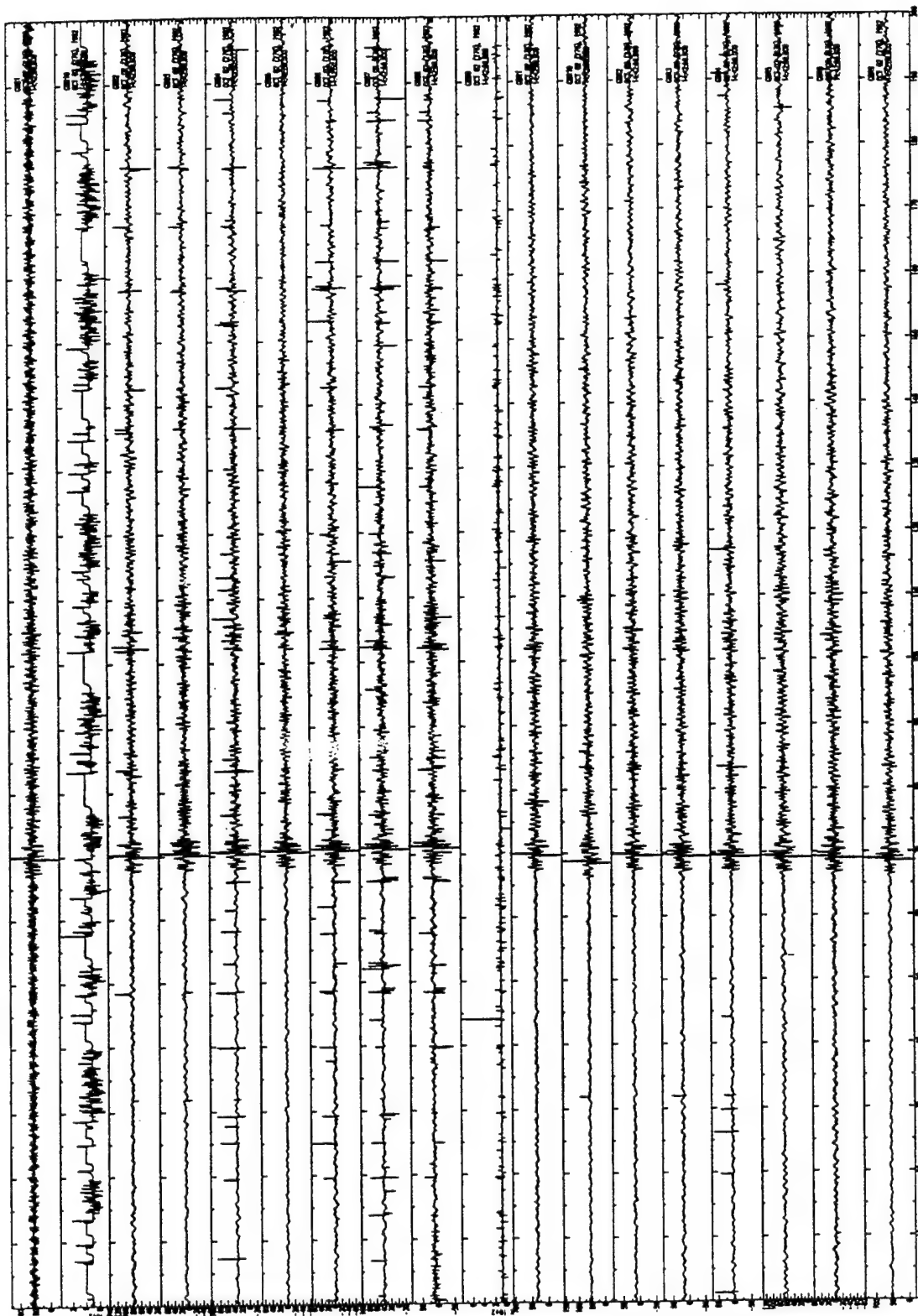

126

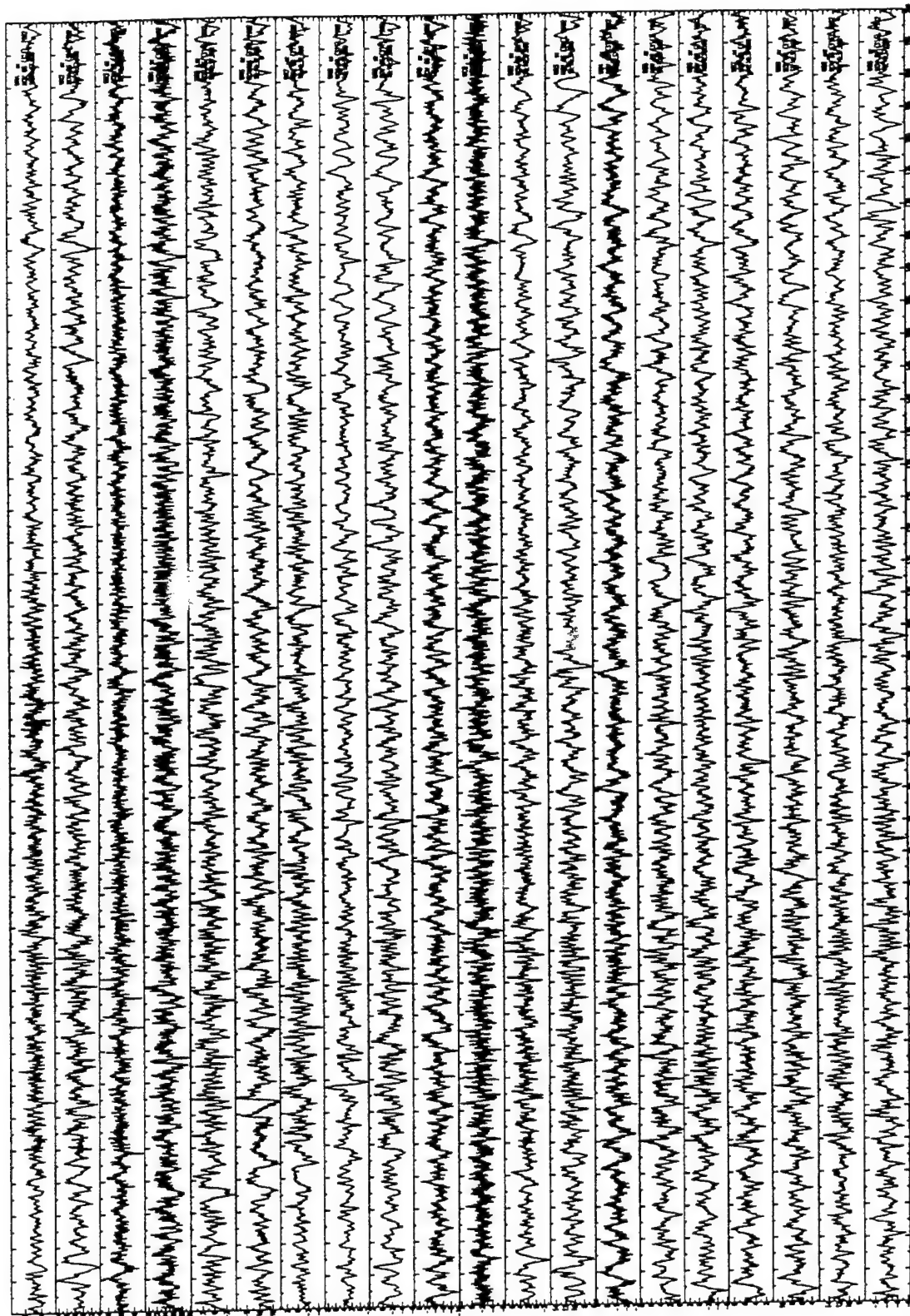GBA – JD289   Oct 15, 1992   19h 42m 11.80s   h=135.0Km   Mb=4.6

127

GBA — JD289 Oct 15, 1992 02h 42m 06.30s h=16.0Km Mb=4.6

GBA   JD276 - Oct 02, 92   14h38m 44.4s   h=118.0Km   M=4.9

WRA - JD311 Nov 6, 92   17h58m 38.0s   h=33.0Km   M=4.5

PROF. THOMAS AHRENS
SEISMOLOGICAL LAB, 252-21
DIVISION OF GEOLOGICAL & PLANETARY SCIENCES
CALIFORNIA INSTITUTE OF TECHNOLOGY
PASADENA, CA 91125

PROF. SHELTON ALEXANDER
GEOSCIENCES DEPARTMENT
403 DEIKE BUILDING
THE PENNSYLVANIA STATE UNIVERSITY
UNIVERSITY PARK, PA 16802

DR. THOMAS C. BACHE, JR.
SCIENCE APPLICATIONS INT'L CORP.
10260 CAMPUS POINT DRIVE
SAN DIEGO, CA 92121 (2 COPIES)

PROF. MUAWIA BARAZANGI
CORNELL UNIVERSITY
INSTITUTE FOR THE STUDY OF THE CONTINENT
3126 SNEE HALL
ITHACA, NY 14853

DR. DOUGLAS R. BAUMGARDT
ENSCO, INC
5400 PORT ROYAL ROAD
SPRINGFIELD, VA 22151-2388

DR. T.J. BENNETT
S-CUBED
A DIVISION OF MAXWELL LABORATORIES
11800 SUNRISE VALLEY DRIVE, SUITE 1212
RESTON, VA 22091

DR. ROBERT BLANDFORD
AFTAC/TT, CENTER FOR SEISMIC STUDIES
1300 NORTH 17TH STREET
SUITE 1450
ARLINGTON, VA 22209-2308

DR. STEVEN BRATT
NTPO
1901 N. MOORE STREET, SUITE 609
ARLINGTON, VA 22209

DR. JERRY CARTER
CENTER FOR SEISMIC STUDIES
1300 NORTH 17TH STREET
SUITE 1450
ARLINGTON, VA 22209-2308

MR ROBERT COCKERHAM
ARMS CONTROL & DISARMAMENT AGENCY
320 21ST STREET NORTH WEST
ROOM 5741
WASHINGTON, DC 20451,

DR. ZOLTAN DER
ENSCO, INC.
5400 PORT ROYAL ROAD
SPRINGFIELD, VA 22151-2388

DR. STANLEY K. DICKINSON
AFOSR/NM
110 DUNCAN AVENUE
SUITE B115
BOLLING AFB, DC

DR PETR FIRBAS
INSTITUTE OF PHYSICS OF THE EARTH
MASARYK UNIVERSITY BRNO
JECNA 29A
612 46 BRNO, CZECH REPUBLIC

DR. MARK D. FISK
MISSION RESEARCH CORPORATION
735 STATE STREET
P.O. DRAWER 719
SANTA BARBARA, CA 93102

DR. CLIFF FROHLICH
INSTITUTE OF GEOPHYSICS
8701 NORTH MOPAC
AUSTIN, TX 78759

DR. HOLLY GIVEN
IGPP, A-025
SCRIPPS INSTITUTE OF OCEANOGRAPHY
UNIVERSITY OF CALIFORNIA, SAN DIEGO
LA JOLLA, CA 92093

DR. JEFFREY W. GIVEN
SAIC
10260 CAMPUS POINT DRIVE
SAN DIEGO, CA 92121

DAN N. HAGEDON
PACIFIC NORTHWEST LABORATORIES
BATTELLE BOULEVARD
RICHLAND, WA 99352

DR. JAMES HANNON
LAWRENCE LIVERMORE NATIONAL LABORATORY
P.O. BOX 808, L-205
LIVERMORE, CA 94550

PROF. DANNY HARVEY
UNIVERSITY OF COLORADO, JSPC
CAMPUS BOX 583
BOULDER, CO 80309

PROF. DONALD V. HELMBERGER
DIVISION OF GEOLOGICAL & PLANETARY SCIENCES
CALIFORNIA INSTITUTE OF TECHNOLOGY
PASADENA, CA 91125

PROF. ROBERT B. HERRMANN
DEPARTMENT OF EARTH & ATMOSPHERIC SCIENCES
ST. LOUIS UNIVERSITY
ST. LOUIS, MO 63156

PROF. THOMAS H. JORDAN
DEPARTMENT OF EARTH, ATMOSPHERIC &
 PLANETARY SCIENCES
MASSACHUSETTS INSTITUTE OF TECHNOLOGY
CAMBRIDGE, MA 02139

PROF. CHARLES A. LANGSTON
GEOSCIENCES DEPARTMENT
403 DEIKE BUILDING
THE PENNSYLVANIA STATE UNIVERSITY
UNIVERSITY PARK, PA 16802

PROF. THORNE LAY
INSTITUTE OF TECTONICS
EARTH SCIENCE BOARD
UNIVERSITY OF CALIFORNIA, SANTA CRUZ
SANTA CRUZ, CA 95064

MR. JAMES F. LEWKOWICZ
PHILLIPS LABORATORY/GPE
29 RANDOLPH ROAD
HANSCOM AFB, MA 01731-3010(2 COPIES)

PROF. THOMAS V. MCEVILLY
SEISMOGRAPHIC STATION
UNIVERSITY OF CALIFORNIA
BERKELEY, CA 94720

PROF. BERNARD MINSTER
IGPP, A-025
SCRIPPS INSTITUTE OF OCEANOGRAPHY
UNIVERSITY OF CALIFORNIA, SAN DIEGO
LA JOLLA, CA 92093

MR. JACK MURPHY
S-CUBED
A DIVISION OF MAXWELL LABORATORY
11800 SUNRISE VALLEY DRIVE, SUITE 1212
RESTON, VA 22091 (2 COPIES)

PROF. JOHN A. ORCUTT
IGPP, A-025
SCRIPPS INSTITUTE OF OCEANOGRAPHY
UNIVERSITY OF CALIFORNIA, SAN DIEGO
LA JOLLA, CA 92093

PROF. EUGENE HERRIN
GEOPHYSICAL LABORATORY
SOUTHERN METHODIST UNIVERSITY
DALLAS, TX 75275

PROF. LANE R. JOHNSON
SEISMOGRAPHIC STATION
UNIVERSITY OF CALIFORNIA
BERKELEY, CA 94720

DR. RICHARD LACOSS
MIT LINCOLN LABORATORY, M-200B
P.O. BOX 73
LEXINGTON, MA 02173-0073

JIM LAWSON, CHIEF GEOPHYSICIST
OKLAHOMA GEOLOGICAL SURVEY
OKLAHOMA GEOPHYSICAL OBSERVATORY
P.O. BOX 8
LEONARD, OK 74043-0008

DR. WILLIAM LEITH
U.S. GEOLOGICAL SURVEY
920 NATIONAL
CENTER
RESTON, VA 22092

DR. GARY MCCARTOR
DEPARTMENT OF PHYSICS
SOUTHERN METHODIST UNIVERSITY
DALLAS, TX 75275

DR. KEITH L. MCLAUGHLIN
S-CUBED
A DIVISION OF MAXWELL LABORATORY
P.O. BOX 1620
LA JOLLA, CA 92038-1620

PROF. BRIAN J. MITCHELL
DEPARTMENT OF EARTH & ATMOSPHERIC SCIENCES
ST. LOUIS UNIVERSITY
ST. LOUIS, MO 63156

DR. KEITH K. NAKANISHI
LAWRENCE LIVERMORE NATIONAL LABORATORY
L-025
P.O. BOX 808
LIVERMORE, CA 94550

DR. HOWARD PATTON
LAWRENCE LIVERMORE NATIONAL LABORATORY
L-025
P.O. BOX 808
LIVERMORE, CA 94550

2

DR. FRANK PILOTTE
HQ AFTAC/TT
1030 SOUTH HIGHWAY A1A
PATRICK AFB, FL 32925-3002

DR. JAY J. PULLI
RADIX SYSTEMS, INC.
6 TAFT COURT
ROCKVILLE, MD 20850

PROF. PAUL G. RICHARDS
LAMONT-DOHERTY EARTH OBSERVATORY
 OF COLUMBIA UNIVERSITY
PALISADES, NY 10964

MR. WILMER RIVERS
MULTIMAX INC.
1441 MCCORMICK DRIVE
LANDOVER, MD 20785

DR. ALAN S. RYALL, JR.
LAWRENCE LIVERMORE NATIONAL LABORATORY
L-025
P.O. BOX 808
LIVERMORE, CA 94550

DR.CHANDAN K. SAIKIA
WOODWARD-CLYDE FEDERAL SERVICES
566 EL DORADO ST., SUITE 100
PASADENA, CA 91101-2560

MR. DOGAN SEBER
CORNELL UNIVERSITY
INST. FOR THE STUDY OF THE CONTINENT
3130 SNEE HALL
ITHACA, NY 14853-1504

SECRETARY OF THE AIR FORCE
(SAFRD)
WASHINGTON, DC 20330

OFFICE OF THE SECRETARY OF DEFENSE
DDR&E
WASHINGTON, DC 20330

THOMAS J. SERENO, JR.
SCIENCE APPLICATION INT'L CORP.
10260 CAMPUS POINT DRIVE
SAN DIEGO, CA 92121

DR. MICHAEL SHORE
DEFENSE NUCLEAR AGENCY/SPSS
6801 TELEGRAPH ROAD
ALEXANDRIA, VA 22310

PROF. DAVID G. SIMPSON
IRIS, INC.
1616 NORTH FORT MYER DRIVE
SUITE 1050
ARLINGTON, VA 22209

DR. JEFFREY STEVENS
S-CUBED
A DIVISION OF MAXWELL LABORATORY
P.O. BOX 1620
LA JOLLA, CA 92038-1620

PROF. BRIAN STUMP
LOS ALAMOS NATIONAL LABORATORY
EES-3
 MAIL STOP C-335
LOS ALAMOS, NM 87545

PROF. TUNCAY TAYMAZ
ISTANBUL TECHNICAL UNIVERSITY
DEPT. OF GEOPHYSICAL ENGINEERING
MINING FACULTY
MASLAK-80626, ISTANBUL TURKEY

PROF. M. NAFI TOKSOZ
EARTH RESOURCES LAB
MASSACHUSETTS INSTITUTE OF TECHNOLOGY
42 CARLETON STREET
CAMBRIDGE, MA 02142

DR. LARRY TURNBULL
CIA-OSWR/NED
WASHINGTON, DC 20505

PROF. TERRY C. WALLACE
DEPARTMENT OF GEOSCIENCES
BUILDING #77
UNIVERSITY OF ARIZONA
TUSCON, AZ 85721

DR. WILLIAM WORTMAN
MISSION RESEARCH CORPORATION
8560 CINDERBED ROAD
SUITE 700
NEWINGTON, VA 22122

ARPA, OASB/LIBRARY
3701 NORTH FAIRFAX DRIVE
ARLINGTON, VA 22203-1714

DEFENSE TECHNICAL INFORMATION CENTER
8725 JOHN J. KINGMAN ROAD
FT BELVOIR, VA 22060-6218 (2 copies)

TACTEC
BATTELLE MEMORIAL INSTITUTE
505 KING AVENUE
COLUMBUS, OH 43201 (FINAL REPORT)

PHILLIPS LABORATORY
ATTN: GPE
29 RANDOLPH ROAD
HANSCOM AFB, MA 01731-3010

PHILLIPS LABORATORY
ATTN: TSML
5 WRIGHT STREET
HANSCOM AFB, MA 01731-3004

PHILLIPS LABORATORY
ATTN: PL/SUL
3550 ABERDEEN AVE SE
KIRTLAND, NM 87117-5776 (2 COPIES)

DR. MICHEL CAMPILLO
OBSERVATOIRE DE GRENOBLE
I.R.I.G.M.-B.P. 53
38041 GRENOBLE, FRANCE

PROF. HANS-PETER HARJES
INSTITUTE FOR GEOPHYSIC
RUHR UNIVERSITY/BOCHUM
P.O. BOX 102148
4630 BOCHUM 1, GERMANY

PROF. EYSTEIN HUSEBYE
IFJF
JORDSKJELVSTASJONEN
ALLEGATEN 41, 5007 BERGEN NORWAY

DAVID JEPSEN
ACTING HEAD, NUCLEAR MONITORING SECTION
BUREAU OF MINERAL RESOURCES
GEOLOGY AND GEOPHYSICS
G.P.O. BOX 378, CANBERRA, AUSTRALIA

DR. PETER MARSHALL
PROCUREMENT EXECUTIVE
MINISTRY OF DEFENSE
BLACKNEST, BRIMPTON
READING FG7-FRS, UNITED KINGDOM

DR. BERNARD MASSINON, DR. PIERRE MECHLER
SOCIETE RADIOMANA
27 RUE CLAUDE BERNARD
75005 PARIS, FRANCE (2 COPIES)

DR. SVEIN MYKKELTVEIT
NTNT/NORSAR
P.O. BOX 51
N-2007 KJELLER, NORWAY (3 COPIES)

DR. JORG SCHLITTENHARDT
FEDERAL INSTITUTE FOR GEOSCIENCES & NAT'L RES.
POSTFACH 510153
D-30631 HANNOVER, GERMANY

DR. JOHANNES SCHWEITZER
INSTITUTE OF GEOPHYSICS
RUHR UNIVERSITY/BOCHUM
P.O. BOX 1102148
4360 BOCHUM 1, GERMANY

TRUST & VERIFY
VERTIC
CARRARA HOUSE
20 EMBANKMENT PLACE
LONDON WC2N 6NN, ENGLAND

4